UNIVERSITY
OF OSLO

Master's thesis

Modelling wave-induced losses on floating photovoltaic systems

Energy yield modelling with high geographical resolution

Nils Enric Canut Taugbøl

60 ECTS study points

Department of Physics
Faculty of Mathematics and Natural Sciences

3rd June 2025

Modelling wave-induced losses on floating photovoltaic systems

Nils Enric Canut Taugbøl

3rd June 2025

Abstract

Floating photovoltaic (FPV) systems have seen a growing interest over the past 10 years as a land-saving alternative in renewable energy generation. Until recently FPV systems have been installed on in-land water bodies. FPV systems are now increasingly installed in nearshore and offshore areas since. Installations at sea experience varying sea-states which may impact the energy generation of FPV systems. For FPV systems installed with floats, wave-induced motion alter the orientations of modules with respect their initial orientation causing an energy loss with respect to a system unaffected by waves.

This thesis models the energy losses caused by wave-induced motion on an FPV system at three specific locations near Risør, Norway. The total wave-induced loss (WIL) is decomposed into a wave-induced mismatch loss (WIML) and a wave-induced irradiance loss (WIIL). The WIML and WIIL are new definitions presented in this thesis. To model the energy yield, the SWAN wave model is used for modelling sea-states at specific locations. The FPV modules' motion are simulated using the proprietary software 3DFloat. The electrical modelling is performed by combining Python libraries, irradiance data from CAMS, and the simulated module movements.

A sensitivity scan is performed on the WIL for the sea-state variables used in 3DFloat. The WIL as a function of incoming wave direction is found to have a 180-degree rotational symmetry. The wave-induced losses are modelled for the year 2023 at three locations near Risør, for a 10-module series-connected FPV system with and without initial tilt. The WIL is between 0.837% and 1.429% for a system with no initial tilt, at the three locations. For a system placed with 15° initial southward tilt, the WIL showed a $\sim 30\%$ reduction. The WIML is found to be larger than the WIIL by an order of magnitude.

Contents

List of Figures

List of Tables

Chapter 1

Introduction

The world is in an unprecedented predicament: human-caused greenhouse gas (GHG) emissions over the past century are inducing rapid global climate change, which in turn endangers almost all lifeforms on the planet, including humans. GHGs trap heat from the sun that is reflected off the surface of the earth before it can escape into space, which is known as the greenhouse effect. Without human interference, the naturally occurring greenhouse effect keeps the temperature of the earth level. The released GHGs by humans, predominantly in developed industrial regions, has caused the global surface temperature to increase by approximately 1°C over the past century. Due to climate change, there has been an increase in frequency and magnitude of extreme weather conditions such as heavy rainfalls, droughts, and heatwaves [5]. These weather conditions pose an increasing threat to human health, infrastructure, and settlements [8]. Another effect of climate change, is a shift in the nature of weather seasons and their lengths, which forces animal species poleward or to higher elevations, and causes the degradation of land (such as desertification). In sum, the consequences of climate change are many, its cause is known, and it is recognised as a problem [32].

Reducing, or eliminating, the use of fossil fuels, and the practices used to produce them, is an important step in mitigating climate change. The main contributing sector to GHG emissions, and consequently to climate change, is the energy sector with 34% of global GHG emissions in 2019, followed by the industry, and AFOLU (Agriculture, Forestry and Other Land of Use) sectors with 24% and 22% of global GHG emissions respectively in 2019 [5]. Replacing fossil fuels, such as crude oil and coal, with renewable energy sources, such as solar photovoltaics (PV) and wind, is a known and necessary solution for climate change mitigation as they do not release GHGs during operation [5, 32]. Renewable energy sources, or renewables for short, are naturally renewing sources of energy which we can harvest and use, for example for transport or in our electricity grids.

The past 30 years has seen an increase in installed capacity of renewables, especially wind and solar PV. At the signing of the Kyoto Protocol in 1997, 19.6% of the global electricity generation originated from renewable energy sources[1], wind and solar PV represented 0.1% and 0.0% of the global electricity generation respectively in 1997. At the signing of the Paris Agreement in 2015, 3.4% and 1.0% of the global electricity generation came from wind and solar PV respectively. Other renewable sources represented 18.6% of the global electricity generation in 2015. In 2023, 7.8% and 5.4% of the global electricity generation came from wind and solar PV respectively, making 30.2% of the world's energy generation renewable [14].

---

[1] Nuclear energy is not considered a renewable energy source.

An important aspect of the growth in wind and solar PV energy sources is their reduction in costs. In the past 15 years, the cost of producing energy through solar PV and wind has reduced noticeably as shown in Table 1.1, where the LCOE of solar PV, wind and fossil fuels are compared. The levelised cost of electricity (LCOE) is a measure that represents the average cost of the energy produced by an energy generator, such as a solar PV farm, over the lifetime of that generator. In 2010, the global weighted average LCOE ($\mathrm{LCOE_{gwa}}$) of solar PV and offshore wind were above the upper range of the LCOE of fossil fuels. On the other hand, the LCOE range of onshore wind was similar to that of fossil fuels in 2010. By 2023, the $\mathrm{LCOE_{gwa}}$ of solar PV and onshore wind had reduced to be below the lower range of the LCOE of fossil fuels. The upper range of the LCOE of onshore wind had even reached the lower level of the LCOE of fossil fuels by 2023. Though offshore wind experienced a reduction in $\mathrm{LCOE_{gwa}}$ similar to that of solar PV and onshore wind, the LCOE range of offshore wind remained large. The variations in the LCOE range of offshore wind have been large between 2010 and 2023, albeit the overall trend is a reduction in costs. The low cost and social acceptance of solar PV has led to a rapid growth of installed solar PV capacity with a $\sim 75\%$ increase of added capacity between 2023 and 2024: in 2023 the added capacity in solar PV was ~ 456 GW while in 2024 the added solar PV capacity was ~ 602 GW [30].

Table 1.1: Comparison of the LCOE (in USD/kWh) between solar PV, onshore and offshore wind, and fossil fuels for the years 2010 and 2023. The data is gathered from [25]. In [25], there is no reported $\mathrm{LCOE_{gwa}}$ for fossil fuels and the LCOE range for fossil fuels is shown as constant between 2010 and 2023.

Energy source	Year	$\mathrm{LCOE_{gwa}}$	LCOE lower range	LCOE upper range
Solar PV	2010	0.460	~ 0.23	> 0.5
	2023	0.044	~ 0.04	~ 0.11
Onshore wind	2010	0.111	~ 0.07	> 0.15
	2023	0.033	~ 0.025	~ 0.075
Offshore wind	2010	0.203	~ 0.12	> 0.3
	2023	0.075	~ 0.05	~ 0.21
Fossil fuels	2010-2023		~ 0.07	~ 0.17

Despite the reduction in costs, solar PV installations remain land-intensive at $\sim 1.5 \times 10^4$ $\mathrm{m^2/MW}$ [10]. A land-sparing alternative for solar PV that has seen an increase in popularity in recent years are floating photovoltaic (FPV) installations. FPV installations are solar PV systems placed on water which increase the capacity of renewable energy sources while ceding land in favour of agriculture and other essential necessities. The land-saving aspects of FPV give reason to the yearly doubling of globally installed FPV capacity from the first FPV installation deployed in 2008 to ~ 7.7 GW in 2023 [42]. Deploying solar PV systems on water bodies also carries potential benefits such as a cooling effect due to the FPV system's proximity to water or exposure to wind [12, 29] and reduced water evaporation [18, 24]. Between 2008 and 2019, all FPV installations have been deployed on inland water bodies such as lakes or artificial water reservoirs; the first offshore FPV installation was deployed in 2019 [49]. The delay in deploying FPV in offshore or nearshore locations is attributed to the differences between freshwater and saltwater environments, exposure to harsher weather conditions, and higher costs compared to land-based solar PV.

When installing new FPV systems, it is useful to model the expected energy yield of the system to assess the profitability and sustainability of the new installation. The literature considering FPV yield-modelling is limited and well summarised by Alcañiz et al. in [1]. As summarised by Alcañiz et al., most yield-modelling works focus on the thermal aspects of FPV being placed near water or in contact with water. In the case of wave-modelling for FPV systems, most works have focused on the dynamical response and mechanical load of the installations in the new environments without exploring the effect of the waves on the energy yield. Publications on the effect of waves on the yield of FPV systems are few and relatively recent [1, 7, 11, 19, 35]. This research has been limited since the majority of FPV installations have been on inland water bodies where the wave-induced movements of the modules are often negligible.

As FPV systems move to areas with more waves, the impact of the waves on the FPV system's energy yield will increase, giving compelling reason to include the wave-induced effects in the energy yield. The influence of waves on FPV systems is a yield-affecting condition unique to FPVs. Waves reaching an FPV installation will induce movement to the floats and consequently to the PV modules mounted on the floats. The movement of the modules will induce variations in the orientation of the modules with respect to their initial orientation, altering the total incoming irradiance compared to a non-moving PV system at the same location. The wave-induced movement can affect the total energy-yield in two ways. First, the difference in total received irradiance between an FPV system with wave-induced movement, and a similar FPV system unaffected by waves, can be considered an optical effect: the movement may reduce or increase the total received irradiance. Second, if the modules in an array are installed such that they can move independently, the wave-induced motion will cause different irradiance conditions on different modules leading to an electrical mismatch loss.

Of the publications that study the effect of waves on the yield of FPV systems, Golroodbari and van Sark [19], and Alcañiz et al. [1], model the energy yield of an FPV system without considering electrical mismatch between the modules. To model the wave-induced movement on the modules, Golroodbari and van Sark recreate a sea surface, based on different measured wind speeds, from which they compute the resulting torque applied to the floats. From the torque and the float specifications, they compute the resulting orientations of the float. Alcañiz et al. expand the work of Golroodbari and van Sark by including two rotational axes, pitch and roll, where Golroodbari and van Sark included a single rotational axis. Both Alcañiz et al. and Golroodbari and van Sark compute the irradiance on their modelled FPV systems based on the computed orientation of a single extended float, effectively eliminating mismatch effects but including an optical loss.

Of the existing literature, Dörenkämper et al. [11] and Nysted et al. [35] model the total wave-induced loss (WIL), i.e. the optical and electrical losses together[2]. In both works, the total wave-induced loss is computed by finding the irradiance on each module in a moving FPV system based on their calculated surface normals. Dörenkämper et al. model the pitch and roll of individual floats with two different approaches: one where the floats follow the sea surface perfectly, and one where they calculate the torque applied on the floats. Dörenkämper et al. analyses, with measured sea-states and irradiance conditions, the how the WIL varies with increasing FPV system size and how it varies over the course of a year. Nysted et al. apply an approach similar to Dörenkämper et al. by assuming that the modules strictly follow the sea surface: they compute the surface normal of a module based on the sea surface elevation at the four sides and centre of the float. Nysted et al. extend the analysis performed by Dörenkämper et al. by additionally

---

[2] Dörenkämper et al. labels the total wave-induced loss for as WIML. In this thesis, the term WIML is reserved for the electrical loss only.

exploring how different sea surfaces affect the WIL under clearsky conditions.

One publication, by Chen et al. [7], separate the electrical and optical losses within the total wave-induced loss. Chen et al. analytically model the float movements, based on Stokes wave theory and the equation of motion of a free-floating body [33], and model the energy yield in the same manner as done by Dörenkämper et al.. However, Chen et al. do not present the methodology used to separate the electrical and optical losses within the total wave-induced loss. Chen et al. report significant optical losses compared to the electrical losses for an FPV system placed with an optimal tilt angle.

This thesis builds on and extends the existing literature on energy yield modelling of FPV systems. The goal is to assess the wave-induced energy losses of FPVs at chosen locations with a reusable pipeline that relies on existing datasets. The wave-induced energy losses of an FPV system consisting of 10 series-connected modules are modelled for the full year 2023 at three select locations near Risør, Norway. We look exclusively at the effect the movement of the modules has on the performance and, as a simplification, structural interactions between the water and the floats are omitted. The approach used in this thesis to model the wave-induced energy losses is based on the work of Nysted et al., where the same methodology is used to find the module orientations and energy yield. The modelling of the wave-induced energy losses of an FPV system is performed with a pipeline developed in this thesis, with realistic and continuous sea states for the chosen deployment location. A third-generation wave model is used to model the wave surface energy distribution at a high temporal resolution for a precise geographical location. From the modelled wave surface energy distribution, the module movements are simulated based on a reconstruction of the wave spectrum and compute the energy yield considering mismatch effects between the modules. The total wave-induced energy loss is decomposed into the optical wave-induced irradiance loss (WIIL) and the electrical wave-induced mismatch loss (WIML). This work provides novel definitions for the WIIL and WIML as the terms have not been explicitly defined in the literature. The total wave-induced loss has been defined by Nysted et al., though in this work their definition is slightly altered to allow for negative WIL. Though the wave-induced energy loss is modelled for three select locations, the pipeline has been developed to be applicable worldwide.

The thesis is structured as follows. The relevant theory and methods is presented in Chapter 2. In section 2.1, the background for mismatch conditions in FPV systems is presented, followed by a consideration on what data source is optimal to simulate the FPV system movement in section 2.2. Sea surface simulation methodology is presented in section 2.3. The computational pipeline, datasets and system specifics used in this thesis are then presented in section 2.4. In Chapter 3, he results are presented and discussed in a sequential fashion. In section 3.1, a short validation of the simulated module movements is performed by use of site measurements. Section 3.2 presents a sensitivity scan over the relevant sea-state variables and their impact on the WIL, while section 3.3 presents a wave-induced loss analysis for three different locations near Risør, Norway.

On the use of large language models

In the process of writing this thesis, the privacy-friendly UiO GPT service (www.uio.no/tjenester/it/ki/gpt-uio/) has been used. No other multi-level perceptron models has been used in relation to this thesis. The service has been used for debugging purposes when developing the pipeline for the thesis, as well as for the writing of the code documentation. UiO GPT has been seeked out when creating the figures found in Chapter 2, though the service did not provide useful answers. UiO GPT has also been used to discuss certain topics when writing Chapter 2. The discussions with UiO GPT were followed by online fact-checks from reliable sources. UiO GPT has not been used to generate any text found in this document, neither during the writing process nor during the proofreading.

Chapter 2

Theory and methods

In this chapter, I present the knowledge and background information necessary to comprehend the results and the pipeline developed for this thesis. First, I present the basic components of an FPV system and explain how mismatch conditions occur in section 2.1. In particular, novel definitions of the wave-induced irradiance loss and wave-induced mismatch loss are presented in section 2.1.4. In section 2.2, I elaborate on the possible sources for sea surface data and discuss their benefits and drawbacks. The approach used to simulate the FPV system movement is presented in section 2.3. To conclude Chapter 2, I present the pipeline developed for this thesis in section 2.4. The specific datasets used in this thesis, as well as the FPV system parameters and the locations studied, can also be found in section 2.4.

2.1 Wave-induced mismatch on FPV

The WIL is defined as the sum of electrical and optical losses in FPV systems caused by waves interacting with the system. To compute the WIL, I present background information to explain the power loss due to wave-induced motion on FPV systems. The basics of the solar cell starting from the pn-junction are presented in section 2.1.1. Section 2.1.2 gives a short overview on the operation of PV systems. To conclude section 2.1, I present how mismatch conditions occur before presenting mathematical definitions of the wave-induced mismatch effects on FPV systems.

2.1.1 The solar cell

The main building block of a solar cell is a pn-junction. A pn-junction is formed by joining two semiconductor materials, one which has an abundance of holes[1], called a p-type semiconductor (p for positive), and another which has an abundance of electrons, called an n-type semiconductor (n for negative). When joining the p-type and n-type semiconductor materials together, the excess holes and electrons at the junction diffuse into the opposing semiconductor. This diffusion creates positive ions on the n side of the junction and negative ions on the p side of the junction which results in an electric field within which there are no free charge carriers. The region at the junction in which there are no free charge carriers is called the depletion region[2]. Figure 2.1 shows a simplified illustration of a pn-junction.

---

[1] Holes are positive charge carriers that represent the absence of an electron in the atomic structure of the material.

[2] The depletion region has a limited size due to the immobility of the atoms in the material.

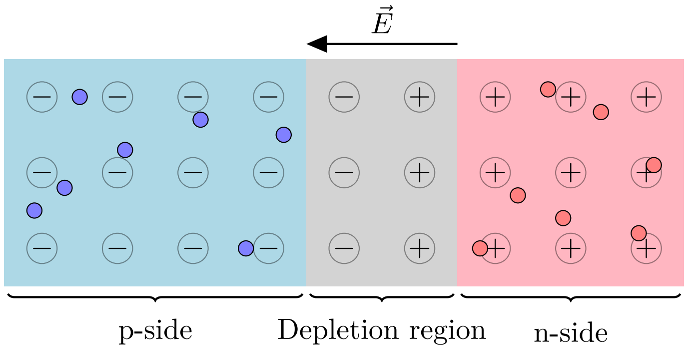

Figure 2.1: Simplified pn-junction. The circled minus and plus signs represent the fixed ions with negative or positive charge respectively. The blue opaque circles represent free holes and the red opaque circles represent free electrons. In the depletion region there are no free charge carriers. The ions left in the depletion region create an electric field $\vec{E}$ from the n-side to the p-side of the depletion region.

To generate current, the pn-junction of a solar cell must be exposed to irradiation: incident photons from the sun or other electromagnetic sources. If an incoming photon has an energy equal to or larger than the bandgap of the semiconductors, the photon may be absorbed to excite an electron from the valence band to the conduction band. The bandgap is the difference, in energy, between the highest energy level of an atom where electrons are present (the valence band) to the next energy level (the conduction band). The excitation of the electron leaves behind a hole in the valence band, the absorption of a photon thus creates an electron-hole pair. If the electron-hole pair is created within or near the depletion region, the electric field at the junction can separate the pair by sending the hole to the p-side and the electron to the n-side, where they become excess carriers. An electron-hole pair created within the n or p sides will most likely recombine before being separated, i.e. the pair won't contribute in generating current. The excess charge carriers move the pn-junction out of its equilibrium by increasing the electric potential between the p and n sides, effectively applying a forward bias to the solar cell. If the forward biased solar cell is connected to an external closed circuit, the excess electrons will flow from the n-side of the junction into the circuit to recombine with the holes at the p-side of the junction thus creating a net current.

The simplest description of a solar cell is given by the single diode model as shown in Figure 2.2 as a circuit diagram. In this model, the solar cell is divided into a light-generated current source, a diode for the pn-junction, and the resistances which appear due to non-idealities in the cell circuit. The internal cell resistances are divided into a resistance in series R_s and a resistance in parallel called the shunt resistance R_{sh}. While the series resistance arises from the circuit materials and contact properties, the shunt resistance arises due to manufacturing errors creating alternate current paths. The governing equation for the current in the single diode model as shown in Figure 2.2 is given by

$$I = I_L - I_0 \left(e^{\frac{q(V+IR_s)}{kT}} - 1 \right) - \frac{V + IR_s}{R_{sh}}, \tag{2.1}$$

where I is the output current, I_L is the photon-generated current, I_0 is the leakage current[3], V is the voltage over the cell, k is the Boltzmann constant and T is the cell

---

[3] The leakage current is the current flow in the absence of light.

temperature. In (2.1), a large R_s leads to a lower output current and that a large R_{sh} leads to a higher output current.

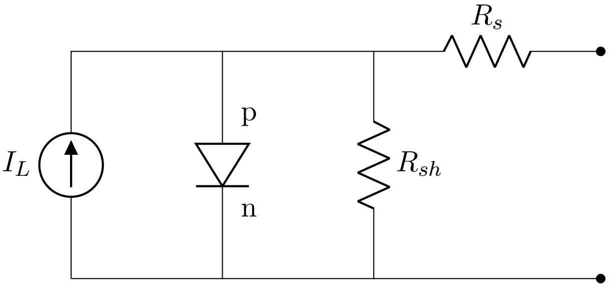

Figure 2.2: Single diode model with shunt and series resistance. The light-generated current is depicted as a separate current source parallel to the pn-junction diode to better suit the form of (2.1). The p and n sides of the diode are depicted respectively with the letters p and n.

While the single diode model is the most widespread, there are myriad models that describe the resulting current from a solar cell. This thesis uses the double diode model as shown in Figure 2.3 when modelling the FPV power generation. The double diode model takes into account recombination of charge carriers in and around the depletion region when the voltage across the circuit is low. This recombination is called the junction recombination. The junction recombination is represented by a second diode with its own leakage current and ideality factor η. The governing equation for the current in the double diode model is

$$I = I_L - I_{01}\left(e^{\frac{q(V+IR_s)}{\eta_1 kT}} - 1\right) - I_{02}\left(e^{\frac{q(V+IR_s)}{\eta_2 kT}} - 1\right) - \frac{V+IR_s}{R_{sh}}, \tag{2.2}$$

where the subscripts 1 and 2 correspond to the first and second diode respectively. The ideality factor is a parameter used to adjust the diode equation to fit observed behaviour that deviates from the ideal diode equation

$$I = I_0\left(e^{\frac{qV}{\eta kT}} - 1\right), \tag{2.3}$$

where $\eta = 1$ in the ideal case and $\eta > 1$ in the non-ideal cases. The ideality factor for the first diode in (2.2) is usually $\eta_1 = 1$, while the ideality factor for the second diode is large, f.ex. $\eta_2 = 2$.

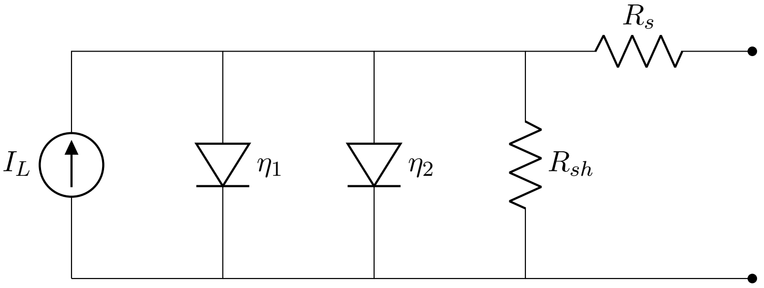

Figure 2.3: Double diode model with shunt and series resistance. The first and second diodes are differentiated by their ideality factors η_1 and η_2. The η_2 diode is non-ideal and takes into account recombinations of electron-hole pairs near and around the depletion region.

2.1.2 Operation of a photovoltaic module

The light-generated current from a solar cell can be harvested as power,

$$P = IV, \tag{2.4}$$

as it flows through an external circuit. To extract the highest possible power of the generated current, the cell must be operated at the point where $P = IV$ is at its maximum within the operating range of the cell, called the maximum power point (MPP). The operating range of a cell is defined by the maximum current and voltage the solar cell can generate when illuminated. The largest current a cell can generate when illuminated, called the short-circuit current I_{sc}, is when the cell circuit has no external resistance, i.e. it is short-circuited. The maximum voltage a cell can generate when illuminated, called the open-circuit voltage V_{oc}, is when the cell circuit has infinite external resistance, i.e. it is open-circuited. The I_{sc} and V_{oc} determine the operation range of the cell, which is determined by the current-voltage (IV) curve of the cell. The relation between the I_{sc}, V_{oc} and MPP can be seen in Figure 2.4, which shows the IV-curve with its corresponding power-voltage (PV) curve. The optimal operating voltage V_{mp} of the cell is determined from the maximum of the PV-curve P_{mp}. The V_{mp} will determine the optimal output current I_{mp} from the cell.

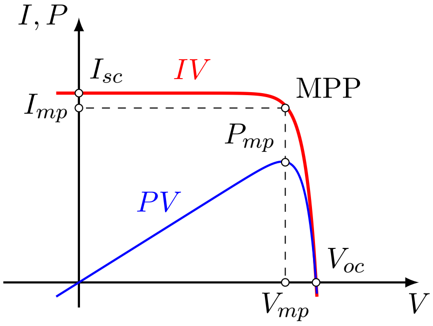

Figure 2.4: IV curve (red) with corresponding PV curve (blue) of an illuminated solar cell. The operating range of the cell is defined by the short-circuit current I_{sc} and the open-circuit voltage V_{oc}. Within the operating range, the optimal operating point of the cell is found at the MPP determined by $P_{mp} = I_{mp}V_{mp}$.

Typically, several solar cells are placed in a gridded pattern onto a flat surface called a module. In this thesis all solar cells used within a module and system have identical properties. When connecting solar cells together to form a module, the operating range changes based on the connection pattern between the cells. The changes in the operating range are dictated by Kirchoff's circuit laws. By Kirchhoff's current law,

$$\sum_{i=1}^{N} I_i = 0, \tag{2.5}$$

the sum of all N currents at any circuit junction is zero. By Kirchhoff's voltage law,

$$\sum_{i=1}^{N} V_i = 0, \tag{2.6}$$

the sum of all N voltages in a closed circuit loop is zero. When connecting solar cells with identical properties in series, the number of nodes remain the same but the number of voltages in a circuit loop increases; connecting solar cells in series increases the V_{oc} as the sum of each cell's open-circuit voltage but does not alter the I_{sc}. When connecting solar cells in parallel, the number of voltages in any closed circuit loop remains the same but the number of currents at the new connection nodes increases; connecting solar cells in parallel increases the I_{sc} as the sum of each cell's closed-circuit current but does not alter the V_{oc}. When connecting the cells as a mix between parallel and series connections, one can increase both the short-circuit current and the open-circuit voltage of the module. Usually, cells within a module are connected in series as a low current minimises resistive losses since

$$P = IV = I^2R. \tag{2.7}$$

Kirchhoff's laws apply when connecting modules together to form PV arrays as well. In this thesis, a PV array is a number $N \geq 1$ of series-connected modules that are operated together. A PV array outputs direct current (DC) and so the operation point of an array is controlled by a DC-DC converter connected to the array circuit. DC-DC converters apply tracking algorithms to find the MPP based on the array performance. The DC-DC converter varies the operating voltage of the array based on the tracking algorithm's output to maximise the power generation from the PV array. The output DC current of the PV array is transformed into alternating current (AC), by use of a DC-AC inverter connected to the circuit, to harvest the current since the electrical grid and most appliances use AC.

The most important factor for PV array power generation is the incoming irradiance on the array cells. In PV arrays, the modules are placed such that they receive the same plane of array (POA) irradiance. The POA irradiance depends on the position of the sun as well as the orientation of the module in question. To find the POA irradiance, the module orientation is described in terms of its azimuth angle φ, i. e. the direction which the module faces defined as the angle east of north, and its tilt angle Θ with respect to the ground horizontal. By convention, the azimuth angle is defined as angles east from north, for example a module with an azimuth of $\pi/4$ indicates that the module is facing due east. The tilt and azimuth angles can be determined from the three-dimensional surface normals $\vec{n} = (x, y, z)$ of the modules. The relations between the surface normal of a module with its tilt and azimuth, as well as the cardinal coordinates, are shown in Figure 2.5. To find the azimuth I first find the angle α formed between the x and y coordinates of the surface normal

$$\alpha = \arctan\left(\frac{x}{y}\right), \tag{2.8}$$

where $\alpha = \pi/2$ if $y = 0$. The angle α is shown in Figure 2.5. The azimuth is then found by placing the resulting angle α in the corresponding quadrant

$$\varphi = \begin{cases} \alpha, & x \geq 0 \wedge y > 0 \\ \pi/2 - \alpha, & x > 0 \wedge y \leq 0 \\ \pi/2 + \alpha, & x \leq 0 \wedge y < 0 \\ 2\pi - \alpha, & x < 0 \wedge y \geq 0 \end{cases}. \tag{2.9}$$

The tilt of the module is then found through

$$\Theta = \arctan\left(\frac{\sqrt{x^2 + y^2}}{z}\right). \tag{2.10}$$

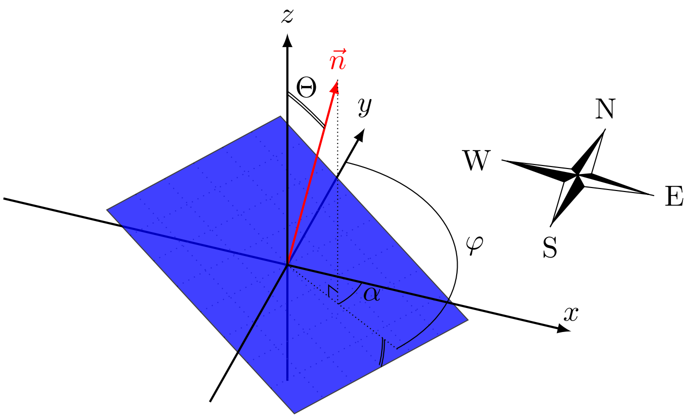

Figure 2.5: Tilt Θ and azimuth φ of a module with surface normal $\vec{n}$. The azimuth is dependent on the angle between the coordinate system of the module and the cardinal coordinates, here the y-axis of the module's coordinate system is aligned with the north-south axis. The angle α is the angle between the projection of $\vec{n}$ to the xy-plane and the x-axis, which is used to find the resulting azimuth. The double-drawn angle signifies the two angles have the same size Θ.

With the azimuth and tilt, the POA irradiance on a module is calculated as

$$E_{\text{POA}} = E_b + E_g + E_d, \tag{2.11}$$

where E_b is the decomposed direct normal irradiance normal to the module surface, E_g is the incident irradiance reflected from the ground and E_d is the incident radiation after diffusion effects provoked by the environment. The beam component E_b is determined from

$$E_b = \text{DNI} \cdot \cos\left(\alpha_i\right), \tag{2.12}$$

where α_i is the angle of incidence between the sun and the module and DNI is the direct normal irradiance. The DNI is extracted from the measured global horizontal irradiance (GHI), while the angle of incidence is determined from

$$\alpha_i = \arccos\left(\cos\left(Z_{\text{sun}}\right)\cos\left(\Theta_{\text{module}}\right) + \sin\left(Z_{\text{sun}}\right)\sin\left(\Theta_{\text{module}}\right)\cos\left(\varphi_{\text{sun}} - \varphi_{\text{module}}\right)\right), \tag{2.13}$$

where Z_{sun} is the sun zenith angle and φ_{sun} is the sun's azimuth angle, both with respect to the module's geographical location. The ground reflected irradiance E_g is determined from

$$E_g = \text{GHI} \cdot \varepsilon \frac{1 - \cos\left(\Theta\right)}{2}, \tag{2.14}$$

where ε is the ground reflectivity known as albedo. There is no ground truth to determine the diffuse irradiance E_d as it results from complex processes which involve the scattering of radiation, the irradiance from the sky dome, and other processes[4]. However, there exists several well established models that determine E_d [22, 36, 39]. The current generated by the cells in a module is determined based on its POA irradiance.

---

[4] Radiation is diffused and redirected in the atmosphere. Consider if you will: when you stand in a shadow outside in a field there is still light reaching you (more than what is reflected from the ground).

2.1.3 Mismatch effects

When operating one or more solar modules within an array, differences in incoming irradiance on cell and module level affect the performance and power output of the array. If all cells in an array receive the same amount of irradiance, then all cells generate the same current and the array can be operated optimally. However, if the cells in an array receive different irradiance levels, then the cells will generate different current levels which negatively affects the power generation of the array. Figure 2.6 shows IV-curves for a solar cell with two different irradiance conditions: the red IV-curve corresponds to the highest possible irradiance on the cell at a given time and the blue IV-curve corresponds to the same cell receiving less irradiance, for example due to a shadow. Both the operating range and the MPP of the solar cell are reduced when the irradiance on the cell diminishes. By Kirchhoff's current law, the circuit current through series connected cells must be the same for all cells. As such, the series connected circuit of solar cells will have a current limited by the worst performing cell.

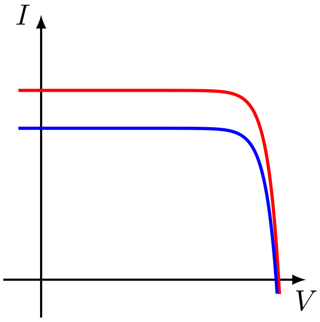

Figure 2.6: IV curves of a solar cell under two different irradiance conditions. The condition where the cell receives more irradiance is represented by the red curve, while the condition where the cell receives less irradiance is represented by the blue curve. The diminished irradiance shifts the IV curve such that both the V_{oc} and I_{sc} are reduced.

The effect of irradiance mismatch between cells can be seen in the resulting IV- and PV-curves of the array as seen in Figure 2.7 and Figure 2.8 for two series-connected cells. The IV-curve of the array is constructed by stacking the individual IV-curves of the cells following Kirchhoff's laws for each circuit component. The IV-curve of series-connected circuit parts is found by aligning their current levels, starting from the highest current point among all cells in the series. The voltage of the series is obtained by adding each cell's voltage contribution at these aligned current points. The I_{sc} of an array of series-connected circuit components is dictated by the lowest I_{sc} in the array. In effect, the IV-curves of the cells are stacked in the direction of increasing potential (left to right in Figure 2.6), starting with the IV-curve with the highest I_{sc} as done in Figure 2.7. The IV-curve of parallel-connected circuit parts is found by aligning their voltage levels, starting from the highest current point compatible among all cells. The current of the circuit is obtained by adding each cell's current contribution at these aligned voltage points. The V_{oc} of an array of parallel-connected circuit components is dictated by the lowest V_{oc} in the array. Stacking IV-curve in parallel connections is practically similar to stacking in series connections, where the curves are stacked in the direction of increasing current starting with the IV-curve with the largest V_{oc}. Figure 2.7 shows how a mismatch between two series-connected solar cell affects their combined IV-curve. Stacking together the two different curves from Figure 2.6 yields the blue curve in Figure 2.7. Stacking together two cells with IV-curves represented by the red curve in Figure

2.6 yields the red curve in Figure 2.7. The two IV-curves in Figure 2.7 have different MPPs and thus deliver different power. The respective PV-curves of the IV-curves in Figure 2.7 can be seen in Figure 2.8. The power loss due to mismatch of an array is the difference in MPP between the case where all cells receive the same reference irradiance to when one or more cells receive less than the reference irradiance. Here, the reference irradiance is the highest irradiance received by a cell in the array. A reduction in output power results in a reduction of generated energy: energy losses due to different currents or voltages between cells are called *mismatch losses*.

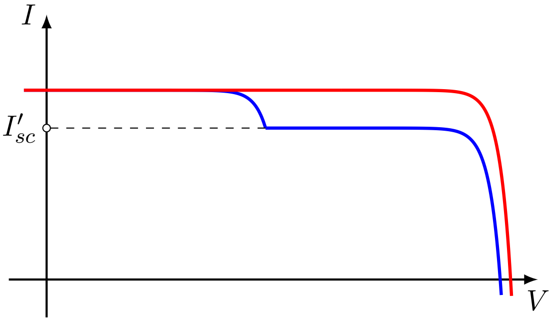

Figure 2.7: Combined IV curves of two series-connected solar cells under two different irradiance scenarios. The red curve corresponds to both cells receiving the same irradiance as given by the red curve in Figure 2.6. The blue curve corresponds to one cell receiving irradiance as given by the blue curve in Figure 2.6, while the other cell receives a higher irradiance, given by the red curve in Figure 2.6. The I_{sc} of the blue curve, denoted I'_{sc}, is dictated by the least performing cell.

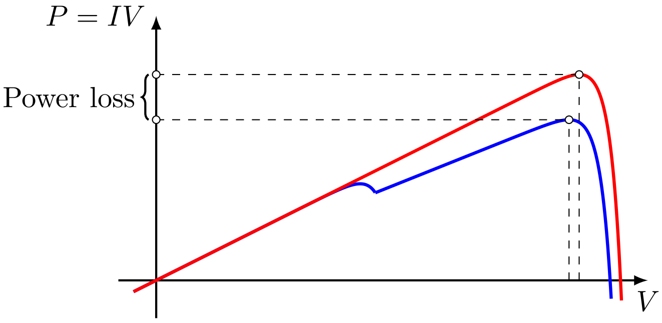

Figure 2.8: PV curves of two series-connected solar cells under two different irradiance scenarios. The red curve corresponds to the red curve in Figure 2.7. The blue curve corresponds to the blue curve in Figure 2.7. The different P_{mp} are marked with white circles. The ideal scenario for the two-cell array at a given moment is represented by the red curve, where both cells receive the same high irradiance. The difference in P_{mp} between the red and blue curves represents the power loss due to mismatch with respect to the ideal scenario. The different optimal operating voltages for the two curves is dictated by the resulting V_{oc} for each curve.

One way to reduce the effects of mismatch between cells is through the placement of bypass diodes in the module and array circuit. One such effect is a temperature increase in the mismatched cell called hot-spot heating, which can lead to permanent damage to the mismatched cell and module. Bypass diodes are placed in parallel to the circuit parts for which they are to mitigate the mismatch effects. Figure 2.9 shows a bypass diode placed to mitigate the mismatch effect of a solar cell connected in series. A forward bias is applied to the bypass diode if the cell 'covered' by the bypass diode generates

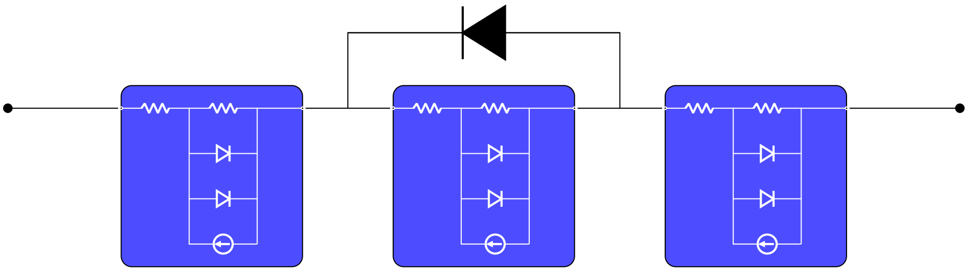

Figure 2.9: A bypass diode (in black) placed to mitigate current mismatch of a solar cell with the rest of the circuit. If the left and right cells receive a higher irradiance than the middle cell, and the difference is such that the potential at the bypass diode is larger than V_b, the bypass diode will be forward biased and will open an alternate circuit path. The alternate circuit path mitigates the current mismatch of the middle cell with the rest of the circuit.

less current than the other cells. The bypass diode closes the circuit around the cell if the applied forward bias to the diode exceeds the activation voltage V_b. The activated bypass diode creates an alternate circuit path for the excess current when activated, thereby maintaining the operating current and voltage of the system, and protecting the mismatched cell from hot-spot heating. Installing bypass diodes for each cell in a module is expensive; bypass diodes are typically placed to cover for several cells at a time. Mismatch losses due to different irradiance on the cells of a module are typically due to partial shading conditions (a passing cloud, a bird resting on the module, the shadow of a tree, etc.) or soiling (dust or dirt setting on the modules).

2.1.4 Wave-induced losses

Mismatch losses can also occur between series connected modules where all the cells in each individual module performs equally, f. ex. two series-connected modules where one is completely shaded and the other is not. In the case of FPV, where modules can be placed on different moving floats, the modules will have varying and different pitch, roll and yaw due to the interaction of the incoming waves with the individual floats. Pitch, roll and yaw signify rotations around the three-dimensional axes as shown in Figure 2.10. The rotations are with respect to the reference frame of each individual module. For example, in Figure 2.5 the module has Θ in pitch and α in yaw and zero roll. Assuming

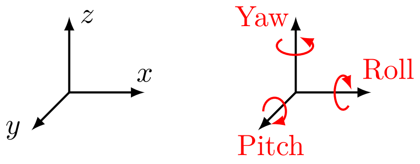

Figure 2.10: Rotation around the three-dimensional axes defined as pitch, roll and yaw. Here the positive x direction is defined to be the front of a float.

an array consisting of several floats, the modules on the different floats will have different and varying rotations around the axes in the presence of waves. The resulting module orientation can be described by the resulting surface normal of the module, which in turn can be translated to the module tilt and azimuth through (2.10) and (2.9). The varying surface normals of the modules will lead to different POA irradiance for the modules on different floats. Figure 2.11 illustrates a situation where a module on one float is rotated such that it has a smaller area of incidence with the sun in comparison to a module on a different float.

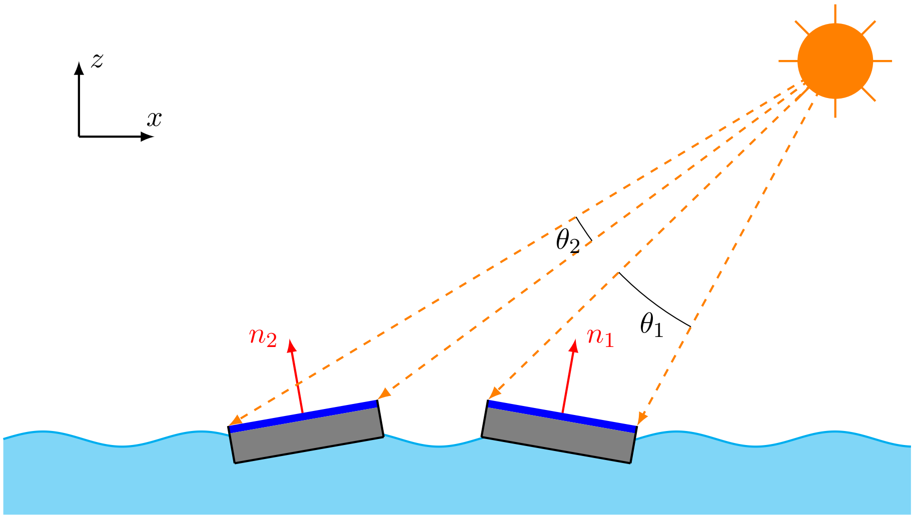

Figure 2.11: Two FPV modules receiving different irradiance from the sun due to the tilt induced by the waves. The module with surface normal n_2 is tilted away from the sun yielding an incident angle θ_2 for the irradiance from the sun. The module with surface normal n_1 is tilted toward the sun yielding an incident angle θ_1 for the irradiance from the sun. Since $\theta_1 > \theta_2$, the module tilted away from the sun will generate less current than the module tilted toward the sun. Connecting these modules in series results in a mismatch induced by waves where the power loss is exemplified in Figure 2.8.

The total energy loss from FPV modules receiving different POA irradiance due to incoming waves is called *wave-induced loss* (WIL). As a reminder, the relation between power and energy as

$$E(t_i) = P(t_i)(t_i - t_{i-1}), \tag{2.15}$$

where t is the time and the indices i represent timestamps for measurements. The WIL can be split into the *wave-induced mismatch loss* (WIML) and the *wave-induced irradiance loss* (WIIL). The terms WIML and WIIL have not been explicitly defined prior to this thesis. The WIML is the energy loss of an FPV array due to electrical mismatch between the modules provoked by incoming waves. I consider the WIML to be an electrical loss. The WIIL is the energy loss due to different total irradiance incoming on an FPV array in the presence of waves compared to the same FPV array but in the absence of waves, i.e. a static array. I consider the WIIL to be an optical loss. The WIL, WIML and WIIL are expressed as percentage losses. I define the WIL as

$$\mathrm{WIL} = \frac{E^s - E^f}{E^s}, \tag{2.16}$$

where E^s is the energy production of the FPV array in the absence of waves (s for static) and E^f is the energy production of the FPV array when it interacts with waves. In (2.16), as a modification to the definition in [35], the WIL can be either positive or negative depending on the overall energy-yield. From (2.16), the loss is expressed as a positive percentage if $E^f < E^s$; a negative loss represents an over-performance of the FPV array compared to a similar, but static, PV array. I define the WIIL as

$$\mathrm{WIIL} = \frac{E^s - \sum_i^N E_i^f}{E^s}, \tag{2.17}$$

where $\sum_i^N E_i^f$ is the sum of the individual modules' energy production in an FPV array of N modules without considering the mismatch mechanisms. One can consider $\sum_i^N E_i^f$ as being the sum of the energy production of an FPV array in the case where each module has its own DC-DC converter and AC-DC inverter and are not connected with the other array modules. In (2.17), a negative loss means the FPV array has received more total irradiance than in the absence of waves. I define the WIML as

$$\mathrm{WIML} = \frac{\sum_i^N E_i^f - E^f}{\sum_i^N E_i^f}, \tag{2.18}$$

where the loss is a percentage with respect to the FPV array without mismatch effects. In (2.18), a positive loss expresses the energy lost purely to mismatch effects. The WIML cannot be negative, as it is not possible for an FPV array to produce more energy than all of its individual modules' energy production combined. The best-case scenario for the mismatch losses is WIML= 0% where all the modules have the same POA irradiance at all times. The WIIL may be non-zero in the case of WIML= 0% as the FPV array may still follow a movement dictated by incoming waves. WIML= 0% means simply that all the modules move in unison and as a result receive the same POA irradiance. To express the WIL as a sum between the WIML and WIIL, the WIML must be corrected to account for the irradiance difference

$$\frac{E^s - E^f}{E^s} = \left(\frac{\sum_i^N E_i^f - E^f}{\sum_i^N E_i^f}\right)\frac{\sum_i^N E_i^f}{E^s} + \frac{E^s - \sum_i^N E_i^f}{E^s}. \tag{2.19}$$

2.2 Sea surface data

To model and assess the performance of an FPV system at a particular location it is necessary to model the water surface at the location. The datasets needed to simulate the movement of floats caused by incident waves depend on the technique used to simulate the float movement. While some methods may only require wave heights and periods, others may require a complete wave spectrum. The wave spectrum is presented in section 2.2.4. The wave spectrum can be estimated from wind measurements or recreated from sampled sea-state variables such as wave heights and periods. It is preferable to have a complete time-series dataset of the necessary sea-state variables. Such a time-series can be obtained through different means: one can consider data from buoys, satellites, reanalysis, physical models or extrapolate tabulated sea state data based on wind measurements [1, 19]. Each data source has its benefits and drawbacks. The above-mentioned methods are considered in turn, with the exception of extrapolation of sea-states from other measurements, for getting sea surface data at a specific location with their benefits and drawbacks.

2.2.1 Buoys

Measurement buoys can obtain accurate sea-state data for a specific location. There are two main types of buoys to aquire sea state data: drifting and moored buoys. Drifting buoys are considered inexpensive and have an expected lifetime of 1 year to 18 months [13]. As the name suggests, drifting buoys drift with the sea current, which makes them unreliable for collecting data at a single location over time. Moored buoys, on the other hand, are anchored and do not drift from their deployment location. They are more expensive than drifting buoys but can gather more data than drifting buoys and have a significantly longer lifetime of 10+ years [31]. For the purpose of collecting sea-state data for FPVs, moored buoys are better suited than drifting buoys.

With enough resources and time, a buoy can be deployed to gather the necessary data over a desired period of time at a location where one intends to assess the performance of an FPV system. The data acquired by the buoy can then be used to simulate the movement of FPVs. A drawback of such a process is that gathering the data to run the desired simulation is time-consuming. An alternative to such a process is to use already deployed buoys given that they are placed at or close enough to the desired location, for example within the same bay. These buoys must be online, give access to their collected data through the institution that monitors them, and collect the relevant data to simulate the FPV system's movement. Two websites that grant a map of, and access to, several existing buoys are https://www.ndbc.noaa.gov/obs.shtml and https://co-en.ifremer.fr (accessed 2025-02-17).

As an additional case, buoys can be deployed to measure sea-state variables where FPV installations already exist. Gathering production and movement data from the FPV system where a buoy gathers sea-state data would allow for a near-exact assessment of the impact of waves on the FPV system.

2.2.2 Satellites

Satellite observations can provide measurements of sea-state variables with high spatial resolution. However, they usually cannot provide a continuous time-series of measurements for a fixed geographical location as most altimeter satellites are not geostationary. A way to obtain a time series of the desired variables is through the combination of measurements from different satellites that pass over the location of interest. The resolution, in both time and space, of the resulting dataset at the location will then be determined by the number of satellites that pass over the specific area, their measurement apparatus, altitude, angle with respect to the desired location, and their repeat period.

A study from 2017 [48] created a time-series dataset of significant wave height with a 30 minute time resolution and 50km × 50km spatial resolution over the East/Japan Sea. To achieve this they used nine altimeter mission datasets from Institut Français de Recherche pour l'Exploitation de la Mer (IFREMER): European Remote Sensing-1 [16], Topography Experiment/Poseidon [45], European Remote Sensing-2 [17], Geosat Follow-On [6], Joint Altimetry Satellite Oceanography Network-1 [43], Environmental Satellite [15], Joint Altimetry Satellite Oceanography Network-2 [26], Cryosat-2 [9], and Satellite for Argos and Altika [40]. These satellites have different repeat periods[5], altitudes, inclination, and mission time. The difference in altitude, inclination and repeat periods as well as the satellites having different orbit paths limit the spatial coverage and resolution of an area. The different satellite missions also have different mission periods which limits the spatial resolution further, as the number of satellites covering the area of interest during any time period is limited. To obtain a good enough time-series dataset of sea-state variables using satellite data for finer geographical areas is challenging. For instance, gathering sea surface data from within any mainland Norwegian fjord using satellites would require more work than that done by [48], as it would require a higher spatial resolution.

---

[5] The time a satellite takes to come back to the same geographical location.

IFREMER provides a dataset with multiple sea-state variables collected through satellite observations at a monthly time resolution and spacial resolution of 1° [37]. [48] explored the evolution of the significant wave height for East/Japan Sea and compared the altimeter datasets with buoy data and found that data from IFREMER had a bias smaller than 0.1m in the significant wave height. If the location in question can use a 1° spatial resolution, then the data from IFREMER would be well suited.

2.2.3 Reanalysis

Reanalysis datasets provide a consistent spatial and temporal resolution by combining past short-term forecasts with observations. The observations used for reanalysis may come from satellites, buoys, and other data collection techniques. In reanalysis datasets the irregularities from the data gathered from observations are completed by interpolating short-term forecasts, thus granting a coherent long-term dataset of past weather. The short-term forecasts are done such that they fit the observations to provide consistent data. In the case where reanalysis datasets have the desired spatial resolution for the chosen FPV system location, such as offshore areas, then using data from reanalysis datasets is a simple and effective way to get sea-surface and sea-state data.

The European Centre for Medium-Range Weather Forecasts (ECMWF) provides several reanalysis datasets, one of which is the ERA5 dataset [23]. The ERA5 dataset contains sea-state variables with an hourly temporal resolution. The spatial resolution is $0.25° \times 0.25°$ on land and $0.5° \times 0.5°$ to $1° \times 1°$ otherwise. Another reanalysis dataset with $3\text{km} \times 3\text{km}$ spatial resolution for the Norwegian coast and the north sea is NORA3 [21] provided by the Norwegian Meteorological Institute (MET). The NORA3 dataset provides the same sea-state variables as ERA5, as NORA3 is in effect a downsampling of the ERA5 dataset, NORA3 is therefore a better suited dataset if the FPV system location is along the Norwegian coast. If the FPV system location requires a smaller spatial resolution than $3\text{km} \times 3\text{km}$, one can use wave models to model the sea-state at the desired location utilising the data from the available reanalysis datasets.

2.2.4 Wave models

Physics driven wave models can model the sea-states where the resolution of existing datasets is unsatisfactory for the desired location. Third generation wave models are extensively used for hindcast and forecast modelling of the generation, decay and transport of waves. Wave models yield a statistical description of the sea surface as sea surface waves are random in nature: an exact description of the sea surface evolution is not possible. The wave models model the sea surface evolution and find the water surface energy distribution called the wave energy spectrum. The wave energy spectrum grants a statistical description of the sea surface as a distribution of the wave energy over a set of coordinates such as wave frequency and propagation direction. Third generation wave models explicitly model weak non-linear interactions as opposed to second generation models which include non-linear interactions in a parametrised form. Non-linear interactions are considered weak when they do not cause dramatic changes in the wave energy distribution. The wave models find the wave energy spectrum by solving the action balance equation presented below.

The most well-established third generation wave models are: Wavewatch III (WW3) [44], Wave Model (WAM) [28] and Simulating Waves Nearshore (SWAN) [3]. WAM and WW3 were developed for ocean wave modelling and are therefore more applicable for modelling large water bodies. Both models employ explicit time-integration schemes when solving the action balance equation which impose the CFL convergence conditions. These convergence conditions increase the number of required time steps for increasing spatial resolution making the models computationally costly for fine spatial resolutions. Originally, WAM and WW3 did not include coastal or shallow-water effects, however the models have been expanded to include such interactions. The SWAN model was developed to specifically handle coastal and shallow-water effects. The SWAN model applies a fully implicit time-integration scheme which is unconditionally stable. This implicit scheme allows SWAN to solve the sea-state evolution at high spatial resolution with larger time steps than WAM and WW3, thus reducing the computational requirements. All three models are continuously improved upon to include more complex interactions and different integration schemes. Which model to use when modelling sea-states becomes a matter of preference as they all perform well and similarly [2].

Practically, WW3 provides a flexible framework while having a more complex setup compared to SWAN and WAM. SWAN has a simple setup and can be run nested within WAM or WW3. A nested run is a simulation performed by WAM or WW3 on a large area to provide boundary data for SWAN to perform simulations with a higher spatial resolution for an area of interest. This way one can perform sea-surface modelling without external wave spectrum datasets. Nested runs are unnecessary when data is available to be used as forcing and boundary terms within the computational region. In this thesis, I use SWAN with existing datasets for wind and boundary energy spectra where the setup and modelling is facilitated by the `dnora` python package (developed by MET).

The action balance equation

The third generation wave models find the evolution of sea-states by solving the action balance equation. The solutions to the action balance equation give the energy density spectrum at every point on the grid of interest. From a wave spectrum, one can simulate a statistically similar sea surface where the movement of the floats and modules can be calculated. In order to understand what the wave spectrum is and what the action balance equation describes I present a simple derivation of the action balance equation. I follow the detailed derivation found in [28, Chapter 1] from basic assumptions about the sea surface. In this derivation, I employ the plural form ‘we’ to include the reader in the process.

The derivation is performed in the two-dimensional horizontal plane as only the wave energy at the sea surface is of interest. For vector notation I use $\vec{x} = (x_1, x_2)$, where x_i for $i = \{1, 2\}$ are our two horizontal orthogonal space coordinates. Differentiation by a scalar is indicated by

$$\partial_t = \frac{\partial}{\partial t}, \tag{2.20}$$

where t is the scalar in question, this example employed the time t. Differentiation by a vector is indicated by a nabla ∇ with the corresponding vector subscript

$$\nabla_{\vec{x}} F(\vec{x}) = (\partial_{x_1} F, \partial_{x_2} F), \tag{2.21}$$

where $F(\vec{x})$ is here an exemplary function.

We start the derivation of the action balance equation by considering free linear wave components. A wave component is free if it can propagate through a medium without being affected by its environment. The wave components can be described by an amplitude a, a wavenumber $\vec{k} = \{k_1, k_2\}$, a frequency ω and a phase function, or eikonal, $s(\vec{x}, t)$ and can be expressed as

$$\eta\left(\vec{x}, t\right) = a\left(\vec{x}, t\right) e^{is(\vec{x},t)}, \tag{2.22}$$

where η is the water surface elevation at $(\vec{x}, t)$. The eikonal is given by

$$s\left(\vec{x}, t\right) = s(0,0) + \vec{x} \cdot \nabla_{\vec{x}} s + t\partial_t s, \tag{2.23}$$

which is related to the wavenumber through

$$\vec{k}\left(\vec{x}, t\right) = \nabla_{\vec{x}} s, \tag{2.24}$$

and to the frequency through

$$\omega\left(\vec{x}, t\right) = -\partial_t s. \tag{2.25}$$

In (2.22), both the eikonal and amplitude are allowed to vary in space and time. Since we are considering linear wave components the variations will depend on the water depth and other linear interactions between wave components. We assume the wave components propagate such that the variations in depth and wave properties are slow with respect to the wave components' wavelength and period; we treat the wave components as adiabatic invariants. From (2.23), (2.24) and (2.25) we get the consistency relation

$$\partial_t \vec{k} + \nabla_{\vec{x}} \omega = 0. \tag{2.26}$$

Water waves are dispersive, components with different wavenumbers propagate at different velocities, and so the dispersion relation dictates

$$\omega_{\pm}\left(\vec{x}, t\right) = \Omega\left[\vec{k}\left(\vec{x}, t\right), \vec{U}\right] = \vec{k} \cdot \vec{U} + \sigma_{\pm}\left[\vec{k}\left(\vec{x}, t\right), h(\vec{x})\right], \tag{2.27}$$

where Ω is a functional for the frequency, $\vec{U}$ is the local water current, and σ is defined as

$$\sigma_{\pm}\left[\vec{k}\left(\vec{x}, t\right), h(\vec{x})\right] = \pm\sqrt{g\vec{k}\tanh\left(\vec{k}h\right)}, \tag{2.28}$$

where g is the gravitational acceleration and h is the distance from the water surface to the sea floor. The term $\vec{k} \cdot \vec{U}$ in (2.27) accounts for the Doppler shift caused by a current $\vec{U}$. Local water currents cause a Doppler shift to the wave components with respect to a stationary observer (at a fix $\vec{x}$), the relative wave velocity between the observer and wave component changes. One can solve the time evolution of the eikonal numerically: given an initial state $s(\vec{x}, 0)$ one determines $\vec{k}(\vec{x}, 0)$ through (2.24) and then solve (2.26) for the subsequent time steps. The time evolution of the amplitude a is derived in detail by Whitham in [46, Chapter 11]. Here I provide a shortened derivation. In essence, (2.22) is substituted in the Lagrangian which is then used in an average variational principle

$$\delta \iint \mathscr{L}(\omega, \vec{k}, a) dt d\vec{x} = 0, \tag{2.29}$$

for the functions $a\left(\vec{x}, t\right)$ and $s\left(\vec{x}, t\right)$. The variational equations from (2.29) are

$$\delta a : \quad \mathscr{L}_a = 0 \tag{2.30}$$

$$\delta s : \quad \partial_t \mathscr{L}_\omega - \nabla_{\vec{x}} \mathscr{L}_{\vec{k}} = 0, \tag{2.31}$$

where we can rewrite (2.31) as

$$\partial_t N + \nabla_{\vec{x}}[\vec{v}_D N] = 0, \tag{2.32}$$

with

$$N\left(\vec{x},t\right) = \frac{2|a\left(\vec{x},t\right)|^2}{\sigma}, \tag{2.33}$$

and

$$\vec{v}_D = \nabla_{\vec{k}}\Omega = \vec{U} + \vec{c}_g = \vec{U} + \nabla_{\vec{k}}\sigma\left(\vec{k}((\vec{x},t))\right), \tag{2.34}$$

where $\vec{v}_D$ is called the propagation velocity and $\vec{c}_g$ is the group velocity which for a single wave component is the phase velocity. Following Whitham's arguments, the wave action is expressed as

$$A = \rho g \int N\left(\vec{x},t\right) d\vec{x}, \tag{2.35}$$

from which we have the wave action density $\rho g N\left(\vec{x},t\right)$, where ρ is the water density. For simplicity we refer to the wave action density as $N\left(\vec{x},t\right)$ since water is incompressible which means $\rho g =$ constant. In this manner, (2.32) takes the form of a conservation law which expresses the conservation of the wave action A. From our intial assumption that the wave properties and depth vary slowly with respect to the wavenumber and period we have that A is an adiabatic invariant.

The sea surface consists of a large number $\mathcal{N} \gg 1$ of wave components, since we assume linear wave components we can superpose components as

$$\eta\left(\vec{x},t\right) = \sum_{n}^{\mathcal{N}} a_n\left(\vec{x},t\right) e^{i(\vec{k}_n(\vec{x},t)\cdot\vec{x} - \omega_n(\vec{x},t)t)} + \text{small corrections}, \tag{2.36}$$

where the small corrections are attributed to non-linear corrections which have a small dynamical significance and are thus neglected. The dynamical significance is low because the non-linear corrections affect the wave height and steepness of the wave components rather than their dynamics. To include the non-linear interactions one has to move away from linear wave theory to higher order wave approximations such as Stokes wave theory. The effects of non-linear interactions are included as sourcing terms in the action balance equation. The wave components are considered to be dynamically independent, i.e. each component evolves independently of other components. To describe the wave field with (2.36) we must assume that all a_n are independent and yield the same average values. The wave components can be considered distinct and independent if we assume that all components at a point $\vec{x}$ have converged to that point from distant and different origins. The wave field can be considered quasi-homogenous and quasi-stationary[6] since all wave components are independent and yield the same average values. With independent components yielding the same average values, the central limit theorem states that the wave field, given by (2.36), is Gaussian.

We can express (2.36) in a continuous form as

$$\eta\left(\vec{x},t\right) = \int_{-\infty}^{+\infty} \hat{\eta}(\vec{k},t) e^{i\left(\vec{k}\cdot\vec{x} - \omega t\right)} d\vec{k} + \text{small corrections}, \tag{2.37}$$

---

[6] The variations in the wave field are slow with respect to the wavenumbers and periods.

where $\hat{\eta}$ is the Fourier inverse of η for the wavenumbers $\vec{k}$. We can discretise the amplitude for wavenumber intervals as

$$a_{\vec{k}} = \int_{\vec{k}-\Delta\vec{k}/2}^{\vec{k}+\Delta\vec{k}/2} \hat{\eta}(\vec{k})d\vec{k}, \tag{2.38}$$

where $\Delta\vec{k}$ is an arbitrary wavenumber interval, the subscript $\vec{k}$ does not indicate a derivative in this case, the subscript indicates here the pertaining wavenumber to the amplitude a. We relate (2.38) to the discrete wave action density

$$N_{\vec{k}} = \frac{2\left|a_{\vec{k}}\right|^2}{\sigma_{\vec{k}}}. \tag{2.39}$$

In the continuous case we have

$$N(\vec{k},\vec{x},t)\Delta\vec{k} = \sum_n N_n \varepsilon(\vec{k}-\vec{k}_n), \quad \varepsilon(\vec{k}) \begin{cases} 1, & \text{if } -\frac{1}{2}\Delta\vec{k} < \vec{k} < \frac{1}{2}\Delta\vec{k} \\ 0, & \text{otherwise} \end{cases}. \tag{2.40}$$

We relate the wave action density to the wave energy density through

$$N\left(\vec{k},\vec{x},t\right) = \frac{E\left(\vec{k},\vec{x},t\right)}{\sigma}, \tag{2.41}$$

indeed we have that the average energy of the system at a particular point in time and space $(\vec{x},t)$ is given by

$$\bar{\mathscr{E}} = \rho g \int E(\vec{k})d\vec{k}. \tag{2.42}$$

Both $E\left(\vec{k},\vec{x},t\right)$ and its discrete counterpart are known as the wave energy spectrum. With a Gaussian wave field, the expectation value of the surface height at a certain point is given by the total energy

$$<\eta^2>= \int E(\vec{k})d\vec{k}, \tag{2.43}$$

so we can find the wave energy spectrum through the evolution of the wave amplitudes. In the Gaussian wave field, each wave component n conserves their wave action separately [47] as

$$\partial_t N_n + \nabla_{\vec{x}} \cdot \left[\nabla_{\vec{k}}\omega_n N_n\right] = 0, \quad N_n = \frac{2|a_n|^2}{\sigma_n}, \tag{2.44}$$

which is the same as (2.32). In (2.44), the wavenumber of each component n may vary and so the density of $\vec{k}$-modes will also vary at $\vec{x}$. As shown in [47], we can write (2.44) in a continuous form and since we now have a varying wavenumber density in $N\left(\vec{k},\vec{x},t\right)$, we get an additional term with $\partial_t\vec{k}$

$$\partial_t N + \partial_t\vec{k} \cdot \nabla_{\vec{k}} N + \nabla_{\vec{x}} \cdot \left[\nabla_{\vec{k}}\omega_n N\right] = 0. \tag{2.45}$$

Practically, one finds the energy spectrum in the frequency-directional coordinates, as done in the SWAN wave model, rather than in the wavenumber coordinates. We can switch the coordinates of (2.45) to the frequency-directional spectrum and (2.45) will still hold according to [28]. To switch to the frequency-directional domain, we define the frequency f and direction of propagation of the waves θ as

$$f = \frac{\sigma\left(\left|\vec{k}\right|\right)}{2\pi}, \quad \theta = \mathrm{atan2}(k_{x_1}, k_{x_2}), \tag{2.46}$$

where (k_{x_1}, k_{x_2}) are the wavenumber components along the space axis coordinates. The energy spectrum is given by

$$E(f,\theta) df d\theta = E(\vec{k}) d\vec{k}. \tag{2.47}$$

The action conservation in continuous form can then be expressed as

$$\partial_t N + \partial_t f \cdot \nabla_f N + \partial_t \theta \cdot \nabla_\theta N + \nabla_{\vec{x}} \cdot \left[\nabla_{\vec{k}} \omega_n N\right] = 0, \tag{2.48}$$

which, omitting the sourcing terms, is the expression used within the SWAN wave model. One can express the frequency-directional spectrum in terms of frequency only as

$$E(f) = \int_0^{2\pi} E(f,\theta) d\theta, \tag{2.49}$$

from which we can extract the moments of the spectrum

$$m_p = \int_0^{\infty} f^p E(f) df, \tag{2.50}$$

where p signifies the p^{th} moment. From the spectrum moments we can find sea-state variables such as the significant wave height and the wave periods among others. The zeroth moment is used to find the significant wave height is given straight from (2.43) as

$$m_0 = \int_0^{\infty} E(f) df =< \eta^2 >, \tag{2.51}$$

from which the significant wave height can be found through

$$H_s = 4\sqrt{m_0}. \tag{2.52}$$

The homogenous equation (2.48) can be considered the action balance equation without forcing terms. The non-linear forcing terms are included based on the assumption that they are weak-in-the-mean. A weak-in-the-mean process may have high non-linearity locally but yield low impact on average. As long as the forcing terms are weak-in-the-mean they can be approximated to a quasi-linear sourcing term. Each process must be described with its individual sourcing term, the sourcing terms can then be added linearly to (2.48) which becomes inhomogenous

$$\partial_t N + \partial_t f \cdot \nabla_f N + \partial_t \theta \cdot \nabla_\theta N + \nabla_{\vec{x}} \cdot \left[\nabla_{\vec{k}} \omega_n N\right] = \sum_i S_i, \tag{2.53}$$

where the subscript i differentiates the sourcing terms between the different processes and S_i is the i^{th} sourcing term. Using (2.34) in (2.48) we get the action balance equation

$$\partial_t N + \nabla_{\vec{x}} \cdot \left[\left(\vec{U} + \vec{c_g}\right) N\right] + \partial_t f \cdot \nabla_f N + \partial_t \theta \cdot \nabla_\theta N = \sum_i S_i. \tag{2.54}$$

2.3 Simulating FPV movement

Simulating the movement of FPVs on the water surface can be done based on time series of sea-state variables or wave spectra. Due to the random nature of waves, simulating a realistic sea surface is performed by sampling a wave spectrum for a given sea-state. This thesis uses the Joint North-Sea Wave Project (JONSWAP) spectrum, which is an expansion on the modified Pierson-Moskowitz spectrum given by

$$E_{PM}(\omega) = \frac{5}{16} H_s^2 \left(\frac{2\pi}{T_p}\right)^4 \omega^{-5} e^{-\frac{5}{4}\left(\frac{T_p \omega}{2\pi}\right)^{-4}}, \tag{2.55}$$

where T_p is the period of the waves with the highest energy, known as the peak period, and the rest of the variables are defined in the derivation of the action balance equation in section 2.2.4. The JONSWAP spectrum can then be expressed as a function of E_{PM}

$$E_J(\omega) = \alpha_\gamma S_{PM}(\omega) \gamma^{\exp\left(-\frac{(\omega - 2\pi/T_p)^2 2\pi^2}{\varsigma^2 T_p^2}\right)}, \tag{2.56}$$

where α_γ is a normalising factor, γ is the peak enhancement factor or skewness of the spectrum, and ς is the spectrum width parameter given by

$$\varsigma = \begin{cases} \varsigma_a, & \text{if } \omega \leq 2\pi/T_p \\ \varsigma_b, & \text{if } \omega > 2\pi/T_p. \end{cases} \tag{2.57}$$

The parameters ς_a and ς_b are empirical values, their most common values are $\varsigma_a = 0.07$ and $\varsigma_b = 0.09$. With $\varsigma_a = 0.07$ and $\varsigma_b = 0.09$, the normalising factor becomes $\alpha_\gamma = 1 - 0.287 \ln(\gamma)$, and as such the JONSWAP spectrum can be determined by the three sea state variables H_s, T_p and γ. Setting the peak enhancement factor $\gamma = 1$ gives $E_{J,\gamma=1} = E_{PM}$. Both (2.55) and (2.56) are presented as one dimensional spectra whose relation to the 2D-wave spectrum is given by (2.49). The $\mathcal{N}$ wave components used to simulate the water surface elevation $\eta(\vec{x}, t)$ of a given wave spectrum can be sampled from the wave spectrum as

$$\eta(\vec{x}, t) = \sum_{i=1}^{\mathcal{N}} \sqrt{2E(\omega_i)\Delta\omega}\, e^{i(\vec{k}_i \cdot \vec{x} - \omega_i t)} \tag{2.58}$$

where $\mathcal{N}$ frequencies are sampled with a frequency resolution of $\Delta\omega$. The wavenumber $\vec{k}_i$ for a frequency ω_i is found through the dispersion relation (2.27). If the wavenumber is two-dimensional it can include an offset in direction which allows for the directional spreading of waves. The amplitude $\sqrt{2E(\omega_i)\Delta\omega}$ in (2.58) is found through (2.43), (2.41) and (2.33).

The movement of the FPV system can be determined from the sampled wave spectrum. However, there is no apparent consensus on how to calculate the modules movements when the FPV systems interact with incoming waves. A complete hydrodynamic simulation of an FPV system interacting with a sea surface generated by (2.58) is beyond the scope of this thesis. In this thesis, I follow the assumptions from [35] which are summarised as:

- the floats are rigid bodies.
- the floats do not affect the propagation of waves.

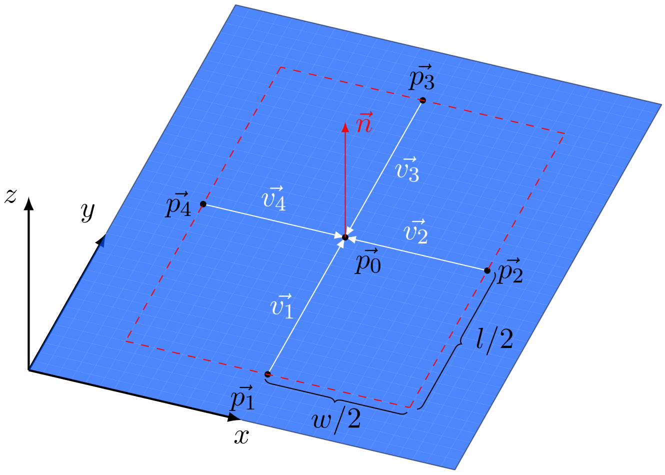

Figure 2.12: Initial conditions when simulating a sea surface with the WFM assumptions. The the cross products of the vectors formed between the points $\vec{p_i}, i = 1, 2, 3, 4$, and $\vec{p_0}$ define the resulting surface normal $\vec{n}$ of the module as described by (2.60).

- the floats follow the local wave motions exactly.
- the floats are not displaced in the horizontal plane.

As a result the floats with the modules are treated as weightless. I refer to this set of assumptions as the wave-following module (WFM) assumptions. The in-house simulation tool 3DFloat [34], developed at IFE, is used to simulate the sea surface based on (2.58). The input parameters used in this thesis for the 3DFloat software are H_s, T_p, γ, the directional spread of the waves, Sprd, and their mean incoming direction, Dir, defined as the angle east of north. A wave with incoming direction Dir $= 0°$ would then be entering the simulated area from the north, as by a nautical convention. Within 3DFloat, a floating module is represented as five points on a rectangle of width w and length l as shown in Figure 2.12. The five points are set in the middle of each side of the rectangle as well as in the centre of the rectangle. From the centre of the rectangle at $\vec{p_0} = (0, 0)$ the four points are placed at $\vec{p_1} = (l/2, 0)$, $\vec{p_2} = (0, w/2)$, $\vec{p_3} = (-l/2, 0)$, and $\vec{p_4} = (0, -w/2)$. During the simulation, only the five mentioned points of each simulated module are recorded. Through the points $\vec{p_i}, i = 0, 1, 2, 3, 4$, the surface normal of the respective module $\vec{n}$ is found as

$$\vec{n} = \frac{1}{4}\sum_{i}^{4} \vec{v_i} \times \vec{v}_{i+1}, \tag{2.59}$$

where the vectors $\vec{v_i}$ are the vectors between a side point $p_i, i = 1, 2, 3, 4$, to the centre point p_0 and $\vec{v_5} = \vec{v_1}$. It is also possible to find the surface normal of the modules by taking the cross product of the vectors between each opposing point as

$$\vec{n} = (\vec{p_1} - \vec{p_3}) \times (\vec{p_2} - \vec{p_4})\,. \tag{2.60}$$

The choice of (2.59) is to account for the possibility of non-representative events during the simulation. The POA irradiance on each module is found through their surface normals to assess their performance. A resulting normal on a sea with waves can be seen in Figure 2.13. As per the WFM assumptions, the five points $\vec{p_i}, i = 0, 1, 2, 3, 4$ follow the sea surface elevation but are fixed at a position on the horizontal plane. As a result, the distances $w/2$ and $l/2$ between the points are not maintained, and the simulated module will not have yaw. Additionally, the WFM assumptions ignores the moment of inertia that a physical float would have which potentially increases the range of the WFM simulated surface normal movement with respect to a real float.

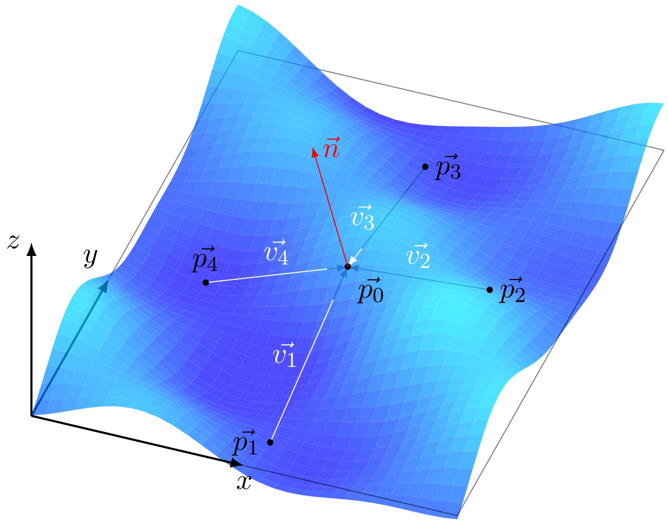

Figure 2.13: Resulting surface normal based on the WFM assumptions and (2.60) under wavy conditions. The distances between the points $\vec{p_i}, i = 0, 1, 2, 3, 4$ are constant in the xy-plane as in Figure 2.12. However, the distances between the points in three-dimensional space are not conserved.

2.4 Computational pipeline

I present the computational pipeline created for the calculation of the WIL, WIML and WIIL. A simplified outline of the pipeline can be seen in Figure 2.14. Each overarching step in Figure 2.14 is delimited by a dashed rectangle which corresponds to the main functions, written in the lower left corner of each rectangle.

A short overview of each overarching step from Figure 2.14 is presented below. The first overarching step in the pipeline is to perform a hindcast over the period of interest using a third generation wave model[7]. For hindcasts, wave models require at a minimum the bathymetry of the computational area (the depth data) and the wind fields during the period of interest. The pipeline assumes that wave spectrum time-series data at the boundaries of the computational area are available. If no wave spectra data is available, a nested run is recommended where the boundary wave spectra data is found from a larger simulation. From the output wave spectrum of the wave model, the necessary sea state variables are extracted to simulate the movement of the FPV system on the varying sea-states. The sea-state variables are passed into the second overarching step, where FPV system movements are simulated following the WFM assumptions. The FPV system movements are passed on to the third and last overarching step, where the system energy yield is computed based on the irradiance conditions at the chosen location for the same time period. With the module movements, the power production of the FPV system is found in the presence of waves, both for the entire system and

---

[7] To perform forecasts, more models would be needed to model the wind fields and possibly other atmospheric processes.

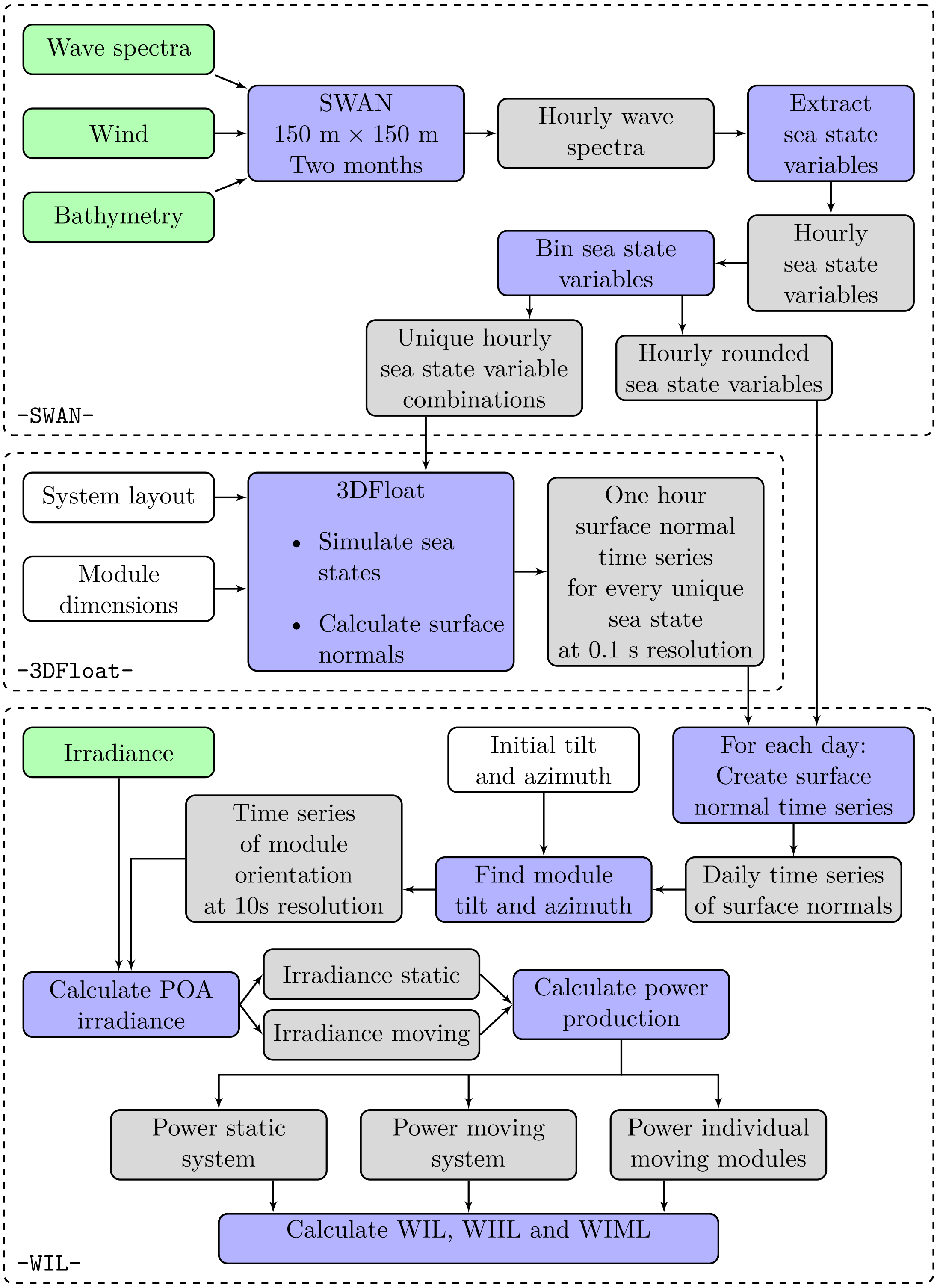

Figure 2.14: Outline of the pipeline used in this thesis. The green boxes represent external data needed to run the pipeline. The gray boxes represent data used and created within the pipeline. The blue boxes represent a process performed using the corresponding input data, such as performing the sea state modelling with SWAN or finding the POA irradiance ont he modules. The dotted boxes encompass the handling of three main functions `-SWAN-`, `-3DFloat-`, and `-WIL-` which define the pipeline processes.

the individual modules, and in the absence of waves. The WIL, WIIL and WIMLW are found with the recorded production data.

I now present the datasets, FPV system specifications and pipeline as used in this thesis. The pipeline is entirely written in the Python programming language apart from the already established SWAN and 3DFloat models which are written in the Fortran programming language. The datasets used in this thesis are presented in section 2.4.1. Three notable Python packages employed in the pipeline are presented in section 2.4.2. The three chosen locations, module parameters, and FPV system layout used in this thesis are presented in section 2.4.3. In section 2.4.4, I elaborate on details I consider important in the three main steps of the pipeline defined by `-SWAN-`, `-3DFloat-`, and `-WIL-` in Figure 2.14.

2.4.1 Datasets

I present the external datasets used in this thesis to calculate the wave-induced loss on a hypothetical FPV system placed along the eastern Norwegian coast. This thesis uses the Norwegian Meteorological Institute's (MET) NORA3 dataset for wind and wave spectra input to SWAN, as well as bathymetry data from Kartverket.no. The irradiance data is provided by the Copernicus Atmospheric Monitoring Service (CAMS).

NORA3

The freely available Norwegian reanalysis dataset NORA3 [21], provided by MET, provides high-resolution hindcast of the Norwegian coast, the North Sea and the Barents Sea. NORA3 has a 3km horizontal resolution (along the latitudes) with a one-hour time step. Using data from the ERA5 dataset, provided by the ECMWF, as initial and boundary conditions, NORA3 downscales the resolution of ERA5 through modelling and on-site measurements. NORA3 provides both atmospheric and wave hindcasts from 1964 until today with a 3 to 4 month delay due to the computational demands and data availability from ERA5. The atmospheric hindcasts grant wind fields at 10m, 20m, 50m, 100m, 250m and 500m height above ground level. This thesis uses the wind speed and direction at 10m above ground level as recommended by the SWAN manual [3]. The wave hindcasts grant hourly wave spectra to be used as forcing terms at the boundaries of the computational grid when using SWAN. The waves pectra provided by NORA3 are found by use of the WAM wave model.

CAMS

The Copernicus Atmospheric Monitoring Service (CAMS) solar radiation time series [38, 41] is used as input irradiance conditions when calculating the FPV power production. CAMS grants the global horizontal irradiance (GHI), diffuse horizontal irradiance (DHI), and the direct normal irradiance (DNI)[8] from 2004 to two days ago. The GHI, DHI, and DNI are provided at a 1 minute time resolution. In the dataset, the irradiation data between two timestamps of 1 minute is constant and equal to the end datapoint, i.e. a datapoint at time $t_{1/2}$ between the t_1 and t_2 timestamps where $t_2 - t_1 = 1$ minute is given by the data at the t_2 timestamp. The spatial resolution of the CAMS dataset is not fixed: the point(s) of interest are interpolated based on geostationary satellite observations. The GHI, DHI, and DNI in CAMS have units Watt-hour per square meter Wh m^{-2}.

---

[8] In the CAMS dataset the direct normal irradiance is abbreviated to BNI.

Kartverket

The bathymetry dataset used as input to the SWAN wave model in this thesis is provided by Kartverket.no [27]. The dataset provides the depth data along the Norwegian coast with a 50m × 50m spatial resolution. The data is publicly available for most of the Norwegian coast, except for areas important for national security such as Svalbard. For areas outside of Norway, the general bathymetric chart of the oceans (GEBCO) [20] provides depth data from the world oceans at a 15 arc-second spatial resolution. A 15 arc-second spatial resolution at 58° latitude corresponds to approximately 500m resolution. The GEBCO dataset grants a global coverage and is freely available, therefore it is a good bathymetry dataset for nested wave model runs. The GEBCO dataset has a higher resolution than the ERA5 reanalysis dataset, granting the option to improve the spatial resolution of all ERA5 wave spectrum data by use of third generation wave models.

2.4.2 Python Packages

I present some specific python packages used in the computational pipeline. The `dnora` python package developed by MET facilitates the use of third generation wave models. The python packages `pvmismatch`, developed by SunPower, and `pvlib`, originally developed at Sandia National Laboratories, facilitate the calculation of the FPV power production and mismatch effects.

dnora

MET developed the `dnora` python package for dynamical downscaling of the NORA3 and ERA5 datasets by use of third-generation models. Per today (3rd June 2025), the `dnora` package can be set up to run the WW3 and SWAN wave models. The `dnora` package facilitates the use of the wave models by automatically creating the necessary input files for the wave models and executing the simulations. The handling of input files is particularly useful for the WW3 wave model as it requires several preprocessed input files to execute the modelling. When using `dnora`, one may use local datafiles or utilise the built-in functionality to dynamically fetch data from either NORA3, ERA5 and GEBCO. To dynamically fetch and adapt data from NORA3 or ERA5, the `dnora` package uses the MET developed `fimex` package. An example of how the `dnora` package has been used in this thesis, without local datasets, can be found in Appendix A.1. In essence, the functionality of the `dnora` package is used to prepare the bathymetry data for the geographical area of interest and define the spatial resolution of the grid. The specific points of interest to find the hourly wave spectra and the total time span of the simulation are then defined. Next, the wind forcing over the entire grid and the wave spectra at the boundaries are prepared through `dnora` and `fimex`. The wave model is the executed through `dnora`.

pvmismatch

The `pvmismatch` python package models PV systems from cell level to system level. In `pvmismatch`, solar cells are modelled using the double diode model as shown in (2.2) and Figure 2.3. When using `pvmismatch`, one can specify the orientation and irradiance of the individual modules. One can thus simulate FPV using the `pvmismatch` package by updating the orientation and finding the POA of each module for each time step. Additionally, one can change the irradiance and temperature individually on every cell or on module or array level. `pvmismatch` also allows specifying placement for bypass diodes, thus providing a flexible framework for solar PV energy yield modelling. `pvmismatch` finds the MPP through the stacking method described in section 2.1.3 for all cells and modules connected series and parallel. The `pvmismatch` package was developed by SunPower and is functional, but the package is no longer maintained[9].

pvlib

The `pvlib` python package was developed to provide a reliable framework for simulating photovoltaic systems. The package is per today maintained and frequently updated. The `pvlib` package models PV systems based on the single diode equation (2.1) as shown in Figure 2.2.

When setting up a PV system using `pvlib`, one sets up the system from arrays, not individual modules. In `pvlib`, all modules in an array have the same orientation which adds complexity when simulating FPV systems. To simulate FPV systems using `pvlib`, one has to model each float as a unique system and perform the mismatch calculations manually. Additionally, `pvlib` does not provide an easy-to-use interface to change orientation of a system. Despite the lack of functionality to simulate FPV systems, `pvlib` provides functionality that complements the `pvmismatch` package where the latter package is lacking. In the pipeline, `pvlib` is used to:

- handle the CAMS irradiance data, such as converting the units of CAMS to W/m^2 as used in `pvlib` and `pvmismatch`.
- calculate the POA on each module based on the GHI, DHI, and DNI from CAMS and the orientation of the modules.
- get the position of the sun based on the FPV system's geographical location.

2.4.3 FPV system specifics

I introduce the three chosen locations near Risør, Norway, where the FPV system movements and the energy yield aer calculated. Then the modules' electric specifications are presented as well as the FPV system layout. The data with which a short validation of the output module movements from 3DFloat is presented at the end of this section.

Location

In this thesis, I perform WIL calculations at three different yet geographically close locations on the Norwegian eastern coast. The wave modelling with SWAN is performed for a computational grid encompassing the town Risør and its surroundings, as seen in Figure 2.15. The computational grid is defined by the longitudinal domain $(9.1, 9.4)$ and latitudinal domain $(58.0, 58.8)$. The three locations are labelled BAR, RIS, and HAV located at $(58.738, 9.17)$, $(58.74, 9.25)$, and $(58.725, 9.28)$ respectively, as shown in Figure 2.15. The three locations BAR, RIS and HAV all have different exposure to incoming waves. The location HAV is exposed to waves from the Skagerrak strait from the north-east to south-west directions[10]. The locations BAR and RIS, are both placed in the fjord Nordfjorden which blocks and dampens incoming waves from Skagerrak. The RIS location is expected to receive more energetic waves than the BAR location.

---

[9] SunPower filed for bankruptcy August 5th 2024.

[10] The Skagerrak strait connects the North Sea and the Barents Sea

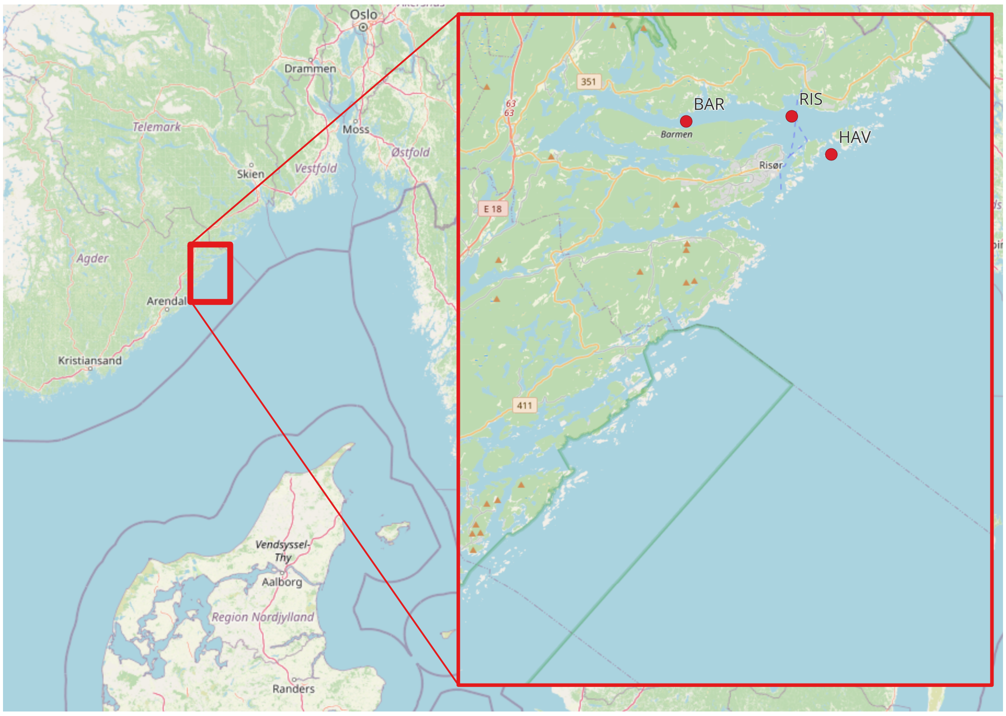

Figure 2.15: The computational area with the location of our three sites of interest placed on the south-eastern coast of Norway. The area delimited by the red rectangle is the area from which SWAN models the sea surface. The WIL calculations are performed at the three sites BAR, RIS, and HAV placed in Nordfjorden.

However, the wave coming from the Skagerrak strait may not be completely dampened by the skerries at the entrance of the fjord before reaching the RIS location. Therefore, the BAR location is expected to experience calm seas, the RIS location to experience calm to moderate seas and the HAV location to experience moderate to rough seas.

System layout and specifications

The parameters to model the solar panels are the same as those used by Nysted et al. [35]. The module parameters are based on a Cheetah 60M-V 325 W mono perc panel by Jinko Solar The electrical parameters can be found in Table 2.1. The electrical parameters were found through in-house measurements by Nysted et al.. The electrical parameters shown in Table 2.1 are used in the modelling, the parameters are supplemented with the default values provided by the `pvmismatch` package. The layout and size of a module can be found in Table 2.2. The modules are modelled with 60 series-connected cells which are divided into three substrings of 20 cells. A substring is a set of series-connected cells to which one bypass diode is connected in parallel. In the case of homogenous irradiance on all cells in a module at all times, the placement of bypass diodes in the circuit has no effect. However, it remains reasonable to model the module layout correctly. This thesis models $N = 10$ series-connected modules as an array and system. The initial position of the modules is as depicted in Figure 2.16, where the modules are placed along the x-axis with a distance $D = 125$ mm between each module. The modules are placed with the 1665 mm sides aligning with the west-east axis as can be seen in Figure 2.16. As shown in Figure 2.16, the system's y-axis is aligned with the north-south axis.

Table 2.1: Solar cell parameters used for the double diode model (2.2) in `pvmismatch`. The parameters are found in [35] and are extracted from a Cheetah 60M-V 325 W mono perc panel by Jinko Solar. The operating temperature of the cells in this thesis is kept constant. The I_{sc} is here short circuit current at the reference temperature. Default values from `pvmismatch` are used for the electrical parameters not mentioned in this table.

T (°C)	25
R_s (Ω)	0.0036
R_{sh} (Ω)	480.72

I_{01} (A)	3.9×10^{-11}
I_{02} (A)	1.1×10^{-6}
I_{sc} at 25°C (A)	10.12

Table 2.2: Module parameters as used in this thesis. All cells in a module are series-connected where the series is subdivided into substrings. Each substring has a bypass diode with a trigger voltage given by V_{bypass}.

Size (mm×mm)	Module	1665×1002
	Cell	158.75×158.75
Cells (count)	Per module	60
	Per substring	20
V_b (V)	-0.5	

Validation data

Data measured over 21 consecutive days at an FPV system deployed along the Norwegian coast is used to validate the simulated module movements by 3DFloat. Figure 2.17 shows a simplified layout of eight modules for which module movement data have been granted for this thesis. The eight modules in question are placed with an initial pitch of 5° and such that they move independently of each other. The time series of the pitch and roll of the eight modules are at a 0.1 s time resolution. For easier remembrance, the eight modules are named from east to west after the planets in the solar system, in order of increasing distance from the sun: Mercury, Venus, Earth, Mars, Jupiter, Saturn, Uranus, and Neptune. The sea-state data is recorded by a moored buoy placed outside of the mooring area, yet near the FPV system, a distance < 200 m east of the system.

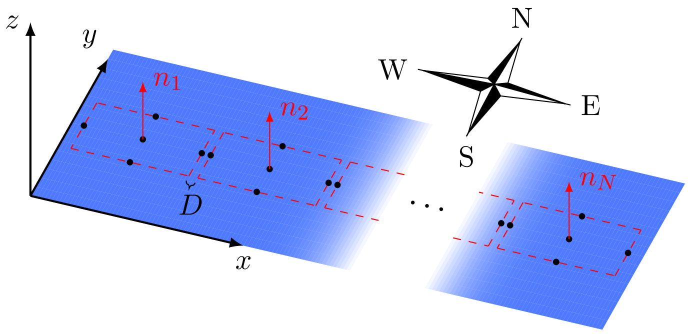

Figure 2.16: FPV system layout used for this thesis, where the relative sizes of the width and length of the modules and the distance between the modules are kept. A number N of modules are placed, with dimensions given in Table 2.2, along the x-axis. The distance between the modules is $D = 125$ mm. The system is placed such that the y-axis aligns with the north-south axis.

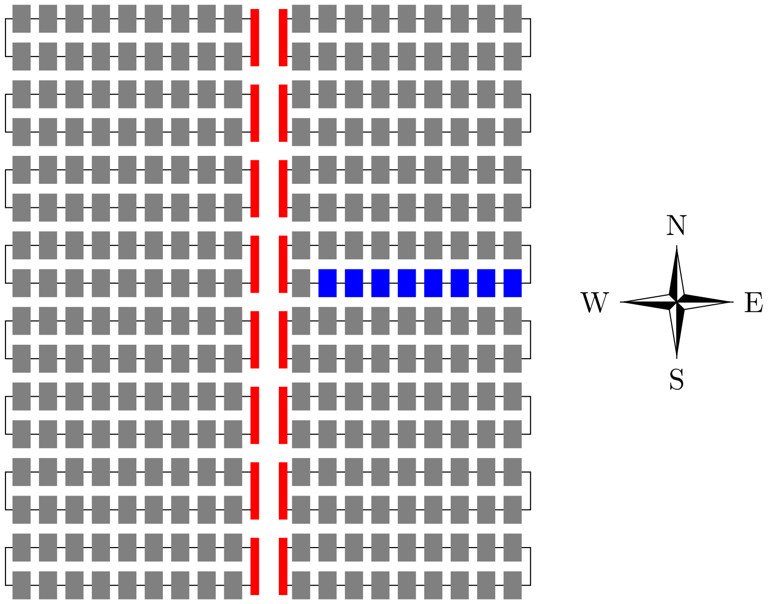

Figure 2.17: Simplified system layout of the deployed FPV system from which movement data for the eight modules in blue are granted for this thesis. Each rectangle represents a module of size 1134 mm × 1762 mm. The 8 blue modules are named from east to west: Mercury, Venus, Earth, Mars, Jupiter, Saturn, Uranus, and Neptune.

2.4.4 Pipeline details

I elaborate on details within Figure 2.14 and the code repository. The choice presented below can be altered for personal preference in the case of utilising the pipeline in different geographical contexts. The three main steps `-SWAN-`, `-3DFloat-`, and `-WIL-` are built such that they can be executed consecutively or separately.

`-SWAN-`

The `-SWAN-` function encompasses all steps taken with the SWAN wave model and its output before being used by 3DFloat. In `-SWAN-`, the SWAN wave model is run through the `dnora` python package with wind and wave spectrum data from NORA3 and bathymetry data from Kartverket, as depicted in the upper dashed rectangle in Figure 2.14. The `dnora` package can automatically fetch the necessary wind and wavespectra data from MET's data archive (https://thredds.met.no). However, acquiring the wind data through `dnora` for periods spanning more than a month is not recommended since the downloading process is time demanding and MET's data archive servers experience incidents on a near-daily basis (see their status page https://status.met.no). An incident occurring on MET's data archive servers while acquiring wind data from their archives interrupts the downloading process and thus necessitates a restart of the process. Therefore, the necessary wind data is downloaded locally before starting the process to reduce the risk of incidents on the MET data archive servers to interrupt the SWAN wave modelling. The NORA3 wind datasets are stored with one file for each month with an hourly time resolution. Each file covers the geographical area within $(44°, 83°)$ north and $(-30°, 85°)$ east with a 3km spatial resolution[11]. It is favourable to reduce the file size of the wind data from NORA3 to encompass only the necessary region defined by the

---

[11] The NORA3 wind datasets used in this thesis can be found at https://thredds.met.no/thredds/catalog/nora3_subset_atmos/atm_3hourly/catalog.html

geographic coordinates of the computational grid. A python script that performs the task of acquiring the wind data from MET's NORA3 dataset can be found in Appendix A.2. Acquiring the NORA3 wave spectra through the `dnora` package is not time demanding and therefore does not need to be downloaded locally. The bathymetry data from Kartverket is acquired from https://kartkatalog.geonorge.no with the name 'Dybdedata - terrengmodeller 50 meters grid' in XYZ format. The chosen spatial resolution when using SWAN with the 50m × 50m bathymetry data was 150m × 150m, a higher resolution led to unphysical solutions. The resulting bathymetry used in this thesis can be seen in Figure 2.18. The sea surface modelling with SWAN starts with homogenous initial conditions; the 20 first hours of the output wave spectra are omitted because of the ramp-up time needed for the SWAN model to produce representative results. The burn-in time was chosen based on early observations of the model output.

One wave spectrum describes the statistical properties of the water surface at the specified time stamp for the previous hour, i.e. between the current and previous time stamp. From the output wave spectra, the significant wave height H_s, peak period T_p, the peak enhancement factor γ, mean incoming wave direction Dir, and the directional spread of the spectrum Sprd are extracted and stored. The extracted variables are the input parameters to simulate the module movements with 3DFloat. Simulating the hourly sea-state for a complete year amounts to a maximum of $365 \text{ days} \cdot 24 \text{ hours} = 8760$ unique sea-states. Simulating one hour of FPV module movements with 3DFloat requires at least 15 seconds with 10 modules. Simulating a complete year amounts then to an expected runtime for 3DFloat of 36.5 hours. It is then favourable to reduce the maximum possible runtime of 3DFloat. An additional reason to reduce the total number of 3DFloat simulations are the storage space requirements: one simulated hour of the movement of 10 modules creates $\sim$ 33 Mb of data stored in text files ($\sim$ 3 Mb per module). Simulating 8760 see states would require a minimum of 290 Gb of available storage space, which I consider a large amount for regular portable computers. To reduce the amount of module movement simulations, the resolution of each variable is reduced to a set of values unique to that variable and exclude the sea states appearing during night hours. The chosen resolution for each variable is based on the impact the variable has on the WIL in clearsky conditions for June, the month of the summer solstice. The set of values for each variable are not required to be uniformly spaced, i. e. with a fixed step size, to adapt for ranges with high variability in the impact on the WIL. The analysis to find a suitable resolution for the sea state variables is performed in section 3.2. The sea state variables at each timestamp are rounded to the nearest value in their corresponding set and stored for further use by 3DFloat.

`-3DFloat-`

The `-3DFloat-` function simulates each unique hourly combination of the rounded sea state variables from SWAN. From these simulations, 3DFloat outputs the time evolution of the module surface normals for the respective hours as xyz-coordinates as well as the pitch and roll of the modules. This thesis models $N = 10$ series connected modules as a system. The layout presented in Figure 2.16 is equal for all simulations performed with 3DFloat for the BAR, RIS, and HAV locations. If the FPV system layout has a non-zero angle A_0 between the north-south and y axes, the mean incoming directions Dir of the simulated sea surface are rotated

$$\text{Dir}_{\text{mod}} = \text{Dir} - A_0 \tag{2.61}$$

to account for the shift in coordinates. The incoming direction $\mathrm{Dir}_{\mathrm{mod}}$, is then the incoming direction of the waves with respect to the y-axis of the FPV system layout. The rotation A_0 is corrected when calculating the azimuth in `-WIL-`.

The sea surface with all modules is simulated for one hour with a temporal resolution of 0.1 s. Each unique combination of sea state variables is simulated only once. The modules will have identical surface normals time series at each reoccurring unique sea state combination when computing the generated power by the modules. The surface normal time series found for a specific sea-state combination are assumed to be statistically representative for that combination and as such, reusing the simulations does not impact the WIL calculations.

Calculating the FPV energy yield - `-WIL-`

The `-WIL-` function performs the energy yield modelling of the FPV system based on its geographical location and simulated surface normals. To calculate the generated power by the modules, the rounded hourly sea-states variables are grouped by day. For each day, a dataset containing a concatenated time series for each module's surface normal is created with the respective tilt, azimuth, and sea state variables at each timestamp. Modules for a given system may be placed with a chosen initial pitch or roll, and a rotation A_0 of the y-axis from the north-south axis, as previously mentioned, to optimise energy production. To account for the initial orientation of the modules, the output normals from 3DFloat are rotated before calculating the tilt and azimuth of the modules. The pipeline only allows for a single initial rotation, either pitch or roll, as three-dimensional rotations are not commutative the order in which the rotations are performed would impact the result. An initial roll Θ_{Roll} corresponds to a rotation around the x-axis given by the rotation matrix

$$R_{\mathrm{Rolls}}(\Theta_{\mathrm{Roll}}) = \begin{pmatrix} 1 & 0 & 0 \\ 0 & \cos\Theta_{\mathrm{Roll}} & -\sin\Theta_{\mathrm{Roll}} \\ 0 & \sin\Theta_{\mathrm{Roll}} & \cos\Theta_{\mathrm{Roll}} \end{pmatrix}. \tag{2.62}$$

With $A_0 = 0$, a non-zero roll corresponds to a southward tilt. An initial pitch Θ_{Pitch} corresponds to a rotation around the y-axis given by the rotation matrix

$$R_{\mathrm{Pitch}}(\Theta_{\mathrm{Pitch}}) = \begin{pmatrix} \cos\Theta_{\mathrm{Pitch}} & 0 & \sin\Theta_{\mathrm{Pitch}} \\ 0 & 1 & 0 \\ -\sin\Theta_{\mathrm{Pitch}} & 0 & \cos\Theta_{\mathrm{Pitch}} \end{pmatrix}. \tag{2.63}$$

With $A_0 = 0$, a non-zero roll corresponds to a eastward tilt. In degrees, the tilt and azimuth time series of a module is calculated based on the time series of the x, y, and z coordinates of its surface normal with (2.9) and (2.10). The initial rotation from the north-south axis A_0 subtracted in (2.61) is added linearly to the calculated azimuth of the modules as

$$\mathrm{azimuth} = \varphi + A_0, \tag{2.64}$$

where φ is defined in (2.9).

In order of appearing sea-state combination for a day, the respective hourly module orientation data are concatenated into a time series for the respective day. When concatenating the time series of the module position, the hours that are outside the daylight hours of the respective day are excluded by use of `pvlib`. To reduce the computation time when calculating the system power output, the position data is resampled from 0.1 s to 10 s. A 10 s time resolution was found to be satisfactory by Nysted et.al.: the loss in accuracy was considered small while the computations were $\sim 100\times$ faster.

With the time series of the modules' movement, the power generation is found at every 10s time step for each day. At each 10 s time stamp, the POA irradiance on the system's modules is found for two cases:

1. In the presence of waves, i. e. based on the azimuth and tilt found from the 3DFloat simulations.
2. In the absence of waves, i. e. based on the initial azimuth and tilt of the modules.

The two distinct cases for the FPV system are refered to as the moving system, when in the presence of waves, and the static system, when waves are absent. For the moving system, the POA irradiance is found for each individual module. For the static system, the POA irradiance is found for one module as all modules have the same orientation in the absence of waves and hence, the same POA irradiance. The calculation of the POA irradiance is facilitated by `pvlib`, where I use the Perez diffuse irradiance model [36] to calculate the diffuse horizontal irradiance (DHI). The Perez model determines the diffuse irradiance through

$$E_d = \mathrm{DHI}\left((1-F_1)\,\frac{1+\cos(\Theta)}{2} + F_1\frac{\max\left[0,\alpha_i\right]}{\max\left[\cos(85^\circ),\cos(Z_{\mathrm{sun}})\right]} + F_2\sin(\Theta)\right), \quad (2.65)$$

where the coefficients F_1 and F_2 are empirical fits and described in detail in [36], DHI is provided by CAMS, and the tilt angle Θ is that of the module. The pipeline is constructed to use the CAMS reanalysis irradiance data with observed clouds, i. e. realistic irradiance data, or clearsky irradiance data from the `pvlib` package. Both datasets provide the DHI, DNI and GHI. The CAMS dataset has irradiance units $\mathrm{Wh/m^2}$ while `pvlib` and `pvmismatch` works with irradiance in the units $\mathrm{W/m^2}$: the CAMS data is therefore converted to fit the units of the pipeline[12]. In the pipeline, the CAMS dataset is downloaded automatically by use of the `cdsapi` python package unless a specific path to a CAMS datafile has been declared.

The power generated by the moving and static systems is found based on the calculated POA irradiance on their modules. The MPP of the two systems at each timestamp is found with the `pvmismatch` package. Additionally, the MPP of each module in the moving system is found as isolated systems based on their individual POA irradiance. The P_{mp} of the moving and static systems at their corresponding time stamp is stored as well as the individual P_{mp} for each module in the moving system. The generated power is stored separately for each day which is used to calculate the WIL, WIIL and WIML on desired time spans (year, month or day).

---

[12] The `pvlib` package, has built-in functionality to handle the unit conversion.

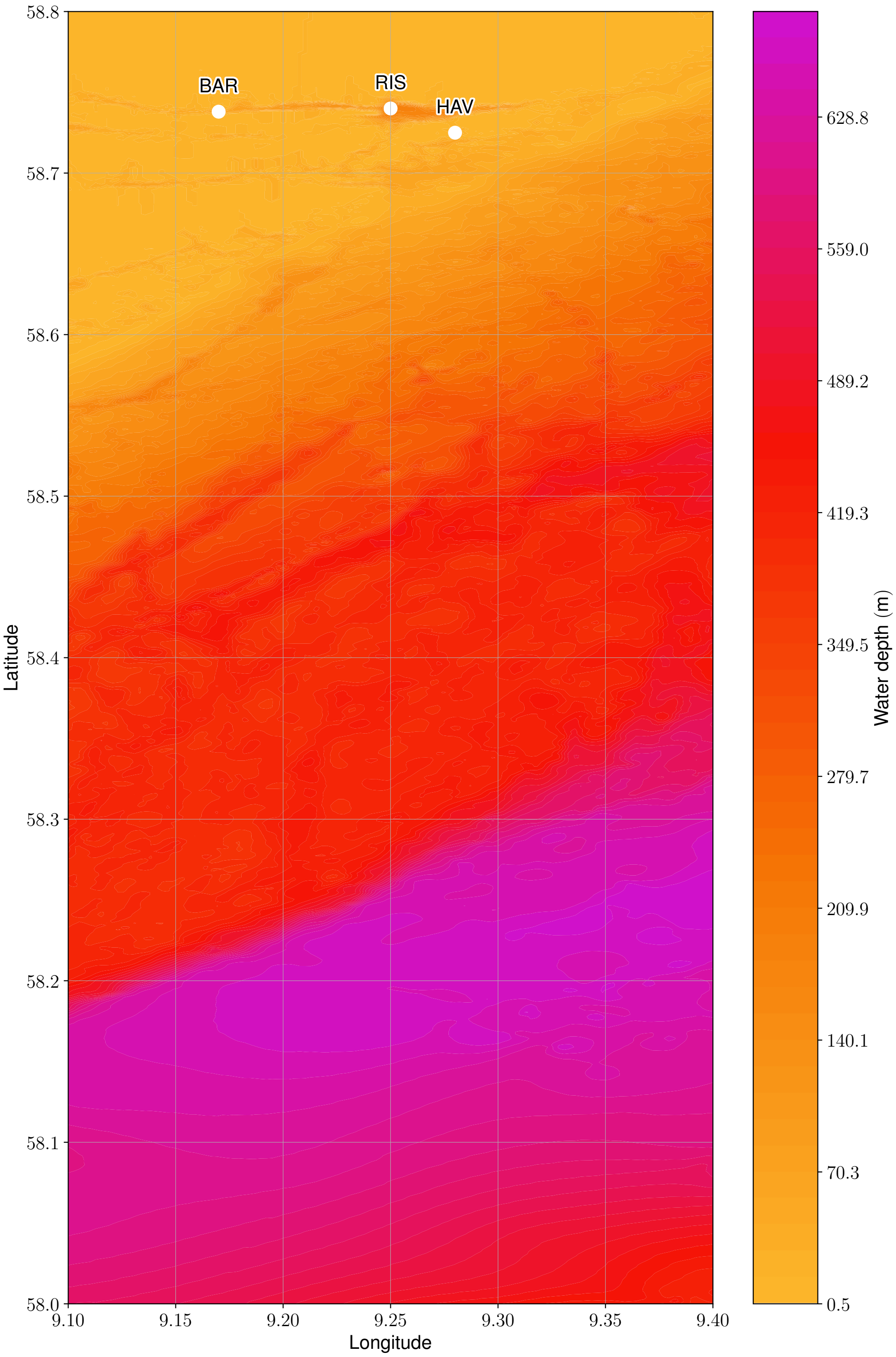

Figure 2.18: Bathymetry data used in the SWAN modelling. The sea-states are modelled at the BAR, RIS, and HAV sites.

Chapter 3

Results and discussions

I present and discuss the results of the thesis in three steps. First, in section 3.1, I perform a validation of the output 3DFloat module movement by comparing the output with measured float module movements from an existing FPV installation. In section 3.2, I perform a sensitivity scan on the WIL for the sea-state variables used when simulating the FPV system movements with 3DFloat. Based on the sea-state variable sensitivity scan I define the resolution of the sea-state variables to be used when performing the complete WIL computations at the locations BAR, RIS and HAV. In section 3.3, I present and discuss the energy yield at the three chosen locations for the full year 2023. How the energy production is affected by the sea-states and irradiance conditions is discussed on the time scales of a day, a month and a year.

3.1 3DFloat validation

The output module orientations from 3DFloat, found with the WFM assumptions, are validated with sea-state and module movement data recorded from an FPV system deployed along the Norwegian coast (see section 2.4.3).

The sea-state data, recorded by a moored buoy, show calm sea-states with significant wave heights below 0.12 m. The significant wave heights and peak periods, recorded in the 21 day period, are shown in Figure 3.1. The FPV system experiences exclusively calm sea-states during the recorded period. From Figure 3.1, the majority of the recorded significant wave heights are below 0.02 m, while the majority of the recorded peak periods are longer than 15 s. The influence of the recorded sea-states on the modules' orientation is expected to be small, which may limit the validation.

The mean incoming wave direction and mean directional spread of the waves recorded near the deployed FPV system are shown in Figure 3.2. The majority of the recorded wave directional spread are above 60°, which indicates that the FPV system will mostly experience long-crested waves. The majority of the incoming wave directions lie between north-west and south-east (clockwise).

From the data recorded by the buoy, 10 different sea-states are sampled with which the module movement with 3DFloat are simulated. The buoy data alternates between providing sea-state values hourly and with 30 minute time steps. Since 3DFloat is used for hourly sea-states in this thesis, the buoy data is downsampled to have a regular hourly time step. The downsampling is done by rounding up to every hour and exclude duplicate hours. To follow the approach applied in the pipeline, the hourly buoy data are rounded before sampling: H_s is rounded to two decimals, while T_p, Dir, and Sprd are rounded to zero decimals. The peak periods are rounded to zero decimals since the

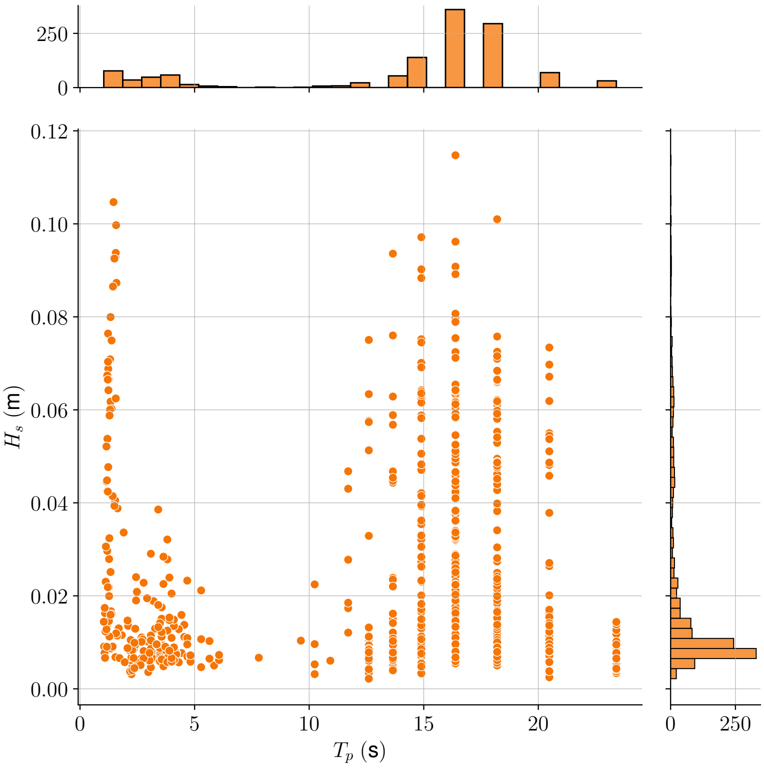

Figure 3.1: Measured H_s and T_p by a moored buoy near the BAR location. The data was recorded for 21 consecutive days. The data distribution of each variable is shown in the margin as histograms.

majority of the T_p measurements are already taken with zero-decimals, and variations with larger wave heights are more interesting than smaller T_p values, given the overall low significant wave heights. Before sampling the sea-states, time stamps where either the buoy or module orientation data are absent are excluded. From the rounded, hourly, buoy data 10 different sea-states are sampled with suitable random seed: I find a seed which selects sea-states with relatively high H_s with both long and short T_p. In Table 3.1, each sampled hour is given a case name to facilitate remembrance and comparison in the subsequent figures. The Sea21 case has $T_p = 1$ s, which cannot be simulated with 3DFloat. Therefore, the Sea21 case is set to have $T_p = 2$ s when simulating the module movements, which allows us to inspect the effect of excluding $T_p < 2$ s in the pipeline.

The module movements are simulated with 3DFloat, with the sea-states presented in Table 3.1. The module orientations in 3DFloat are found for eight modules placed with a distance of 378 mm between each other, and with a 5° initial eastward tilt. The module movement data from the deployed FPV system defined eastward tilt as positive pitch. The module size and placement during the simulation are as depicted by the blue rectangles in Figure 2.17.

The module movement at the site show a displacement from their initial orientation. Figure 3.3 shows the differences between the recorded and simulated modules' pitch and roll, for each sampled case. A first observation from Figure 3.3, is that the variations in the recorded module orientations appear displaced from the initial 5° pitch and 0° roll. These displacements can be seen in all sea-state cases and appear constant for each module across cases. For example: Mercury, Venus, Earth, and Neptune all vary around a pitch $> 5°$. These displacements from the initial orientation are attributed to

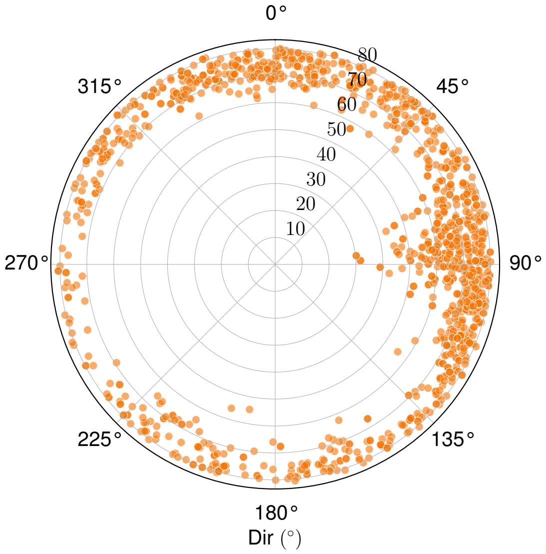

Figure 3.2: Measured Dir and Sprd by a moored buoy near the BAR location. The data was recorded for 21 consecutive days. The inner grid lines show the Sprd in degrees increasing radially.

mooring lines, wind, weight distribution on the floats, or other environmental factors. Since sample size is small, it remains uncertain whether the displacements are equal for all measurements of each module.

The recorded movement show signs of being influenced by external factors in the Sea23, Sea25, and Sea9 cases. In the Sea23 and Sea25 cases, larger than expected movements are observed compared to their similar sea-states in the Sea24 and Sea22 cases. These four cases all have $H_s = 0.02$ m with a $T_p \geq 16$ s and so the Sea25 case, which has the highest T_p among these cases, or the Sea23 case are not expected to show a larger range of movements. At the current time, I do not have any data that can explain this difference in behaviour. Another case where the recorded data appears affected by external factors is the Sea9 case. The simulated movement in the Sea9 case shows large variations in both the pitch and roll while the recorded movement shows large variations in the pitch but smaller variations in the roll. The smaller variations in the recorded roll

Table 3.1: The 10 sampled sea-states from the buoy measurements. Each case represents the sea-state for one hour. The Sea21 case is simulated with $T_p = 2$ s in 3DFloat, although the buoy measured $T_p = 1$ s.

Case name	H_s (m)	T_p (s)	Dir (°)	Sprd (°)
Sea1	0.01	2	88	50
Sea21	0.02	1 (2)	29	58
Sea22	0.02	16	23	76
Sea23	0.02	16	111	76
Sea24	0.02	16	238	69
Sea25	0.02	20	225	75
Sea3	0.03	16	284	76
Sea4	0.04	18	356	74
Sea8	0.08	18	10	72
Sea9	0.09	2	69	65

data are attributed to mooring lines limiting the float movements.

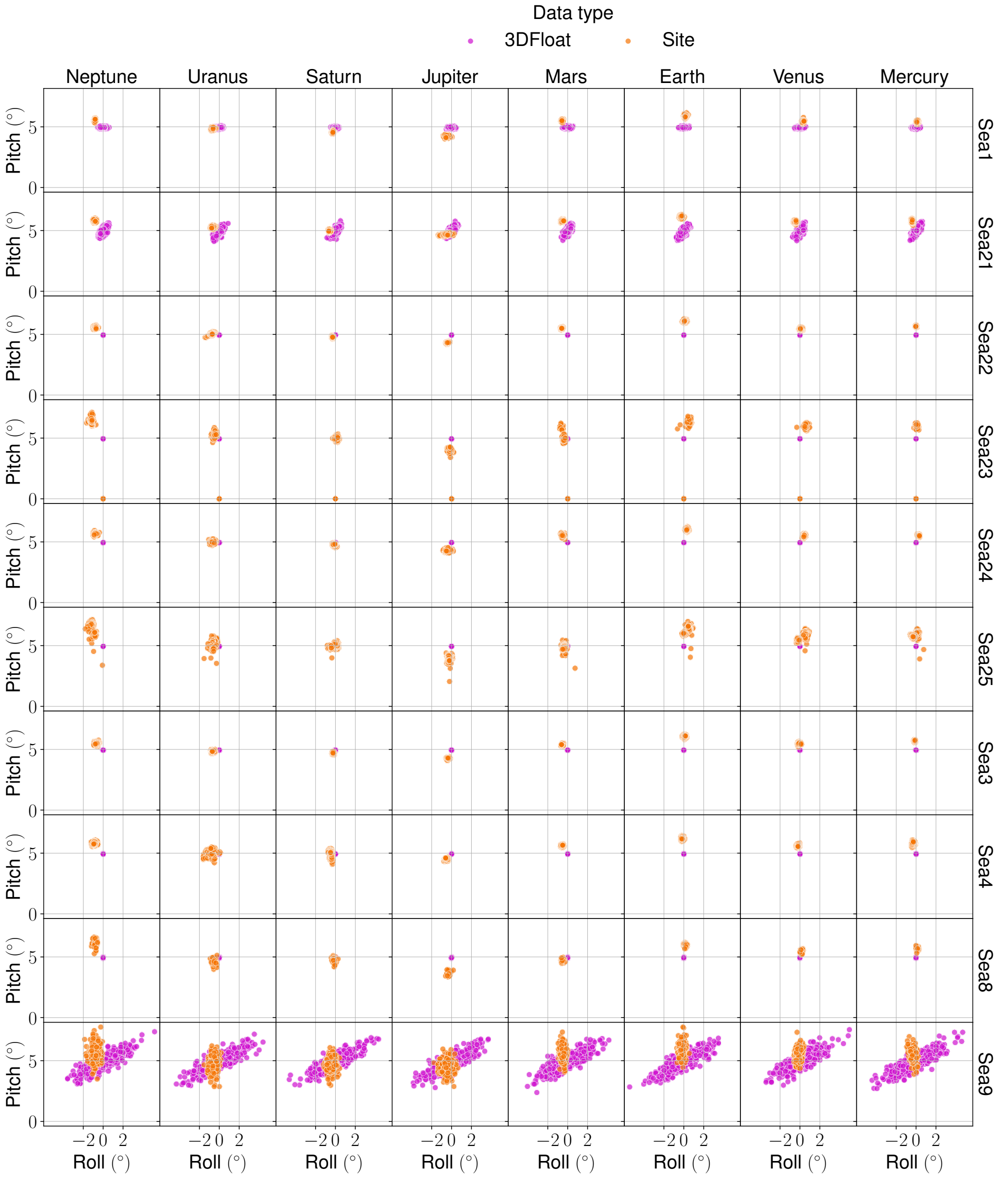

Figure 3.3: Measured and simulated module orientations. The measurements and simulations contain an equal amount of data points. The planet names are the module names, where Mercury is the module placed furthest east and Neptune is the module placed furthest west of the 8 modules. The corresponding sea-states to the instrument names can be found in Table 3.1.

The difference between the average pitch and roll of the simulated and recorded module movements can be seen in Figure 3.4. The difference is calculated, separately for the pitch and roll, as

$$\frac{1}{N}\left(\sum_{i}^{N}\Theta_{\text{simulated},i}-\sum_{i}^{N}\Theta_{\text{measured},i}\right), \tag{3.1}$$

where N is the number of samples, equal for both the simulated and measured data, and the subscript s and m indicate the simulated and measured data respectively. Data points where both pitch and roll are zero in the measured orientations, as can be seen in the Sea23 case, are excluded since those measurements are clear anomalies. Comparing the average orientation of the simulated module movements, with the recorded movements, does not provide meaningful insight on the 3DFloat simulations. However, the difference in the mean pitch and roll, between the simulated and recorded module movements, does not exceed 1.605° in absolute value, and varies around 0°. Therefore the average irradiance should remain approximately the same between an FPV system simulated by use of 3DFloat, and a deployed FPV system.

Despite being unable to account for external factors when simulating the module movement with 3DFloat, Figure 3.5 shows an agreement between the standard deviations of the simulated and measured pitch and roll data. The difference is calculated separately for the pitch and roll, as

$$\sqrt{\frac{1}{N}\sum_{j=1}^{N}\left(\Theta_{\mathrm{s},j}-\frac{1}{N}\left(\sum_{i=1}^{N}\Theta_{\mathrm{s},i}\right)\right)^2}-\sqrt{\frac{1}{N}\sum_{j=1}^{N}\left(\Theta_{\mathrm{m},j}-\frac{1}{N}\left(\sum_{i=1}^{N}\Theta_{\mathrm{m},i}\right)\right)^2}, \tag{3.2}$$

where the terms with the square roots are the standard deviations. With the exception of the roll in the Sea9 case, the differences in the standard deviations, between the simulated and measured pitch and roll, are less than 0.58° in absolute value. The small differences in the standard deviations indicate an agreement in the movement of the simulated module orientation, with the measured module orientation. The Sea21 case, where the sea surface is simulated with $T_p = 2$ s rather than $T_p = 1$ s, shows a difference in the standard deviations in the same scale as the Sea23 and Sea25 cases. For the Sea9 case, the large difference in the standard deviations of the roll was already observed in Figure 3.3.

The difference in the standard deviation for the pitch in the Sea9 case is expected from the WFM assumptions. The simulated module movement with the WFM assumptions does not consider the module or float weights, therefore the simulated movement must be expected to have larger variations than a real module. The Sea9 case, which has the largest H_s and shortest simulated T_p, shows a positive and large difference in the standard deviations. This large difference is an indication that the expectations from the WFM assumptions are correct: the WFM assumptions result in a larger range of movement than a real system.

Due to the low wave heights of the sea-states, the WFM assumptions cannot be completely validated. In Figure 3.3, the module movements are restricted by external factors, possibly by the mooring lines. These restrictions may increase the differences in the data distribution, as seen in Figure 3.5. However, as previously stated, the WFM assumptions are expected to yield a wider range in the module movements compared to a real system, since the float and module weights are omitted. This expectation is, to a limiting degree, confirmed in Figure 3.3 and Figure 3.5. The WFM assumptions must be explored further, preferably with rougher sea-states than those found in Figure 3.1. For the purpose of this thesis, the WFM assumptions are considered to yield good-enough module surface orientations, considering the simple setup needed to simulate the module movements.

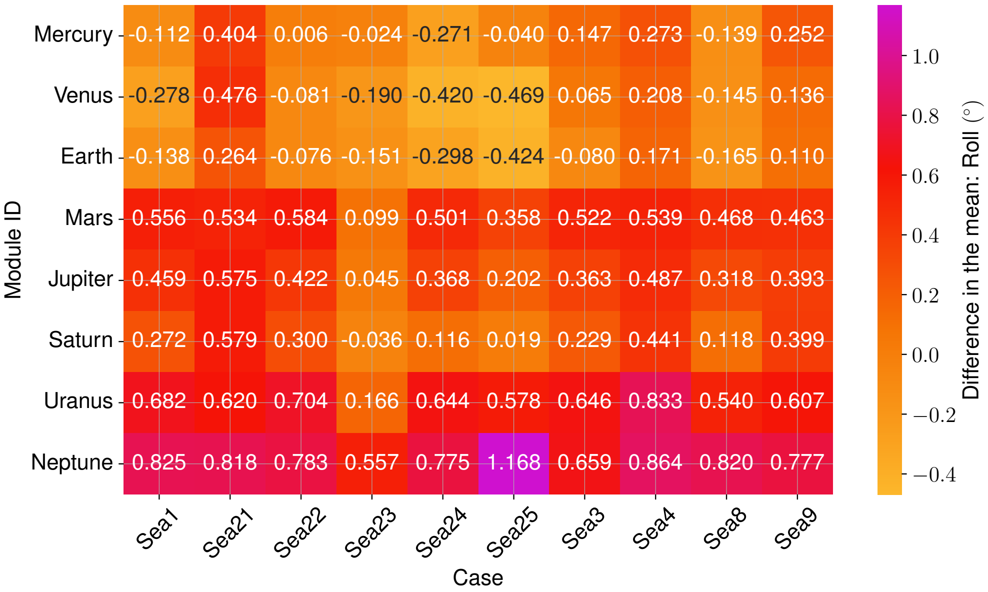

Module ID	Sea1	Sea21	Sea22	Sea23	Sea24	Sea25	Sea3	Sea4	Sea8	Sea9
Mercury	-0.112	0.404	0.006	-0.024	-0.271	-0.040	0.147	0.273	-0.139	0.252
Venus	-0.278	0.476	-0.081	-0.190	-0.420	-0.469	0.065	0.208	-0.145	0.136
Earth	-0.138	0.264	-0.076	-0.151	-0.298	-0.424	-0.080	0.171	-0.165	0.110
Mars	0.556	0.534	0.584	0.099	0.501	0.358	0.522	0.539	0.468	0.463
Jupiter	0.459	0.575	0.422	0.045	0.368	0.202	0.363	0.487	0.318	0.393
Saturn	0.272	0.579	0.300	-0.036	0.116	0.019	0.229	0.441	0.118	0.399
Uranus	0.682	0.620	0.704	0.166	0.644	0.578	0.646	0.833	0.540	0.607
Neptune	0.825	0.818	0.783	0.557	0.775	1.168	0.659	0.864	0.820	0.777

(a) Difference in the mean roll.

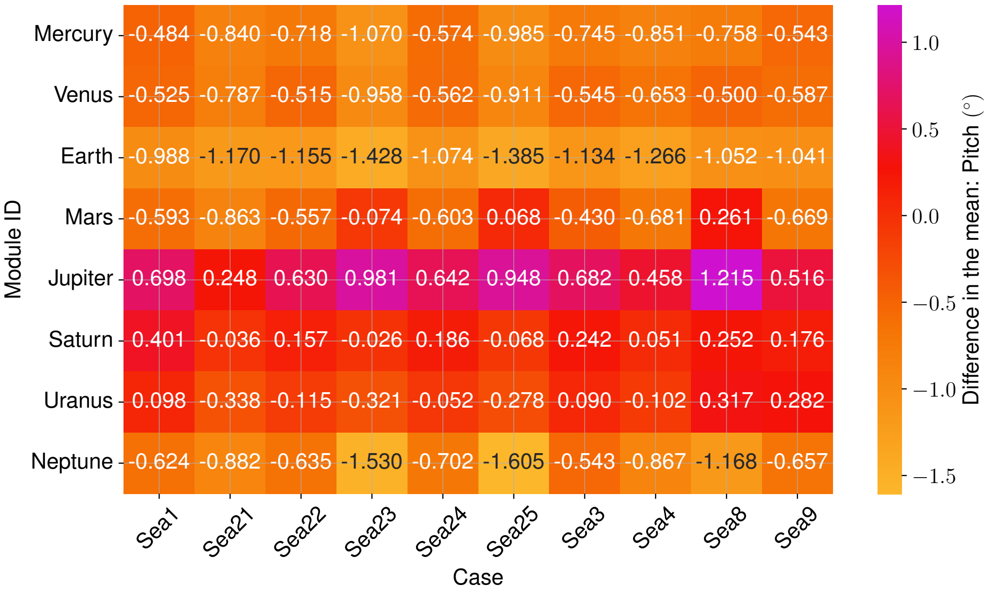

Module ID	Sea1	Sea21	Sea22	Sea23	Sea24	Sea25	Sea3	Sea4	Sea8	Sea9
Mercury	-0.484	-0.840	-0.718	-1.070	-0.574	-0.985	-0.745	-0.851	-0.758	-0.543
Venus	-0.525	-0.787	-0.515	-0.958	-0.562	-0.911	-0.545	-0.653	-0.500	-0.587
Earth	-0.988	-1.170	-1.155	-1.428	-1.074	-1.385	-1.134	-1.266	-1.052	-1.041
Mars	-0.593	-0.863	-0.557	-0.074	-0.603	0.068	-0.430	-0.681	0.261	-0.669
Jupiter	0.698	0.248	0.630	0.981	0.642	0.948	0.682	0.458	1.215	0.516
Saturn	0.401	-0.036	0.157	-0.026	0.186	-0.068	0.242	0.051	0.252	0.176
Uranus	0.098	-0.338	-0.115	-0.321	-0.052	-0.278	0.090	-0.102	0.317	0.282
Neptune	-0.624	-0.882	-0.635	-1.530	-0.702	-1.605	-0.543	-0.867	-1.168	-0.657

(b) Difference in the mean pitch.

Figure 3.4: Difference in the mean of the simulated and measured pitch and roll of the modules. The difference in the mean pitch and roll are shown in Figure 3.4b and Figure 3.4a, respectively. Positive values indicate a larger mean value in the simulated data. For example, in Figure 3.4a, the Sea25-Neptune case shows a larger mean roll in the measured data. The case names correspond to the sea-states found in Figure 3.1.

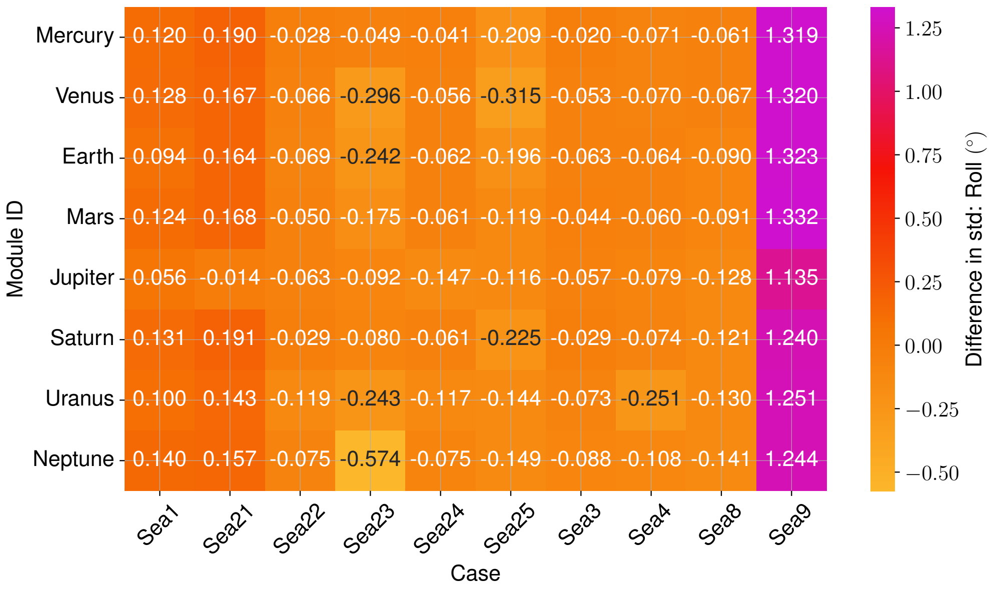

(a) Difference in the standard deviations of the roll.

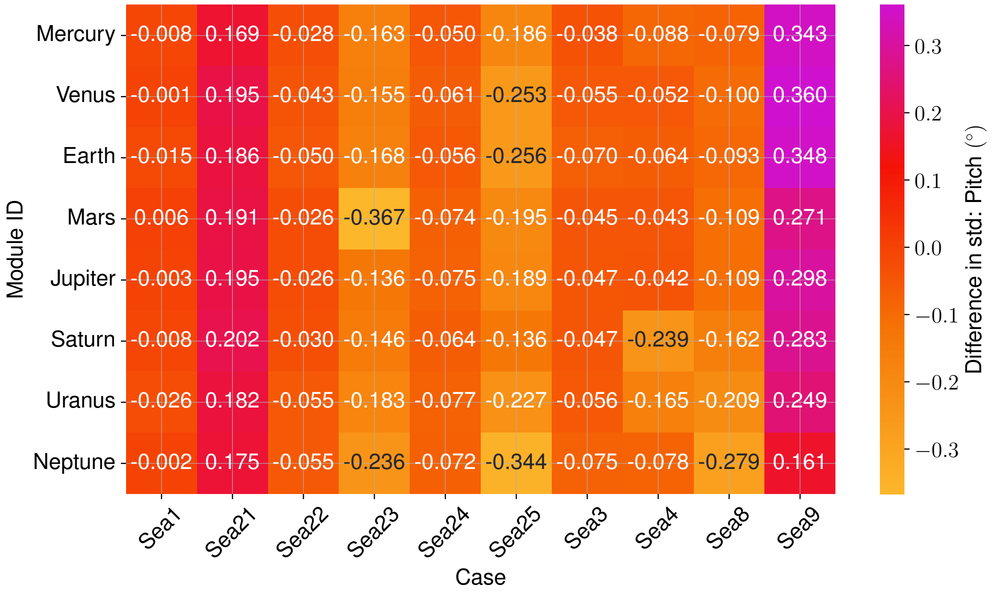

(b) Difference in the standard deviations of the pitch.

Figure 3.5: Difference in the standard deviations (std) of the simulated and measured pitch and roll of the modules. The difference in the standard deviation pitch and roll are shown in Figure 3.5b and Figure 3.5a, respectively. Positive values indicate a larger standard deviation in the simulated data. For example, in Figure 3.5a, the Sea25-Neptune case shows a larger smaller standard deviation in the roll of the measured data. The case names correspond to the sea-states found in Figure 3.1.

3.2 Sea-state variable sensitivity scan

I perform a limited sensitivity scan over the sea-state variables which are used as input to 3DFloat. The scan is performed to identify suitable sea-state variable resolutions that capture the effects on the WIL while reducing the maximum number of 3DFloat simulations. The variables are: the significant wave height H_s, peak period T_p, peak enhancement factor γ, the mean incoming direction of the waves Dir and the wave directional spread Sprd. The scan is performed on a system with no initial tilt and aligned on the x-axis as shown in Figure 2.16. For each sea-state, the energy yield of the FPV system is calculated for June 2023 at the RIS location (lat: 58.74, lon: 9.25) under clearsky conditions. The clearsky irradiance is fetched from `pvlib`. To scan over a sea-state variable, default values are set to all other variables and only the variable in question is altered between each simulation with 3DFloat. For example, to scan γ, H_s, T_p, Dir and Sprd are set to constant values and perform simulations with 3DFloat for altering values of γ. The energy yield is then calculated for each of those sea-states for June, one sea-state at a time.

3.2.1 Wave directional spread

First the wave directional spread is scanned with $H_s = 1$ m, $T_p = 6$ s, $\gamma = 1$ and incoming wave direction at 180° (from the south) and 90° (from the east). The scan can be seen in Figure 3.6, the scan is performed with a step size of 1° between 0° and 45° of wave directional spread and a step size of 10° for wave directional spreads larger than 45°.

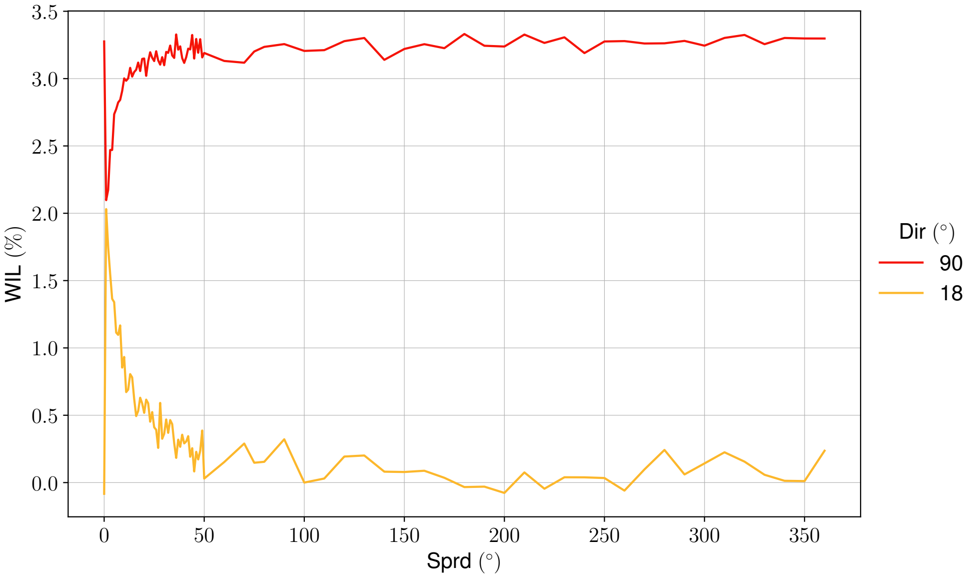

Figure 3.6: Impact of varying wave directional spread on the WIL for a constant sea state at (lat: 58.74, lon: 9.25) for June 2023. The constant sea-state variables are $H_s = 1$ m, $T_p = 6$ s, $\gamma = 1$ and, Dir$= 180°$ and Dir$= 90°$.

To qualitatively validate the implementation of the pipeline, I consider an intuitive case with two incoming wave directions, of 180° and 90°, and no directional spread. With an incoming wave direction of 180°, the waves are plane waves, i.e. pure sine waves, with the crest aligned along the system moving all module identically and simultaneously.

Therefore, Dir = 180° with Sprd = 0° must yield zero WIML which is observed in Figure 3.6. The negative WIL in the case with incoming wave direction of 180° is attributed to a negative WIIL: the system with no initial tilt received a higher total irradiance due to the wave motion compared to its static system. The FPV system is placed north of the equator and aligned with the local east-west axis. Therefore, a unison rotation of the system around the local east-west axis means all modules have the same POA irradiance at all times. With an incoming wave direction of 90° and 0° directional spread, the modules rotate around each of their local north-south axis in an asynchronous manner, which leads to an increase in mismatch effects as seen in Figure 3.6. Observing a sea surface consisting of plane waves propagating along the same direction is unlikely due to the waves naturally propagating from different sources and directions, therefore the wave directional spread of 0° is disregarded as a possibility in the modelling pipeline.

The impact of the wave directional spread on the WIL varies notably for Sprd$<$ 45°. From Figure 3.6, a 1° directional spread shows a similar impact of the WIL for the two incoming wave directions 90° and 180°, before the WIL diverges for increasing directional spread for the two distinct wave directions. The WIL increases from $\sim$ .2% to $\sim$ 3.5% with Dir = 90° and a directional spread from 1° to 45°, after which the WIL stabilises. For incoming wave direction of 180°, increasing the directional spread decreases the WIL from $\sim$ 2% to $\sim$ 0.1% where it stabilises after a 45° directional spread.

With low directional spread, the sea surface consists mainly of short-crested waves which creates a more irregular water surface compared to a sea surface consisting mainly of long-crested waves. Long-crested waves create a sea surface similar to the case of 0° in directional spread, where the waves appear to propagate in one single direction. Based on the observations on Figure 3.6, a high resolution is required for directional spread $<$ 50° and a lower resolution for directional spread $>$ 50°. Though the impact of the directional spread on the WIL is noticeable, the impact of all sea-state variables are considered before defining their resolutions. For the subsequent sea state variable scans, the directional spread is set to 75° to isolate the impact the directional spread may have on the WIL when varying the other sea state variables.

3.2.2 Peak enhancement factor

After analysing the effect of the wave directional spread on the WIL, the peak enhancement factor for the JONSWAP spectrum is scanned and can be seen in Figure 3.7. The constant variables are $H_s = 1$ m, $T_p = 6$ s, Sprd = 75° and with two incoming wave directions: Dir = 90° and Dir = 180°.

The peak enhancement factor has a small impact on the WIL with the chosen sea states. With an incoming wave direction of 180°, varying γ does not have any apparent impact on the WIL. With an incoming wave direction of 90°, increasing γ from 1 to 3 decreases the WIL from $\sim$ 3.1% to $\sim$ 2.4%. The decrease in the WIL for increasing γ with incoming wave direction 90° is small albeit noticeable. The peak enhancement factor is set to 1 for the subsequent sea-state variable sensitivity scans.

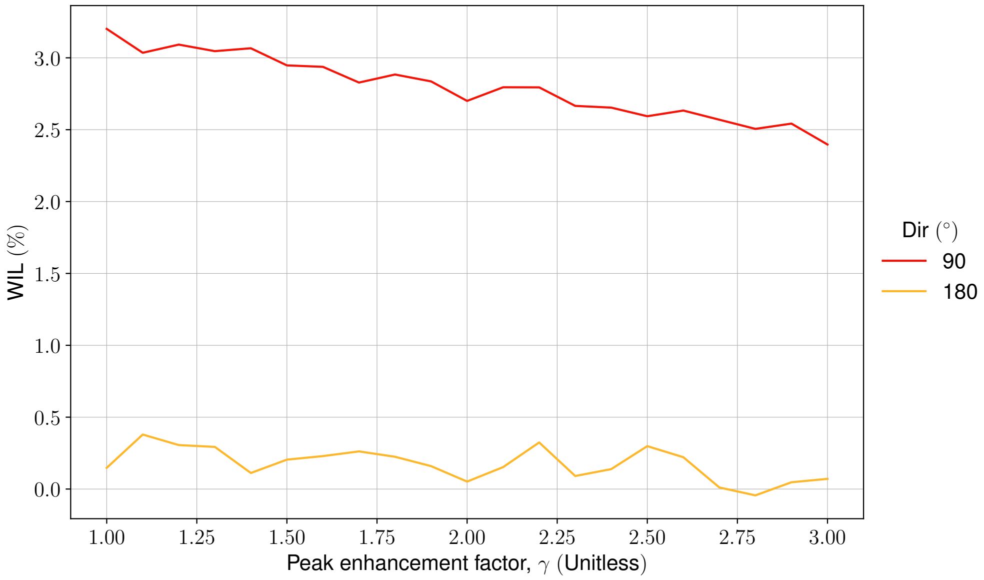

Figure 3.7: Impact of varying peak enhancement factor on the WIL for a constant sea state at (lat: 58.74, lon: 9.25) for June 2023. The constant sea-state variables were $H_s = 1$ m, $T_p = 6$ s, wave directional spread 75° and incoming wave direction was 180° and 90°.

3.2.3 Incoming wave direction

The impact of the incoming wave direction on the WIL, WIIL and WIML is shown in Figure 3.8, where the inner gray grid lines represent the energy loss in %. The constant sea state variables are $H_s = 1$ m, $T_p = 6$ s, $\gamma = 1$ and a 75° wave directional spread.

The WIML closely follows the WIL, while the WIIL varies around 0%. This indicates that the electrical loss, the WIML, has a stronger influence on the WIL than the optical loss, the WIIL. There are several instances with negative optical loss, i.e. an energy gain, indicating that, for a system with no initial tilt, the wave-induced movements increase the total incoming irradiance with respect to a static system. Placing the FPV system with an optimal initial tilt is expected to result in a positive WIIL, i.e. an energy loss. The incoming waves would move the modules away from their optimal orientation thus increasing the WIIL.

For the WIL and WIML, a symmetry around the north-south $(0° - 180°)$ and the east-west $(90° - 270°)$ axes is observed. Around the north-south axis, the WIL increases from $\sim 0.25\%$ to $\sim 3.25\%$ as the incoming direction shifts eastward/westward. It appears that each quadrant behaves similarly, however Figure 3.8 shows an aggregated value for the wave-induced losses which obscures variations on a daily scale.

Figure 3.9 shows that the symmetry observed in Figure 3.8 is a 180-degree rotational symmetry. Figure 3.9 shows how the daily power production, for June 1$^{\text{st}}$, of the moving and static systems is affected by different incoming wave directions. The power production of the moving system shows variations, due to the wave-induced module movements, near the continuous power production of the static system. The profile of the variations in the power production varies with the incoming wave directions: the time of day with the smallest variations in power production changes depending on different incoming wave directions. For instance, with Dir = 135°, the smallest variations occur between 13 h and 15 h, while the smallest variations occur between 8 h and 10 h for Dir = 45°. The time of day for these variations occurs with a 180-degree rotational symmetry for the incoming wave directions: the profile of the power production of the

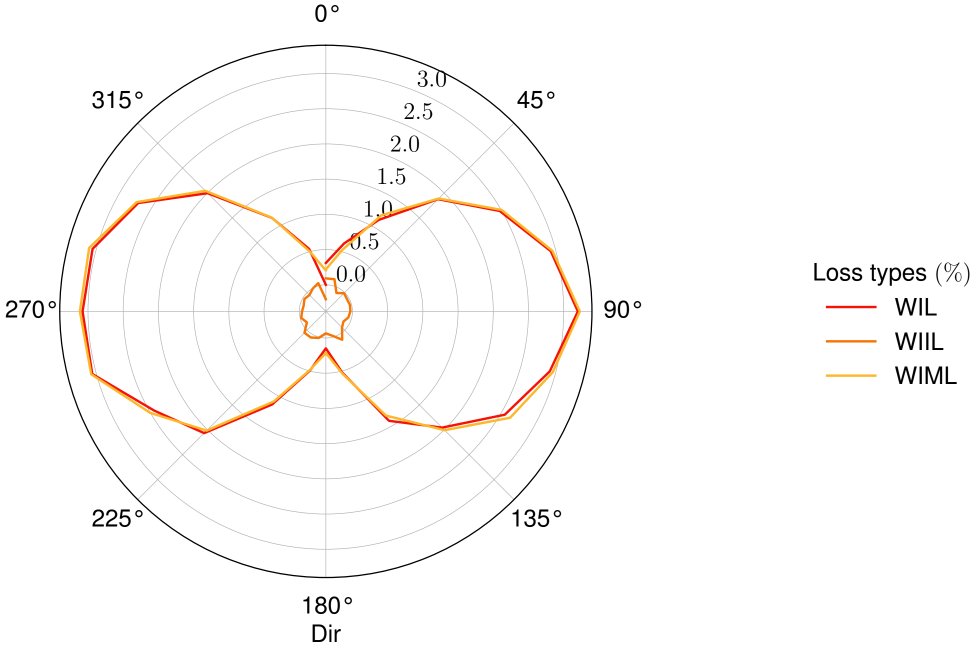

Figure 3.8: Impact of varying incoming wave direction on the WIL, WIIL and WIML for a constant sea state at (lat: 58.74, lon: 9.25) for June 2023. The constant sea-state variables were $H_s = 1$ m, $T_p = 6$ s, $\gamma = 1$ and wave directional spread was 75°.

moving system for Dir$= X°$ is the same at Dir$= X \pm 180°$, where X is any incoming direction.

The effect of the incoming wave direction on the WIL is dependent on the sun's azimuth with respect to the FPV system's location. As found in section 3.1, the distribution of the orientations of the modules calculated with 3DFloat is centred around the initial orientation. So the movements induced by an incoming wave direction and its 180-degree opposite are statistically identical. Therefore, at any point in time during a day with a clear sky, the variations in the power production of an FPV array must have the same range for the two 180-degree opposite incoming wave directions. To minimise the variations in the power production, i.e. the WIL, the position of the sun with respect to the FPV array must be such that the differences in the angles of incidence α_i are minimised. With (2.13), the relative difference in the upper and lower range of α_i is calculated for azimuths $\varphi_{\text{module}} \in \{0°, 45°, 90°, 135°\}$, and a tilt range $\Theta_{\text{module}} \in [-10°, 10°]$. The azimuths are chosen based on the incoming wave directions in Figure 3.9, while the tilt range is chosen as a reasonable tilt range. The relative differences in the range of α_i, for June 1st at the RIS location, can be found in Figure 3.10, where the relative difference at every point in time is calculated as

$$\frac{|\alpha_{i,\max} - \alpha_{i,\min}|}{|\alpha_{i,\max}|}. \tag{3.3}$$

With positive and negative tilt values and a fixed azimuth, the range of α_i corresponds to the relative ranges of angles of incidence for sea-states where Sprd $= 0°$ and Dir $= \{\varphi_{\text{module}}, \varphi_{\text{module}} + 180°\}$. From Figure 3.6, a sea-state with directional spread $\geq 45°$ yields a WIL similar to the same sea-state with Sprd $= 0°$. From Figure 3.10, the minima in the relative differences in α_i coincide with the time of the smallest variations in the power production of the moving systems, seen in Figure 3.9, for each symmetric pair of

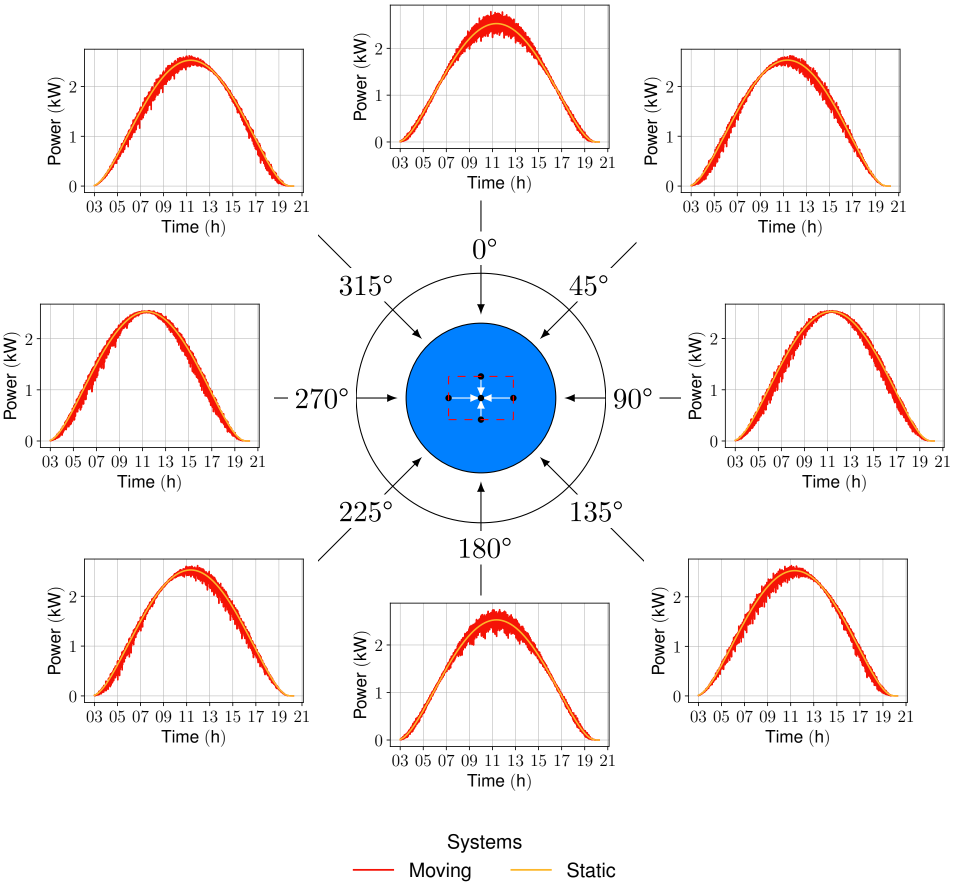

Figure 3.9: Daily power production of a moving and static FPV system for different incoming wave directions. The power production is for a 10-module array on June 1st at the RIS location. The placement of a module in the system with respect to the incoming wave directions can be seen in the innermost circle. The arrows and corresponding degrees indicate the incoming wave direction with their respective daily power production time series.

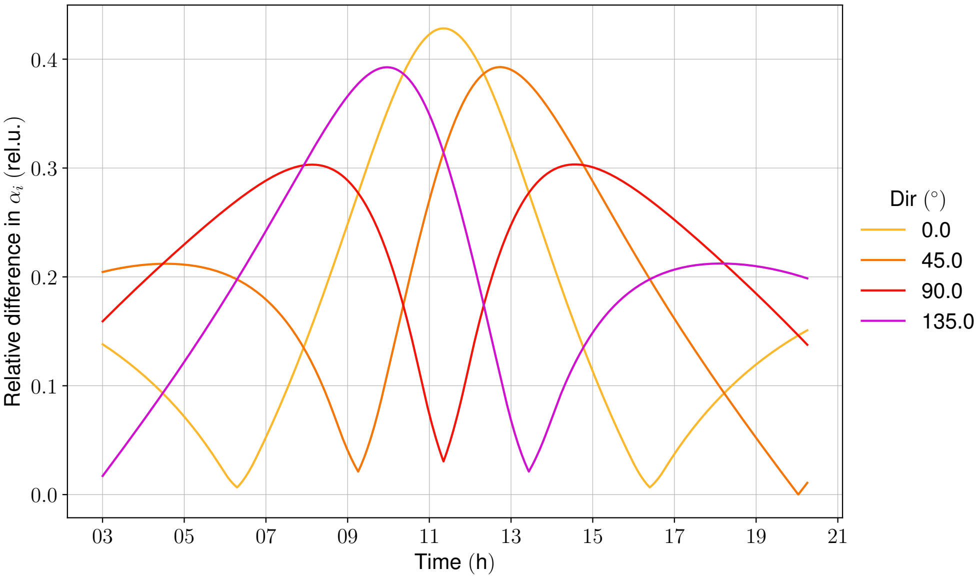

Figure 3.10: Relative size of the range in angles of incidence, α_i, for the moving FPV system for different incoming wave directions. The ranges are calculated through (2.13) with a module tilt range from −10° to 10° and module azimuth equal to the respective incoming wave direction. The angles of incidence are calculated for June 1st at the RIS location.

incoming wave directions. For example: the incoming wave directions Dir = 135° and Dir = 315°, have the smallest variations in the power production around 13 h in Figure 3.9, which corresponds with the minima of the curve for Dir = 135°.

For the subsequent sea-state variable scans Dir is set to 180°. By setting Dir= 180°, the impact of varying H_s and T_p on the WIL is shown as a deviation from $\sim 0\%$ wave-induced loss.

3.2.4 Significant wave height and peak period

The sensitivity scans for H_s and T_p are found in Figure 3.11 and Figure 3.12 respectively, where two different values for T_p (or H_s) are chosen when scanning H_s (or T_p). The sensitivity scan for T_p is performed with $H_s = \{0.25, 1\}$ m, while the sensitivity scan for H_s is performed with $T_p = \{3, 6\}$ s. The other sea-state variables are: $\gamma = 1$, Dir = 180°, and Sprd = 75°.

In Figure 3.11, the combinations of $H_s > 1$ m with $T_p = 3$ s are excluded because I do not expect to encounter such combinations at the chosen locations (see Figure 2.15). Additionally, from Stokes wave theory, the wave steepness is a limiting factor for the possible combinations of H_s and T_p. In deep water conditions, the wave steepness limit is [4, Chapter 5.2]

$$\frac{H_s 2\pi}{g T_p^2} = \frac{1}{7}, \tag{3.4}$$

which, for example, does not allow $H_s > 2$ m for $T_p = 3$ s. The SWAN wave model is expected to output realistic wave spectra which uphold the steepness limit. Similarly, the combinations $T_p < 3.5$ s with $H_s = 1$ m are excluded in Figure 3.12.

Shorter peak periods and larger significant wave heights greatly increase the WIL. Figure 3.11 shows a sharp increase in the WIL for $T_p = 3$ s and a slower increase for

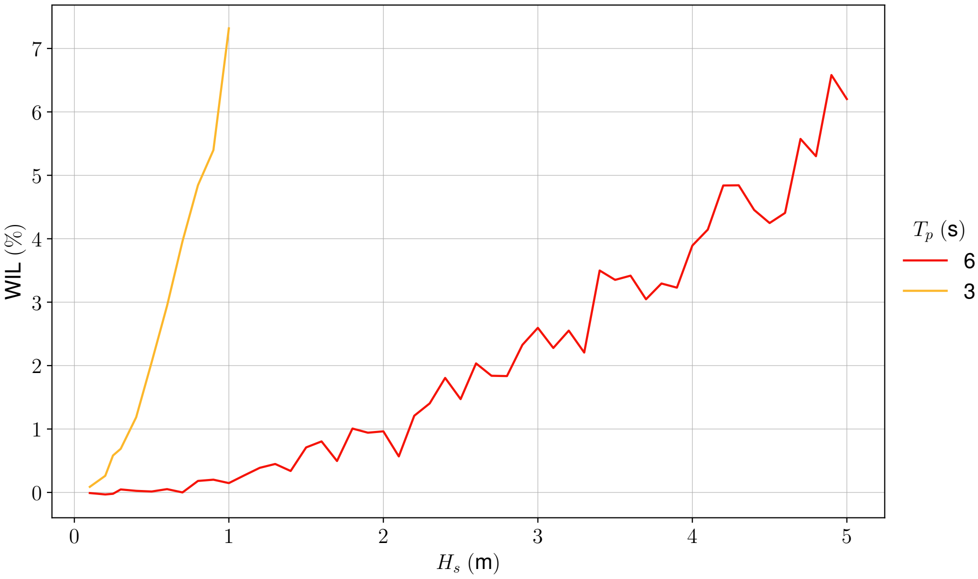

Figure 3.11: Impact of varying H_s on the WIL for a constant sea state at (lat: 58.74, lon: 9.25) for June 2023. The constant sea-state variables were wave directional spread at 75°, incoming wave direction was 180°, $\gamma = 1$, an T_p was set to 6 s and 3 s.

$T_p = 6$ s. Figure 3.12 shows a sharp increase in the WIL for both H_s cases, though the increase begins at different T_p values. Based on the sensitivity scans, H_s and T_p can greatly affect the WIL individually depending on the state of the other. For instance a long T_p would limit the impact on the WIL for lower H_s, while a low H_s limits the effect of shorter T_p. The combination of both variables determines the wave steepness which appears to be the most impactful sea-state parameter on the WIL. Both H_s and T_p have a significantly stronger impact on the WIL compared to γ, Dir and Sprd. The largest impact range in the WIL between γ, Dir and Sprd is attributed to the incoming wave direction with $\Delta\text{WIL} = \text{WIL}_{max} - \text{WIL}_{min} \approx 3\%$. Whereas $H_s = 1$ m and decreasing the peak period to $T_p = 3$ s has an impact range of $\Delta\text{WIL} \approx 7\%$. Large H_s values ar not expected in the BAR and RIS locations as they are not exposed to the open sea, however short T_p can be expected at all three locations.

3.2.5 Sea-state variable resolutions

I choose a suitable resolution for each sea-state variable, based on the observations in sections 3.2.1, 3.2.2, 3.2.3, and 3.2.4. The resolution of the significant wave height and peak period are defined first since they are the most impactful on the WIL.

A high resolution was chosen for low H_s and short T_p while a lower resolution was kept for higher H_s and longer T_p. Due to the surrounding skerries and islands, there should be a majority of low significant wave heights at the BAR and RIS locations. Therefore, it is reasonable to require a high resolution for low significant wave heights with a correspondingly good-enough resolution for the peak periods to correctly capture the WIL effects at all three locations. For the significant wave height a resolution of 0.05 m for $H_s \leq 1$ m was chosen while a resolution od 0.2 s for $T_p \leq 5$ s was chosen for the peak periods. For the larger values of H_s and T_p, the resolutions are reduced to 0.2 m for $H_s > 1$ m and 0.5 s for $T_p > 5$ s. For $T_p > 5$ s, it is unnecessary to have a high resolution in the significant wave height as the combinations of $H_s \leq 1$ and $T_p > 5$

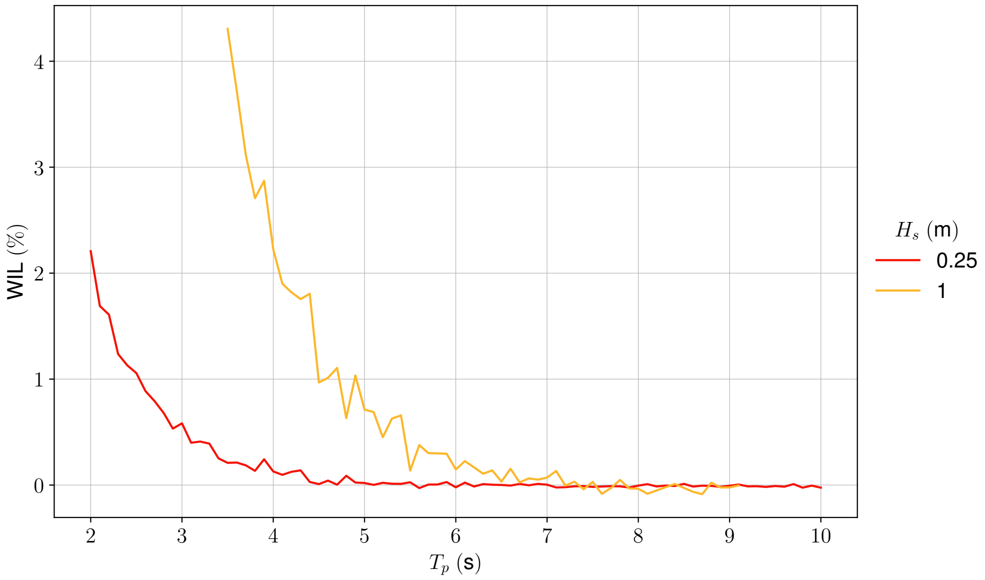

Figure 3.12: Impact of varying T_p on the WIL for a constant sea state at (lat: 58.74, lon: 9.25) for June 2023. The constant sea-state variables were wave directional spread at 75°, incoming wave direction was 180°, $\gamma = 1$, an H_s was set to 1 m and 0.25 m.

will have a small on the WIL. Therefore, the resolution in the significant wave height is reduced to 0.2 m for combinations of $T_p > 5$ s and $H_s \leq 1$ m. The resolution for the significant wave height can be described, in m, as

$$H_s \in \begin{cases} 0.00, 0.05, \dots, 1 \\ 1.20, 1.40, \dots, H_{s,\max} \\ 0.00, 0.20, \dots, H_{s,\max}, & \text{if } T_p > 5 \text{ m} \end{cases}, \tag{3.5}$$

where $H_{s,\max}$ is the highest recorded significant wave height for a location. While the resolution for the peak period can be described, in s, as

$$T_p \in \begin{cases} 2.0, 2.2, \dots, 5.0 \\ 5.5, 6.0, \dots, T_{p,\max} \end{cases}. \tag{3.6}$$

I allow for $H_s = 0$ m since the resolution is high: the significant wave heights extracted from SWAN are rounded to the nearest value in (3.5) meaning any value $H_s < 0.025$ m is rounded to $H_s = 0$ m.

The next most impactful parameter is the incoming wave direction. Due to the symmetries in Figure 3.8, a shift is applied for all values Dir> 180°. The resolution of 15° in step size for the incoming wave direction as used in Figure 3.8, is kept. The chosen resolution for the incoming wave direction is, in degrees,

$$\text{Dir} \in \{0, 15, \dots, 360\}, \tag{3.7}$$

where the values above Dir= 180° are folded as

$$\text{Dir} = \text{Dir} - 180, \text{ if Dir} > 180. \tag{3.8}$$

The wave directional spread requires a higher resolution for values < 45°, while the impact on the WIL stabilises for higher Sprd values as seen in Figure 3.6. To capture the effect of small directional spread and simultaneously reduce the total number of 3DFloat simulations, a resolution of 2° was chosen for Sprd $\leq 45°$ and a resolution of 45° was chosen for Sprd $> 45°$. The resulting resolution for the wave directional spread is expressed, in degrees, as

$$\text{Sprd} \in \begin{cases} 1, 3, \ldots, 45 \\ 90, 135, \ldots, 360 \end{cases} . \tag{3.9}$$

The least impactful sea-state variable on the WIL is the peak enhancement factor γ, based on our findings in section 3.2.2. Since the variations in γ cannot be neglected, a large step size of 2 was chosen starting at $\gamma = 1$. The chosen resolution for γ is expressed as

$$\gamma \in 1, 3, \ldots, \gamma_{\max}, \tag{3.10}$$

where $\gamma_{\max}$ is the largest peak enhancement recorded for a location.

The chosen resolutions are tentative. It may be the case that the chosen resolutions prove to be too coarse for a given location yielding non-representative results, or that the total number of simulations to perform is not reduced enough. The chosen resolutions should be adapted depending on the location and computational limitations.

3.3 FPV simulation results for 2023

I present the computational demand and the time gained from the increased resolution in the sea-state variables. I then compare the energy yield modelling for June 2023 at the three locations BAR, RIS and HAV.

3.3.1 Computational demand

All computations were performed on an Apple M3 chip with 11 cores, with the exception of the sea surface simulations which were performed on an 11th generation Intel i7 chip with eight cores.

The sea-state modelling using SWAN was performed for two-months at a time: January and February were together, then March and April, and so on. The modelling time was $\sim$ 7 hours per two-months period. The modelling was performed with MPI distribution on 10 cores to speed up the modelling time. Though the time demand for the SWAN modelling was considerable, it need only be performed once and it can extract wave spectra for multiple locations. I recommend including additional alternative locations for which to extract wave spectra in case a location is too close to the shore. A location close to shore may be placed on a tile that is considered on land when the bathymetry data is preprocessed to create the computational grid.

The chosen resolution in section 3.2.5 reduced the number of 3DFloat simulations. As can be seen in Table 3.2, the number of unique sea-state variable combinations has been reduced by more than 70% at each location. The reduction in time is considerable considering one sea-state takes at least 15 s to simulate. The low number of unique combinations for the BAR location is explained by its location: the area is less exposed to open waters and thus has less variations in sea-states.

The energy yield modelling of the FPV systems were also performed for two month at a time. The computations were distributed such that every two-month pair were computed on one core, i.e. I used six cores. Performing the energy yield calculations

Table 3.2: Number of unique sea-state combinations at each locations after applying the sea-state variable resolution chosen in section 3.2.5. The reduction in number of sea-states is with respect to the total possible number of unique sea-states: all 8760 hours within a year.

	BAR	RIS	HAV
Unique sea-state combinations (count)	1624	2006	2466
Reduction (%)	81.5	77.1	71.8

took a total of four hours for all two-month pairs. The maximum computational time was determined by the months with the longest days, i.e. the summer months. January and December took ~ 2 h to complete due to shorter days during winter.

3.3.2 Energy yield analysis

With the pipeline described in section 2.4, the difference in energy generation, between the BAR, RIS, and HAV locations, is found to be in the order of 10^1 kWh. The energy yield was calculated for an FPV system, described in section 2.4.3, with no initial tilt, for the year 2023. The resulting total energy production of the moving and static systems, as well as the sum of the energy produced by the individual modules in the moving system, can be found in Table 3.3.

Table 3.3: Energy yield of the moving and static systems for the year 2023 at the BAR, RIS and HAV locations. The sum of the energy produced by the individual modules in the moving system is included as $\sum_i E_i^f$. The systems are simulated with no initial tilt.

Location	E^f (MWh)	E^s (MWh)	$\sum_i E_i^f$ (MWh)
BAR	3.215	3.242	3.242
RIS	3.236	3.266	3.267
HAV	3.220	3.267	3.267

The difference in energy yield between the static systems, placed at the BAR, RIS, and HAV locations, is attributed to a difference in irradiance conditions. For the static systems, the largest difference in energy generated is between the HAV and BAR locations, at 25 kWh. Of the three locations, the RIS and HAV locations are the closest geographically, so those two locations are expected to have interchangeable irradiance conditions. This difference between BAR and the two other locations, is due to a difference in the irradiance provided by the CAMS dataset, where the irradiance for a location is found through interpolating the grid points nearest the location of interest. The BAR, RIS, and HAV locations appear far enough apart to yield different interpolation results from the CAMS dataset, though the RIS and HAV locations yield almost identical results.

The sum of the energy produced by the individual modules in the moving systems, is similar to the energy produced by their respective static systems. The values differ by ≤ 1 kWh. This similarity indicates, for a system with no initial tilt, that the total incoming irradiance does not change noticeably due to wave-induced movement. The modules of the moving system, on a yearly average, have the same orientation as the modules in the static system. This agrees with Figure 3.3, where the distribution of the simulated module movements are centred around the initial orientation.

Comparing energy lost by the moving and static systems, the energy lost in the moving system at the HAV location is almost twice as high as the largest difference in the energy generated by the static systems. At the BAR and RIS locations, this difference in energy lost is also larger than the largest difference in the energy generated by the static systems. Comparing the moving systems, the largest difference in energy yield is between the BAR and RIS locations, at 21 kWh. The moving system at the HAV location generated 16 kWh less than the moving system at the RIS location. Comparing energy generated by the moving systems with the energy generated by the static systems, the largest difference was between the RIS and BAR locations. The difference in energy generated between the moving and static systems at the HAV location was 46 kWh, while at the BAR and RIS locations the differences are 27 kWh and 30 kWh, respectively.

The resulting yearly WIML and WIIL at the three locations, found in Table 3.4, are in accordance with our observations in Table 3.3. In Table 3.4, the optical loss is negligible, below 0.03%, for all three locations. The low WIIL agrees with the small differences in energy produced by the static systems and the sum of the energy produced by the individual modules, in the moving system. However, the WIIL is negative for the BAR and RIS locations, indicating an incoming irradiance gain compared to a static system, with the largest gain at the BAR location. Comparatively, the lowest and largest WIML is found at the BAR and HAV locations respectively. The WIML is larger than its respective WIIL at each location, which agrees with the larger differences between the energy generated by the respective moving and static systems. Additionally, the order of increasing WIML is in accordance with the differences between the respective moving and static modules. Based on Table 3.4, as observed in Figure 3.8, the influence of the WIML on the WIL is larger than that of the WIIL. With the small differences between E^s and $\sum_i^N E_i^f$, the correction term in (2.19) is approximately one, yielding

$$\text{WIL} \approx \text{WIML} + \text{WIIL}. \tag{3.11}$$

Table 3.4: Wave-induced losses on the moving and static systems for the year 2023 at the BAR, RIS and HAV locations. The systems are simulated with no initial tilt.

Location	WIL (%)	WIML (%)	WIIL (%)
BAR	0.837	0.857	-0.020
RIS	0.945	0.955	-0.011
HAV	1.429	1.425	0.004

Table 3.5 shows large variations in the monthly and daily wave-induced losses. The variations are to be expected due to seasonal variations on the monthly scale and irradiance conditions on the daily scale. On a monthly scale, the standard deviations remain below their respective averages for the WIL and WIML in all locations. The monthly standard deviations in the WIL and WIML, being $\geq 68\%$ of their respective averages, point to significant seasonal dependencies for the wave-induced losses. On a daily scale, the standard deviations are up to 174% of the mean of the WIL, WIML, and WIIL. The large variations in the daily wave-induced losses indicates a strong influence of the combination of irradiance and sea-state conditions.

Monthly and daily yield comparison

The seasonal behaviour at the BAR, RIS, and HAV locations is similar, for the monthly WIIL, total possible energy production, WIL, and WIML of a 10-module FPV system with no initial tilt. Figure 3.13 shows that the profile of the monthly WIIL remains

Table 3.5: Monthly and daily mean with standard deviation for the WIL, WIML, and WIL at the BAR, RIS, and HAV locations. The systems are simulated with no initial tilt.

		BAR	RIS	HAV
WIL (%)	Monthly	1.42 ± 0.92	1.46 ± 0.99	2.32 ± 1.61
	Daily	1.16 ± 1.93	1.33 ± 1.60	2.12 ± 2.33
WIML (%)	Monthly	1.45 ± 0.94	1.47 ± 0.99	2.35 ± 1.66
	Daily	1.15 ± 2.01	1.28 ± 1.65	2.08 ± 2.46
WIIL (%)	Monthly	-0.03 ± 0.04	0.00 ± 0.03	-0.03 ± 0.08
	Daily	0.01 ± 0.17	0.04 ± 0.18	0.04 ± 0.33

approximately 0% throughout the year with a negative loss in November for all three locations, i.e. a gain with respect to a static system. The optical energy gain in the winter months can be explained by the sun's low zenith, though an optical gain should then also be expected in December, the month of the winter solstice. The wave-induced movement tilts the modules toward the sun where they generate more power than when the modules are static with a small angle of incidence with the sun. The profile of the WIIL, for each location, is in good agreement with Figure 3.5, where the average WIIL is negative.

The total possible energy production of the moving system, $\sum_i^N E_i^f$, appears identical for all three locations. Figure 3.13 shows a concave seasonal trend in $\sum_i^N E_i^f$, with a maximum of ~ 600 kWh in June which decreases toward the winter months of January and December. All three locations are geographically close to each other, which explains the similarity in $\sum_i^N E_i^f$ as a similarity in irradiance conditions. However, as noted in Figure 3.3, there is a difference of a few kWh in $\sum_i^N E_i^f$ between the three locations.

The monthly WIL and WIML also show a similar, and interdependent, behaviour across the different locations with seasonal variations. From Figure 3.13, the WIL and WIML appear inversely related to $\sum_i^N E_i^f$ and, by extension, to the energy generation of the system. During the winter months, the FPV system is exposed to less irradiance due to shorter days. The power generation during the winter months is low, which leads to larger relative differences between the energy generated by the moving and static systems as well as between the modules themselves. So a large WIL and WIML during the winter months represents a smaller effective loss compared to the smaller WIL and WIML during the summer months, when the FPV system generates significantly more energy. It can be noted that the pattern in the WIL, observed in Figure 3.13, is in accord with the observations of Nysted et al.: the WIL is smaller during the summer months.

There is a difference in the scale of the wave-induced losses, between the BAR, RIS, and HAV locations. The minimum WIL and WIML at the three locations is $\sim 0.5\%$, reached in July. The maximum WIL at the BAR, RIS, and HAV locations is $\sim 3\%$, $\sim 4\%$, and $\sim 6\%$, respectively, reached in December. The differences can be explained by the sea-states at the different locations in combinations with low power generation during the winter months.

During the transitional months (February and October), the wave-induced losses at the BAR location show different behaviour than at the RIS and HAV locations. The differences can be attributed to different sea surface conditions at the three locations. I explore these differences in more detail since only the BAR location shows a different profile.

To avoid a repetitive analysis, the three locations are compared for the month of October. The daily wave-induced losses, and the total possible energy production of the moving systems is presented in Figure 3.14. The energy production and wave-induced losses of February 2023 can be found in Appendix B.1.

In Figure 3.14, it is clear that the WIL at the BAR location deviates from the RIS and HAV locations. There are two distinct spikes, on October 4^{th} and 11^{th}, in the WIL at the BAR location. On October 11^{th}, both the RIS and HAV sites experience a similar behaviour in T_p, Dir, and Sprd with $\gamma = 1$ (found manually in the data) as can be seen in Figure 3.16 and Figure 3.17. On October 11^{th}, the main difference between the RIS and HAV locations lies in H_s, where they experience H_s up to 1.4 m and 0.75 m respectively. The power generation of the moving system varies around that of the static system, which reduces the total loss, with larger variations for larger wave heights. In Figure 3.15, the sea-states at the BAR location show an incoming wave direction that diverges from that seen at the RIS and HAV locations, in addition to shorter T_p and lower H_s. On October 11^{th} at the BAR location, the power generation of the moving system fluctuates around that of the static system At approximately 10 AM there is a dip in irradiance. After 10 AM, the power generation of the moving system fluctuates below that of the static system: the power generation of the moving system is limited due a constant mismatch. In Figure 3.15, the sea-state variables that change noticeably after 10 AM are T_p and Dir. The combination of a lower T_p and an unfavourable incoming wave direction creates the large difference in the daily WIL between BAR and the two other locations. The same differences can be found for October 4^{th}, in Appendix B.2. Additionally, there is a difference in irradiance conditions between the BAR and the two other locations in figures 3.15, 3.16, and 3.17: the dip in irradiance at 10 AM is differently shaped between the locations. The difference in irradiance is small, which corresponds to the differences in total energy production seen in Table 3.4.

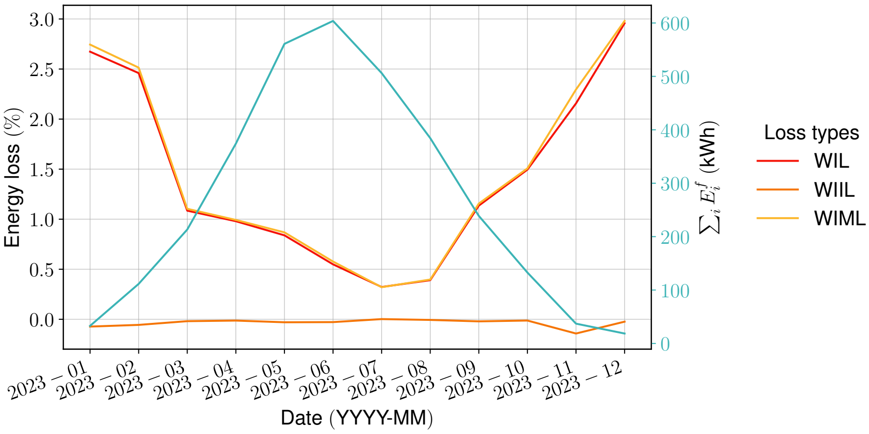

(a) Wave-induced losses at the BAR location, 2023.

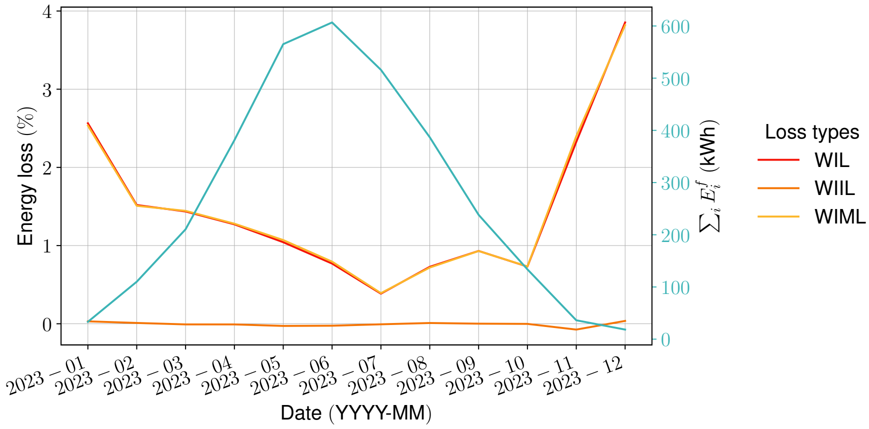

(b) Wave-induced losses at the RIS location, 2023.

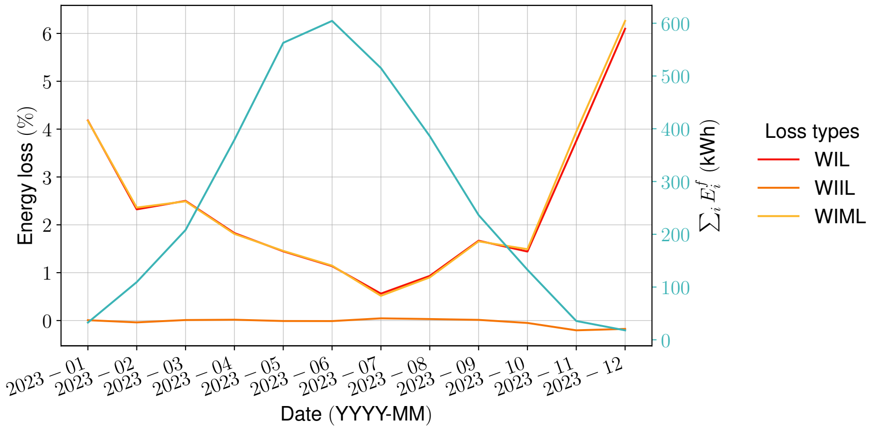

(c) Wave-induced losses at the HAV location, 2023.

Figure 3.13: WIL, WIIL, and WIML for 2023 at the BAR (3.13a), RIS (3.13b), and HAV (3.13c) locations. The cyan line corresponds to the right vertical axis and shows the sum of the energy produced by each individual module in the FPV system.

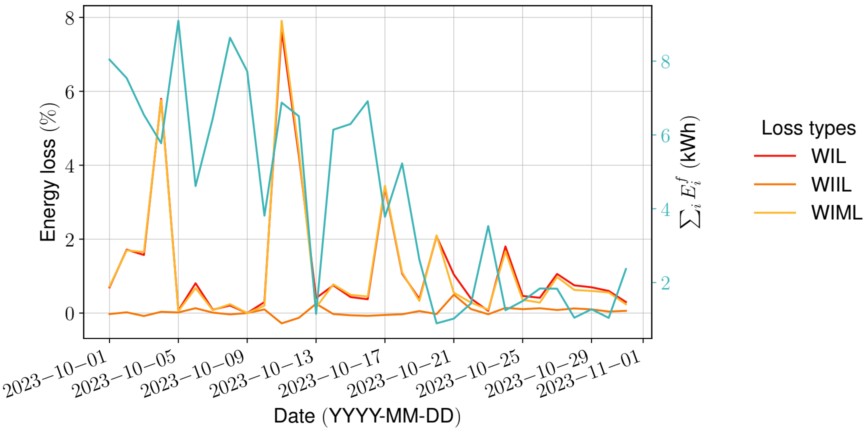

(a) Energy generation and wave-induced losses at the BAR location, October 2023.

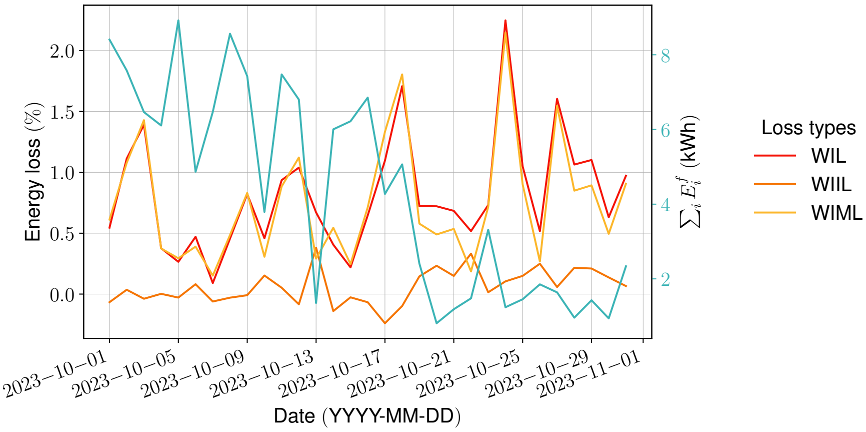

(b) Energy generation and wave-induced losses at the RIS location, October 2023.

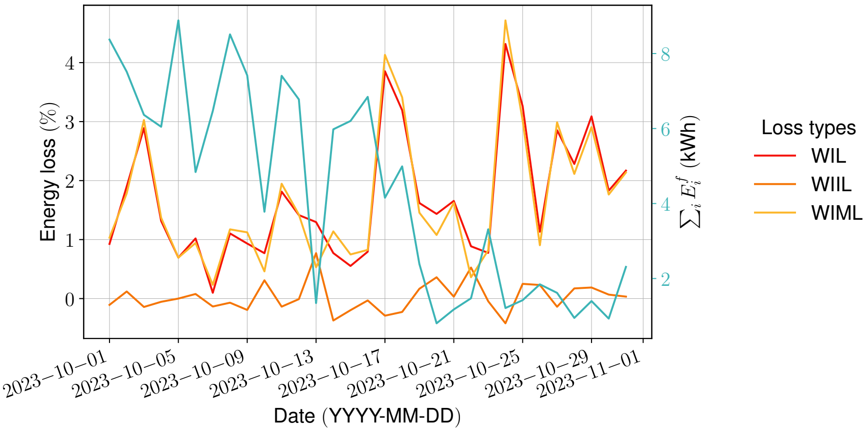

(c) Energy generation and wave-induced losses at the HAV location, October 2023.

Figure 3.14: WIL, WIIL, and WIML for October 2023 at the BAR (3.14a), RIS (3.14b), and HAV (3.14c) locations. The cyan line corresponds to the right vertical axis and shows the sum of the energy produced by each individual module in the FPV system.

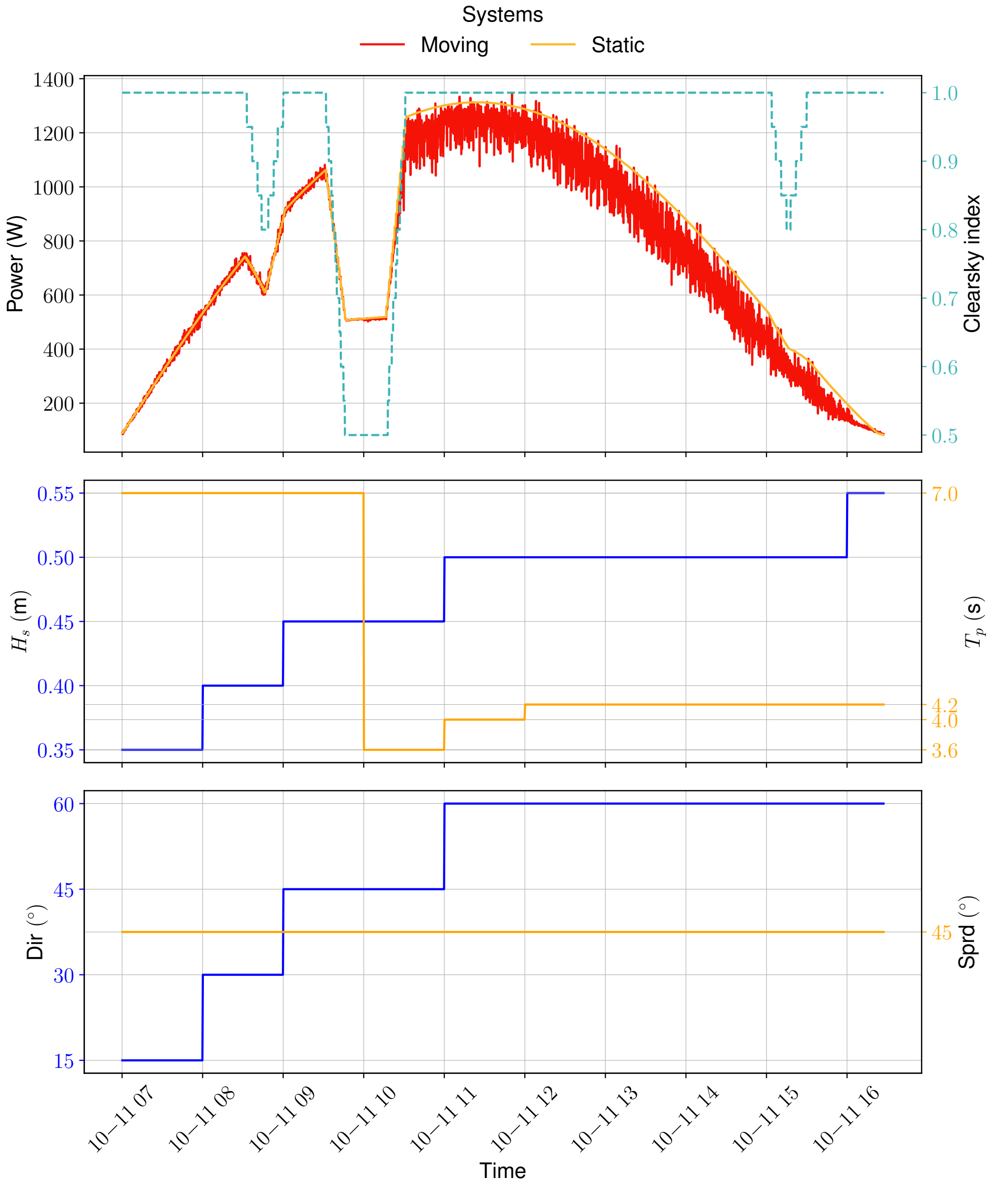

Figure 3.15: Power generation of the moving and static systems at the BAR location for October 11th 2023 along with the variations in sea-state variables. In the uppermost panel, the stippled cyan line represents the clearsky index, a measure of how sunny it is compared to the clearsky conditions. In the lower two panels, the blue lines correspond to the respective left vertical axis while the orange line corresponds to the respective right vertical axis.

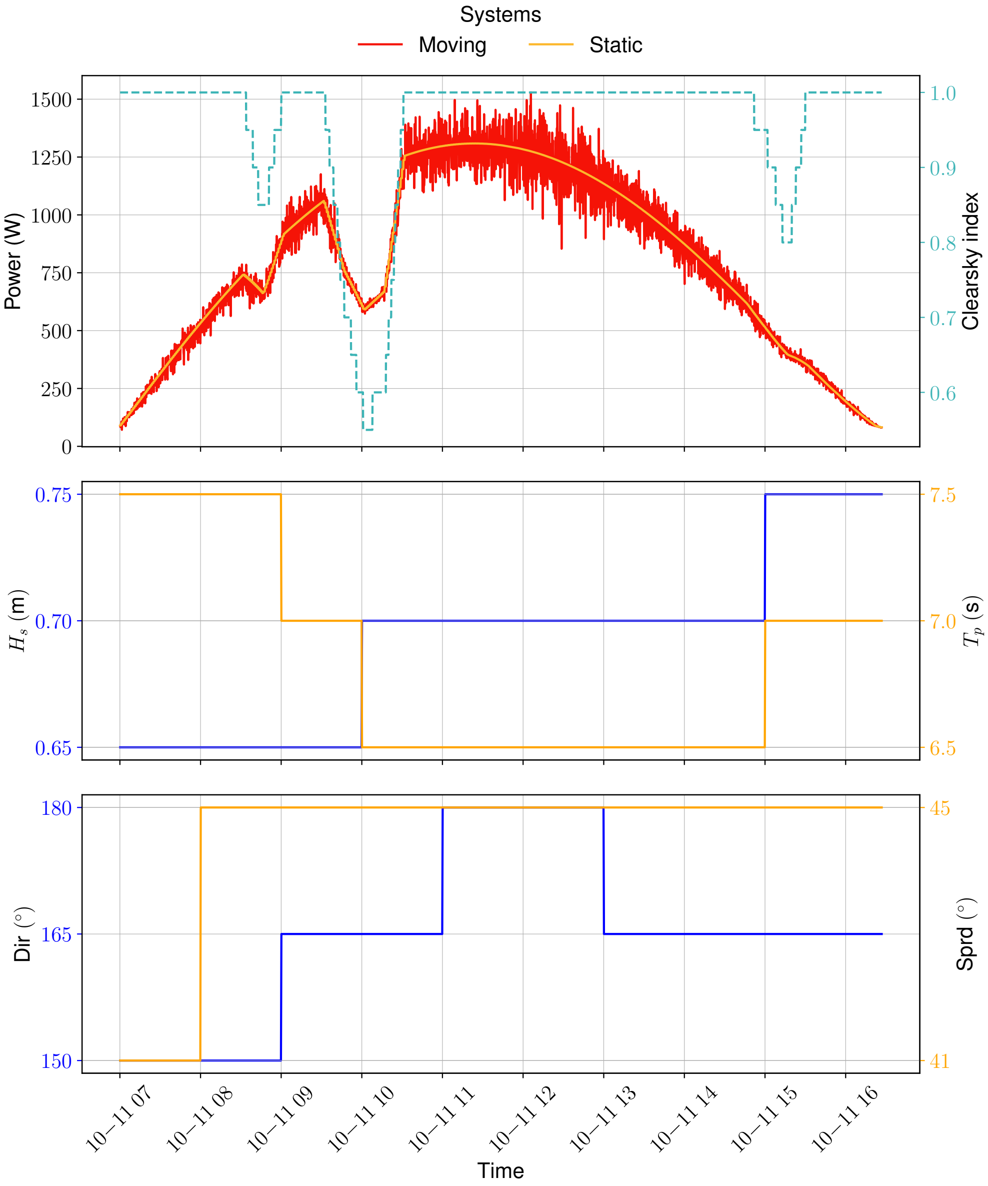

Figure 3.16: Power generation of the moving and static systems at the RIS location for October 11th 2023 along with the variations in sea-state variables. In the uppermost panel, the stippled cyan line represents the clearsky index, a measure of how sunny it is compared to the clearsky conditions. In the lower two panels, the blue lines correspond to the respective left vertical axis while the orange line corresponds to the respective right vertical axis.

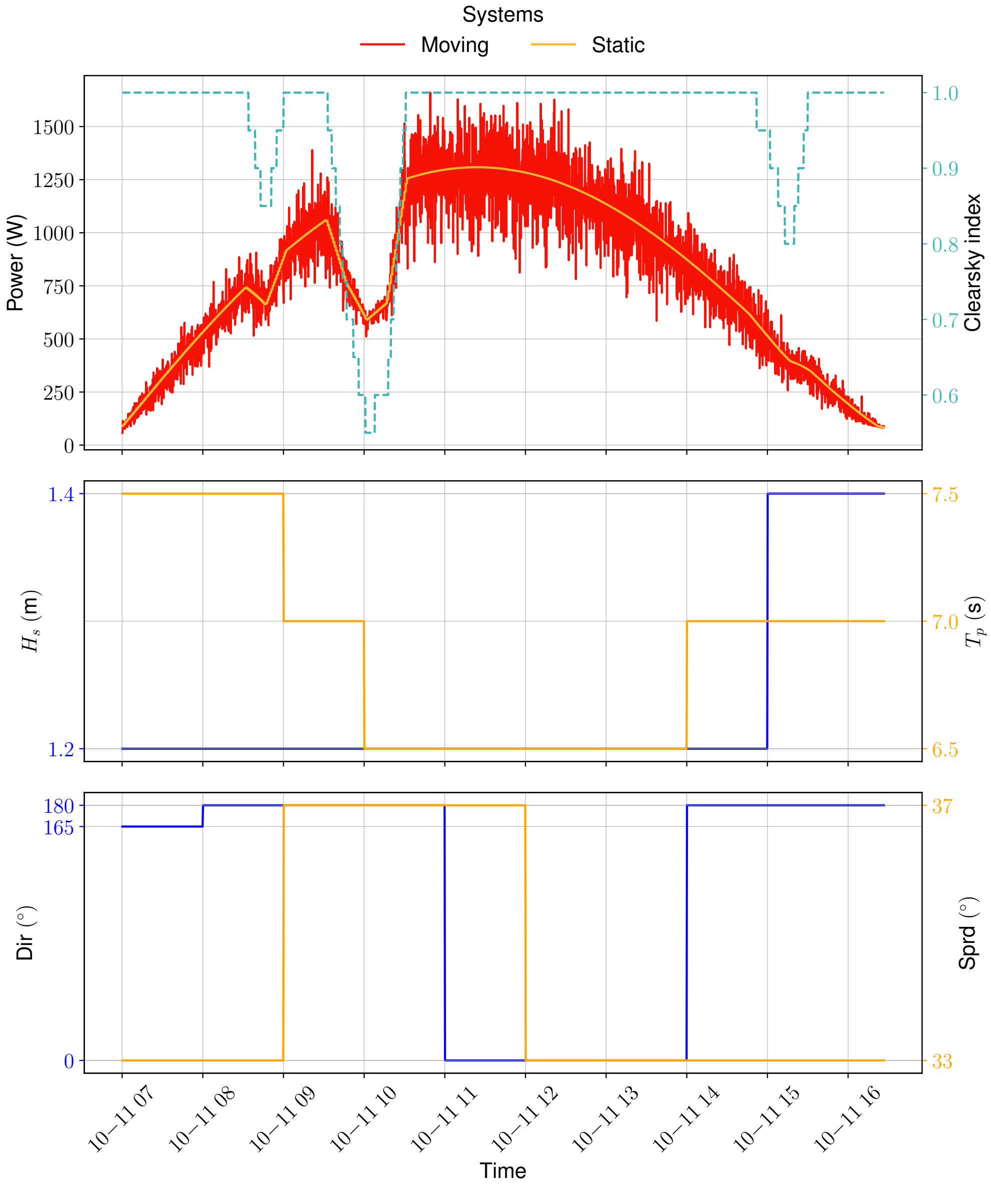

Figure 3.17: Power generation of the moving and static systems at the HAV location for October 11th 2023 along with the variations in sea-state variables. In the uppermost panel, the stippled cyan line represents the clearsky index, a measure of how sunny it is compared to the clearsky conditions. In the lower two panels, the blue lines correspond to the respective left vertical axis while the orange line corresponds to the respective right vertical axis.

3.3.3 The impact of the sea-states and irradiance conditions on the WIL

The sea-states are more calm further into Nordfjorden. In Figure 3.18, the HAV location experiences the highest waves, with H_s up to 3.2 m. The RIS and BAR locations experience lower wave-heights. BAR has the calmest see with $H_s = 0.7$ m as the largest significant wave height. Overall there is a high concentration of sea-states with $T_p = 2$ s at all locations. This may be due to the capping applied to the sea-states' T_p before simulating with 3DFloat, which cannot simulate sea-states with $T_p < 2$ s. The high concentration of sea-states with $T_p = 2$ s may be due to calmer sea surfaces at locations inside the skerries at the fjord entrance, which allows for short capillary waves: a sea surface with ripples. Although the HAV location experiences a high concentration of sea-states with $T_p = 2$ s, the location experiences a large amount of other sea-states as well. All three locations observe an upper-triangular shape to the combinations of H_s and T_p, although this shape is less visible at the BAR location. This triangular shape indicates that the SWAN wave model have processed combinations yielding waves larger than the steepness limit (3.4). Most frequent combinations of H_s and $T_p > 2$ are found in the centre of the triangular-shaped distribution. This indicates an overall calm sea surface at all locations, with the exception of the HAV location where Figure 3.18c shows a high number of sea-states with $H_s > 1$ m due to the direct exposure to the Skagerrak strait.

Steeper combinations of H_s and T_p, as seen in fig:res:mismatch:table:hs, increase the WIL. For each combination of H_s and T_p, the power generated by all occurrences of each combination is aggregated and used to compute their resulting WIL. Combinations with a single occurrence reflects a WIL for one hour only. To visualise the nuances in the WIL in Figure 3.19, the outlier events with $WIL > 10\%$ have been excluded and can be found in Table 3.6. The observed trend in fig:res:mismatch:table:hs, is an increase in the WIL for combinations of H_s and T_p which yield increasingly steeper waves. This is an expected trend based on the observations made in section 3.2, where the WIL increased with increasing H_s or decreasing T_p.

The distribution of incoming wave directions and directional spread is similar at the RIS and HAV locations, while it is different at the BAR location. In Figure 3.20, both the RIS and HAV locations experience a majority of waves originating from the south-east or north-west quadrants. Both locations are exposed to waves incoming from the east or south (see Figure 2.15), From north-west, at both the RIS and HAV locations, there are no sources of waves other than waves reflected at the shoreline. The large amount of waves with Dir = 0° at the HAV location is due to the shift (3.8) applied to Dir after the symmetry observed in section 3.2, which (due to the symmetry) carries no impact on the WIL. To the south and east, the RIS location is directly exposed to the Skagerrak strait. The extracted mean wave direction, from the SWAN wave model, results in a south-eastern origin when the waves come from the south and east at the same time. Therefore, it is reasonable that the RIS and HAV locations display similar distributions in sea-states. The BAR location is only exposed to new waves from the east. These waves may be reflected along the shoreline of the fjord. The BAR location is deep into the fjord, with short capillary waves reaching the location as a sum of reflected waves.

At all three locations the overall WIL is low for different combinations of incoming wave direction and directional spread. There is a tendency of increased WIL close to Dir = 90° as seen in Figure 3.21. The power generated is measured for all occurrences of each combination, of Dir and Sprd, and the resulting WIL is computed. Again, outliers with WIL > 10% have been excluded and can be found in Table 3.6. A general observation is a low wave-induced loss, with multiple cases of WIL = 0.0%. Most of the combinations with WIL = 0.0% occur at the BAR location, which experiences overall calmer sea-states. There are multiple cases of WIL > 5% at the HAV location. While some of those cases have a small sample size, other have not, such as Dir = 90° with Sprd = 41°. The larger WIL at the HAV location is due to rougher sea-states. In Figure 3.21, the density of large WIL values increases toward Dir = 90°. Based on the analysis of the incoming wave direction in section 3.2, the time of day for the smallest variations in the power generation of the moving system is at noon, when the azimuth of the sun is approximately normal to the system layout. For all other times, an incoming wave direction of = 90° would experience larger variations in the power generation and therefore, a higher WIL. For wave with Dir = 180°, the variations in the power generation of the moving FPV system are minimised twice a day. Thus, Dir = 180° has a higher likelihood of reducing the WIL than Dir = 90°, which explains the distribution of the WIL in Figure 3.21.

In Table 3.6, the outliers from Figure 3.19 show no particular behaviour, while the outliers from Figure 3.21 are all from the same day and within a similar time-frame. All outliers have a short T_p combined with an H_s in the upper range for that T_p (see figures 3.18 and 3.20). So, all the outliers are cases with steep waves. However, there are no apparent reasons for the large mismatch other than the incoming wave direction for the specific times. The time of day affects the impact of the incoming wave direction on the WIL, as discussed in section 3.2. The time of day for and the incoming wave direction of the outliers matches a timestamp where the impact of Dir on the WIL is large. The WIL is further increased by the steep waves. As another observation, the outliers from Figure 3.21 occur on the same day at approximately the same time-frame. This may indicate that the irradiance conditions affect the WIL, however after a manual inspection of the data, it is found that the clearsky index throughout the events was above 0.95 with almost no variations.

Table 3.6: Outlier cases excluded from Figure 3.19 and Figure 3.21. The criterion for exclusion is WIL > 10%. Each excluded case appeared only once.

Case	WIL (%)	Location	Hs (m)	Tp (s)	Sprd	Dir	Time
Hs-Tp	16.6	BAR	0.35	2.2	75°	45°	01-30 11 h
Hs-Tp	25.6	RIS	0.35	2.0	90°	45°	11-24 14 h
Hs-Tp	15.0	HAV	0.35	2.2	33°	105°	03-11 15 h
Dir-Sprd	14.6	BAR	0.2	2.6	33°	45°	01-27 14 h
Dir-Sprd	18.0	RIS	0.15	2.2	37°	30°	01-27 13 h
Dir-Sprd	10.8	HAV	0.25	2.0	29°	30°	01-27 13 h

In Figure 3.22, the convex trend in the WIL is a function of the clearsky index. The clearsky indices are categorised in bins of 0.1. The WIL of each bin based on their total power production. There is a global minimum in the WIL for clearsky indices between 0.2 and 0.5. For clearsky indices > 0.5, the WIL increases as well as for clearsky indices < 0.2. The large WIL for the lower and upper end of the clearsky indices indicates that, during those irradiance conditions, the FPV system amasses a larger difference in produced power. For the clearsky indices within the minima, there may be more variations which balance out the differences in power production over time.

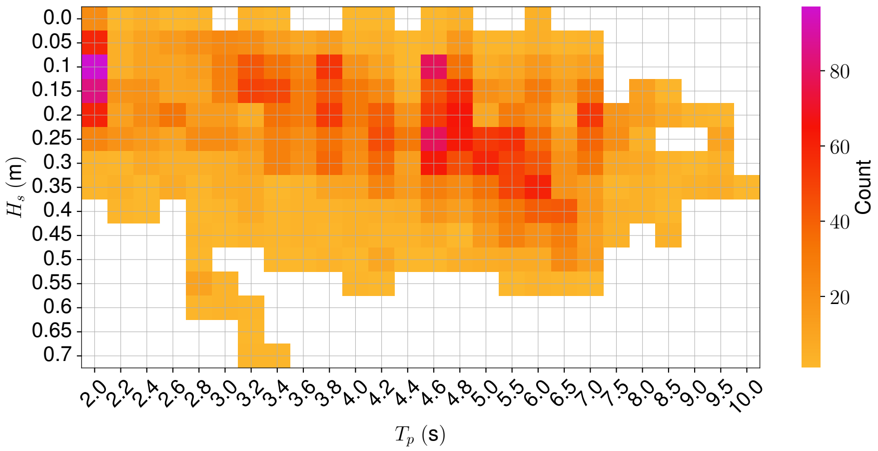

(a) H_s and T_p combinations appearing at the BAR location, 2023.

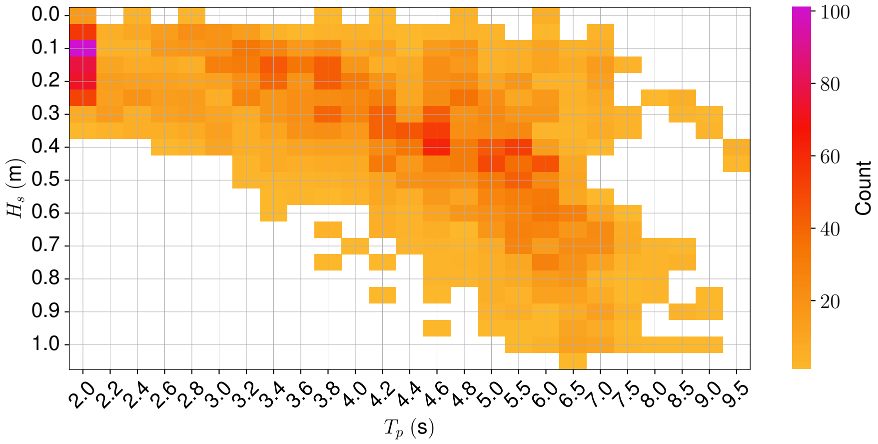

(b) H_s and T_p combinations appearing at the RIS location, 2023.

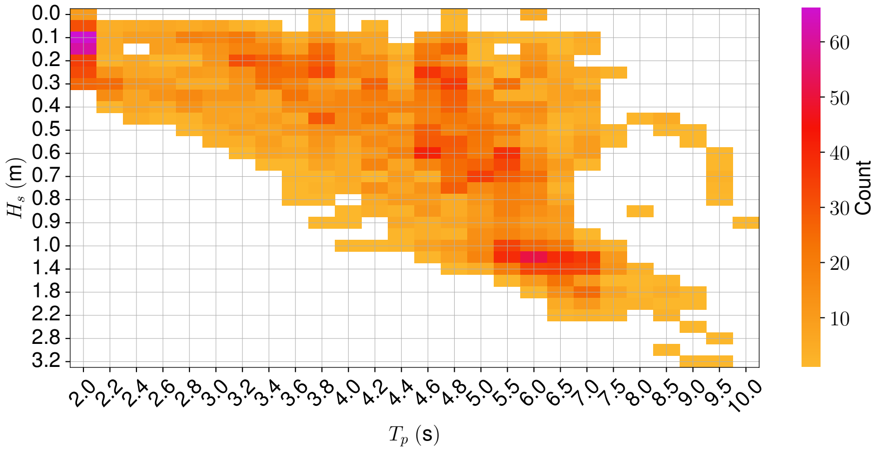

(c) H_s and T_p combinations appearing at the HAV location, 2023.

Figure 3.18: Number of occurrences of each combination of H_s and T_p at the BAR (3.18a), RIS (3.18b), and HAV (3.18c) locations. The combinations are those appearing for the year 2023 during daylight hours

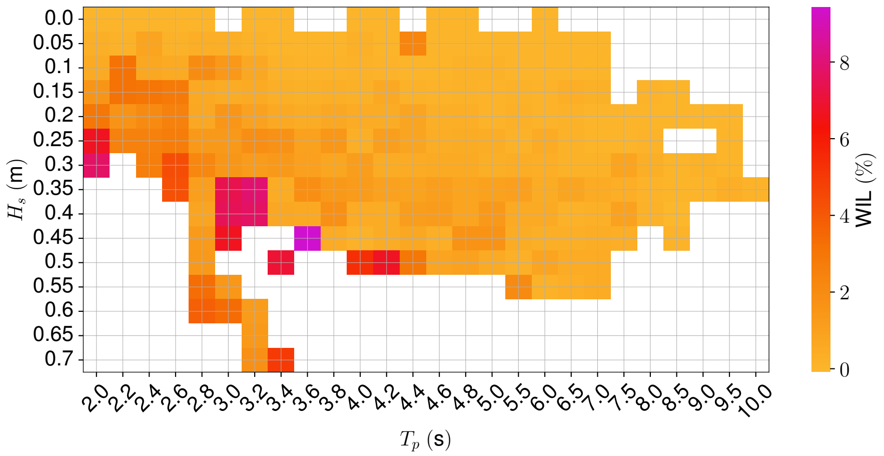

(a) WIL for combinations of H_s and T_p appearing at the BAR location, 2023.

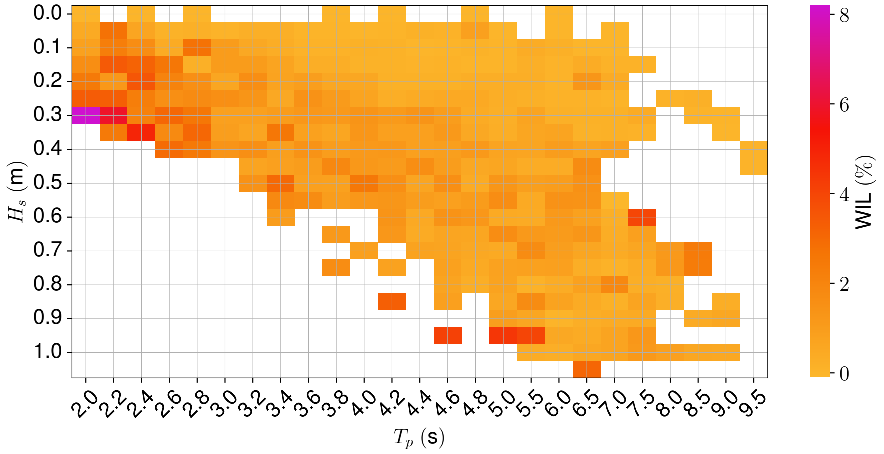

(b) WIL for combinations of H_s and T_p appearing at the RIS location, 2023.

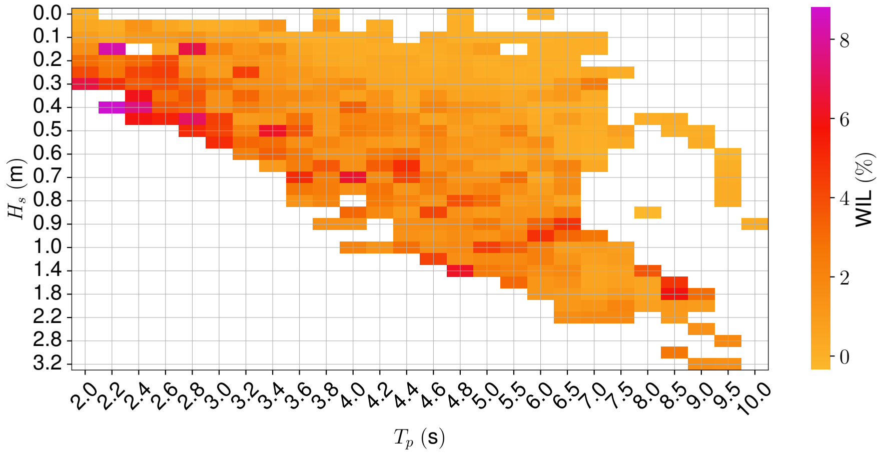

(c) WIL for combinations of H_s and T_p appearing at the HAV location, 2023.

Figure 3.19: Calculated WIL for each appearing combination of H_s and T_p at the BAR (3.19a), RIS (3.19b), and HAV (3.19c) locations. The combinations are those appearing for the year 2023 during daylight hours. The combinations with WIL > 10% have been excluded and can be found in Table 3.6.

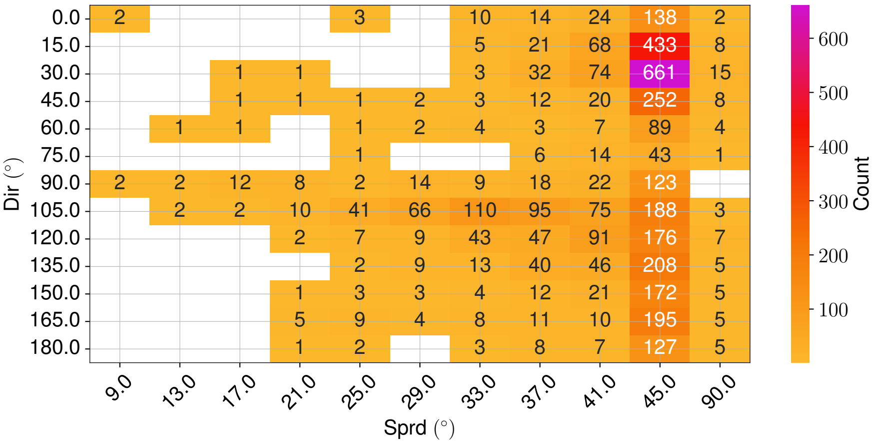

	9.0	13.0	17.0	21.0	25.0	29.0	33.0	37.0	41.0	45.0	90.0
0.0	2				3		10	14	24	138	2
15.0							5	21	68	433	8
30.0			1	1			3	32	74	661	15
45.0			1	1	1	2	3	12	20	252	8
60.0		1	1		1	2	4	3	7	89	4
75.0					1			6	14	43	1
90.0	2	2	12	8	2	14	9	18	22	123	
105.0		2	2	10	41	66	110	95	75	188	3
120.0				2	7	9	43	47	91	176	7
135.0					2	9	13	40	46	208	5
150.0				1	3	3	4	12	21	172	5
165.0				5	9	4	8	11	10	195	5
180.0				1	2		3	8	7	127	5

(a) Dir and Sprd combinations appearing at the BAR location, 2023.

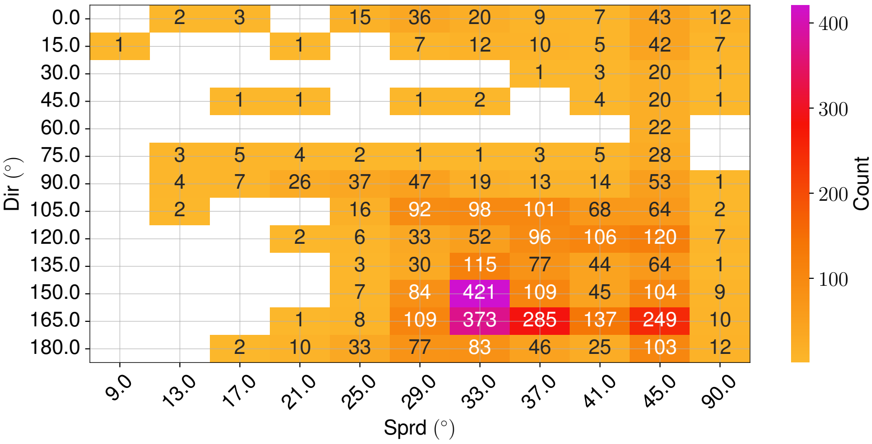

	9.0	13.0	17.0	21.0	25.0	29.0	33.0	37.0	41.0	45.0	90.0
0.0		2	3		15	36	20	9	7	43	12
15.0	1			1		7	12	10	5	42	7
30.0								1	3	20	1
45.0			1	1		1	2		4	20	1
60.0										22	
75.0		3	5	4	2	1	1	3	5	28	
90.0		4	7	26	37	47	19	13	14	53	1
105.0		2			16	92	98	101	68	64	2
120.0				2	6	33	52	96	106	120	7
135.0					3	30	115	77	44	64	1
150.0					7	84	421	109	45	104	9
165.0				1	8	109	373	285	137	249	10
180.0			2	10	33	77	83	46	25	103	12

(b) Dir and Sprd combinations appearing at the RIS location, 2023.

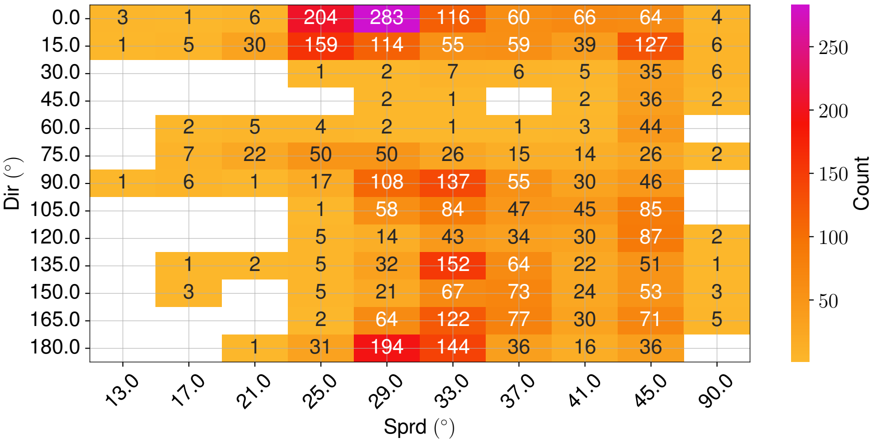

	13.0	17.0	21.0	25.0	29.0	33.0	37.0	41.0	45.0	90.0
0.0	3	1	6	204	283	116	60	66	64	4
15.0	1	5	30	159	114	55	59	39	127	6
30.0				1	2	7	6	5	35	6
45.0					2	1		2	36	2
60.0		2	5	4	2	1	1	3	44	
75.0		7	22	50	50	26	15	14	26	2
90.0	1	6	1	17	108	137	55	30	46	
105.0				1	58	84	47	45	85	
120.0				5	14	43	34	30	87	2
135.0		1	2	5	32	152	64	22	51	1
150.0		3		5	21	67	73	24	53	3
165.0				2	64	122	77	30	71	5
180.0			1	31	194	144	36	16	36	

(c) Dir and Sprd combinations appearing at the HAV location, 2023.

Figure 3.20: Number of occurrences of each combination of incoming wave direction and directional spread at the BAR (3.20a), RIS (3.20b), and HAV (3.20c) locations. The combinations are those appearing for the year 2023 during daylight hours

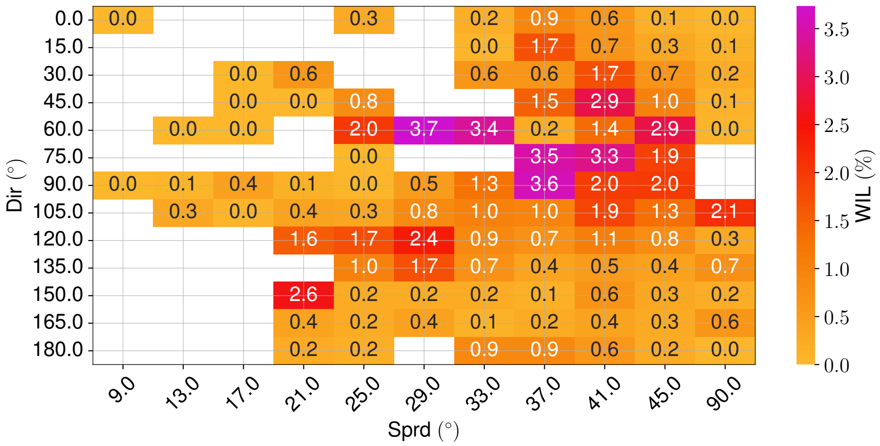

Dir (°)	9.0	13.0	17.0	21.0	25.0	29.0	33.0	37.0	41.0	45.0	90.0
0.0	0.0				0.3		0.2	0.9	0.6	0.1	0.0
15.0							0.0	1.7	0.7	0.3	0.1
30.0			0.0	0.6			0.6	0.6	1.7	0.7	0.2
45.0			0.0	0.0	0.8			1.5	2.9	1.0	0.1
60.0		0.0	0.0		2.0	3.7	3.4	0.2	1.4	2.9	0.0
75.0					0.0			3.5	3.3	1.9	
90.0	0.0	0.1	0.4	0.1	0.0	0.5	1.3	3.6	2.0	2.0	
105.0		0.3	0.0	0.4	0.3	0.8	1.0	1.0	1.9	1.3	2.1
120.0				1.6	1.7	2.4	0.9	0.7	1.1	0.8	0.3
135.0					1.0	1.7	0.7	0.4	0.5	0.4	0.7
150.0				2.6	0.2	0.2	0.2	0.1	0.6	0.3	0.2
165.0				0.4	0.2	0.4	0.1	0.2	0.4	0.3	0.6
180.0				0.2	0.2		0.9	0.9	0.6	0.2	0.0

(a) WIL for combinations of Dir and Sprd appearing at the BAR location, 2023.

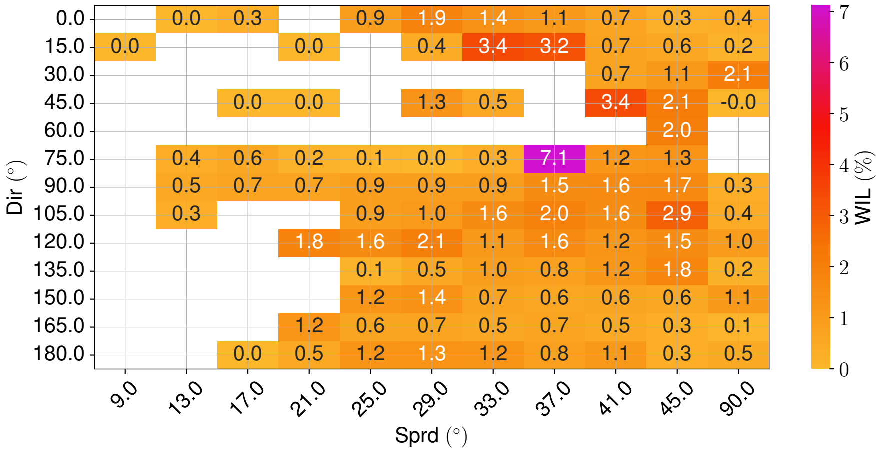

Dir (°)	9.0	13.0	17.0	21.0	25.0	29.0	33.0	37.0	41.0	45.0	90.0
0.0		0.0	0.3		0.9	1.9	1.4	1.1	0.7	0.3	0.4
15.0	0.0			0.0		0.4	3.4	3.2	0.7	0.6	0.2
30.0									0.7	1.1	2.1
45.0			0.0	0.0		1.3	0.5		3.4	2.1	-0.0
60.0										2.0	
75.0		0.4	0.6	0.2	0.1	0.0	0.3	7.1	1.2	1.3	
90.0		0.5	0.7	0.7	0.9	0.9	0.9	1.5	1.6	1.7	0.3
105.0		0.3			0.9	1.0	1.6	2.0	1.6	2.9	0.4
120.0				1.8	1.6	2.1	1.1	1.6	1.2	1.5	1.0
135.0					0.1	0.5	1.0	0.8	1.2	1.8	0.2
150.0					1.2	1.4	0.7	0.6	0.6	0.6	1.1
165.0				1.2	0.6	0.7	0.5	0.7	0.5	0.3	0.1
180.0			0.0	0.5	1.2	1.3	1.2	0.8	1.1	0.3	0.5

(b) WIL for combinations of Dir and Sprd appearing at the RIS location, 2023.

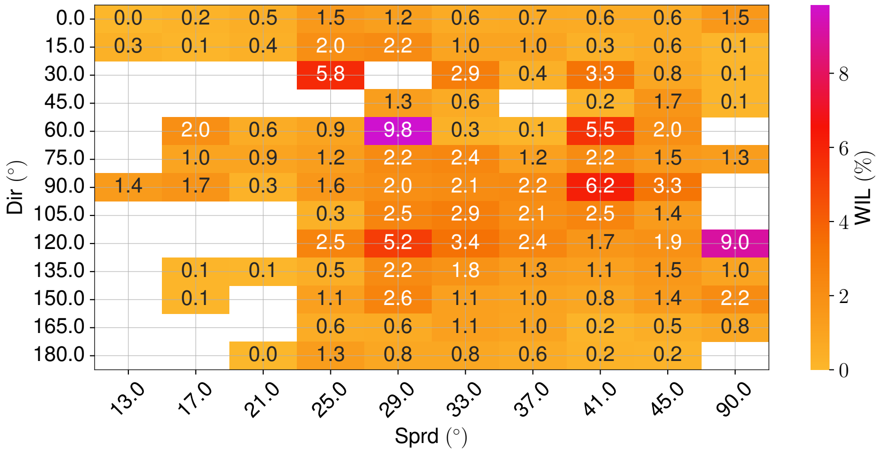

Dir (°)	13.0	17.0	21.0	25.0	29.0	33.0	37.0	41.0	45.0	90.0
0.0	0.0	0.2	0.5	1.5	1.2	0.6	0.7	0.6	0.6	1.5
15.0	0.3	0.1	0.4	2.0	2.2	1.0	1.0	0.3	0.6	0.1
30.0				5.8		2.9	0.4	3.3	0.8	0.1
45.0					1.3	0.6		0.2	1.7	0.1
60.0		2.0	0.6	0.9	9.8	0.3	0.1	5.5	2.0	
75.0		1.0	0.9	1.2	2.2	2.4	1.2	2.2	1.5	1.3
90.0	1.4	1.7	0.3	1.6	2.0	2.1	2.2	6.2	3.3	
105.0				0.3	2.5	2.9	2.1	2.5	1.4	
120.0				2.5	5.2	3.4	2.4	1.7	1.9	9.0
135.0		0.1	0.1	0.5	2.2	1.8	1.3	1.1	1.5	1.0
150.0		0.1		1.1	2.6	1.1	1.0	0.8	1.4	2.2
165.0				0.6	0.6	1.1	1.0	0.2	0.5	0.8
180.0			0.0	1.3	0.8	0.8	0.6	0.2	0.2	

(c) WIL for combinations of Dir and Sprd appearing at the HAV location, 2023.

Figure 3.21: Calculated WIL for each appearing combination of incoming wave direction and directional spread at the BAR (3.21a), RIS (3.21b), and HAV (3.21c) locations. The combinations are those appearing for the year 2023 during daylight hours. The combinations with WIL $> 10\%$ have been excluded and can be found in Table 3.6.

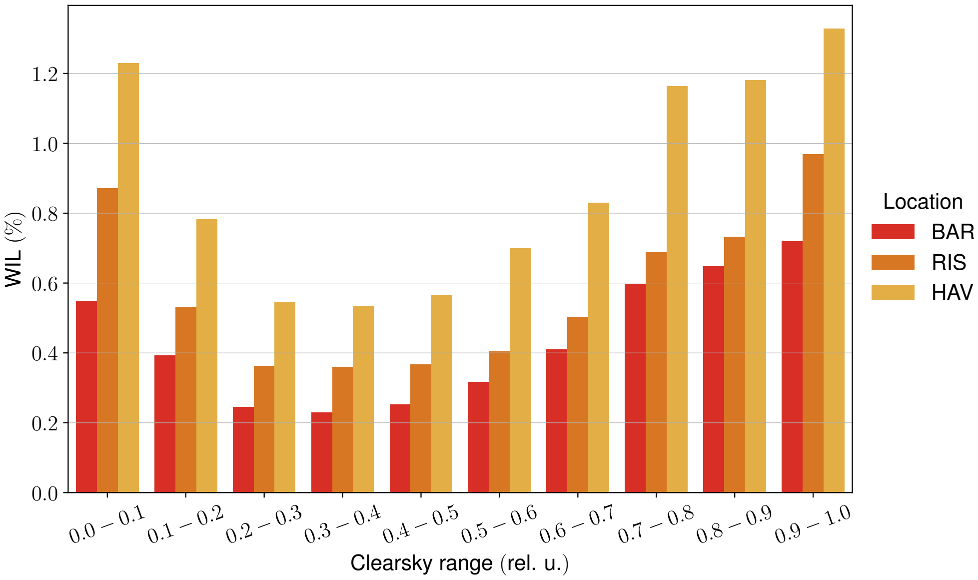

Figure 3.22: WIL computed from the aggregated power generation of clearsky index ranges at the BAR, RIS, and HAV locations. The clearsky indices throughout the year 2023 were grouped into bins of size 0.1. For each bin, the power generation is aggregated to compute the WIL.

3.3.4 10-module FPV system with $15°$ southward tilt

When placed with a 15° initial southward tilt, the 10-module FPV system shows a significant reduction in the WIL and WIML, and an increase in the WIIL. Table 3.7 shows an expected increase in the generated energy for the year 2023 compared to Table 3.3, when placing the FPV system with an initial 15° roll. The differences in the energy generated by the moving systems and their respective static systems are smaller than the differences found for the systems with no initial tilt. The generated energy by the static systems at each location is increased by $\sim 16\%$ in comparison with Table 3.3. The energy generated by the moving systems, with 15° initial tilt, show smaller differences in kWh to their respective static systems than for the system placed with no initial tilt. This reduction in difference is reflected in the reduction of the WIL at all three locations. Compared to Table 3.3, the WIL in Table 3.7 is reduced by $\sim 30\%$. With an initial 15° roll, the FPV system placed at RIS generates more energy than when placed at the BAR location yet the energy loss between the two locations differs by 0.055 pp, making the RIS location the most favourable location in terms of energy generation out of the three locations. The reduction in the WIL is due to the reduction in the WIML and limited by the increase in the WIIL, in terms of kWh. The WIIL increased significantly at all three locations when placing the FPV system with an initial southward tilt. The increase in the WIIL means that, on average, the wave-induced movements of the modules move them away from a more favourable orientation. The WIML remains large in comparison to the WIIL, which is in contrast with the results from Chen et al..

Table 3.7: Energy yield and wave-induced losses of a 10-module FPV system with 15° initial tilt for the year 2023 at the BAR, RIS and HAV locations.

	E^f (MWh)	E^s (MWh)	$\sum_i E_i^f$ (MWh)	WIL (%)	WIML (%)	WIIL (%)
BAR	3.744	3.768	3.766	0.622	0.587	0.035
RIS	3.783	3.809	3.807	0.677	0.620	0.057
HAV	3.769	3.809	3.805	1.041	0.944	0.098

The monthly and daily average wave-induced losses are more similar when the FPV system is placed with an initial 15° southward tilt. Table 3.8 shows a similar trend in the standard deviations for the FPV systems placed with an initial tilt as the systems placed with no initial tilt (found in Table 3.5). The standard deviations are larger on the daily scale than on the monthly scale, with the daily standard deviations being larger than their respective average. In contrast, the average monthly and daily values for the WIL, WIML, and WIIL respectively are more similar in the daily and monthly time scales in all three locations. The BAR location shows the largest difference in the average values with ~ 0.1 pp, for instance the difference between the monthly and daily average of the WIML at the BAR location is 0.12 pp. The RIS and HAV locations show differences ≤ 0.03 pp.

The similarity between the average monthly and daily values in all wave-induced losses is due to an overall reduction in the wave-induced losses on a monthly scale. Figure 3.23 shows the wave-induced losses and $\sum_i^N E_i^f$ of the FPV system placed with an initial 15° roll, for the year 2023. The differences in the profile of the wave-induced losses are similar to those found for the system with no initial tilt. In contrast with

Table 3.8: Monthly and daily mean with standard deviation for the WIL, WIML, and WIL at the BAR, RIS, and HAV locations. The systems are simulated with an initial 15° southward tilt.

		BAR	RIS	HAV
WIL (%)	Monthly	0.82 ± 0.38	0.78 ± 0.32	1.33 ± 0.65
	Daily	0.69 ± 1.04	0.76 ± 0.81	1.32 ± 1.41
WIML (%)	Monthly	0.78 ± 0.38	0.73 ± 0.31	1.23 ± 0.63
	Daily	0.66 ± 1.02	0.70 ± 0.80	1.22 ± 1.40
WIIL (%)	Monthly	0.03 ± 0.01	0.06 ± 0.02	0.10 ± 0.04
	Daily	0.03 ± 0.07	0.05 ± 0.06	0.10 ± 0.13

Figure 3.13, Figure 3.23 shows a clear positive WIIL throughout the year reinforcing the observations from Table 3.7. In addition, the the scale of the WIL and WIML have been reduced with the maximum WIL being $\sim 1.4\%$, $\sim 1.3\%$, and $\sim 2.5\%$ at the BAR, RIS, and HAV locations, respectively. With the monthly variations being smaller for the system with an initial tilt, the similarities in the monthly and daily averages of the wave-induced losses, in Table 3.8, are justified.

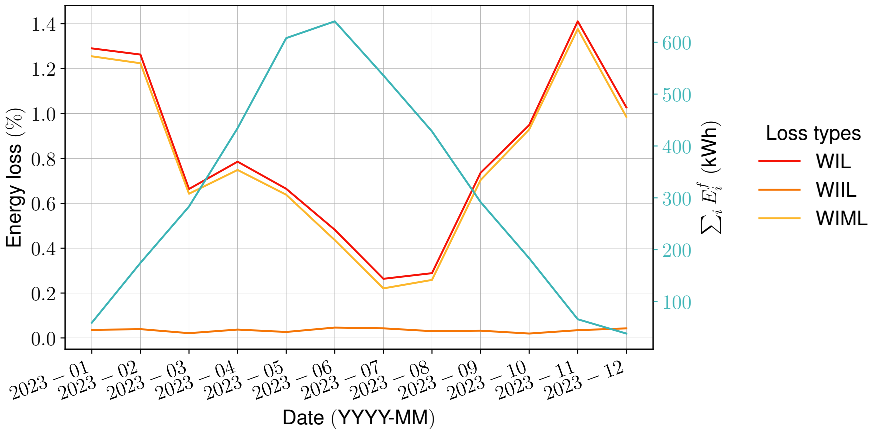

(a) Wave-induced losses at the BAR location, 2023.

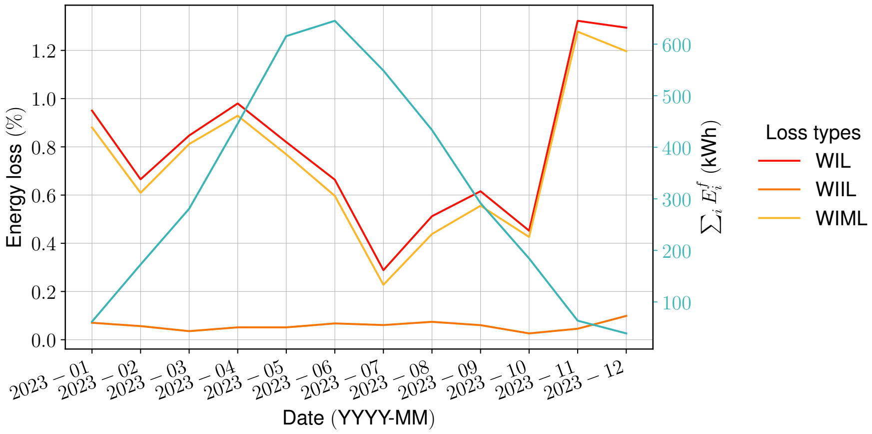

(b) Wave-induced losses at the RIS location, 2023.

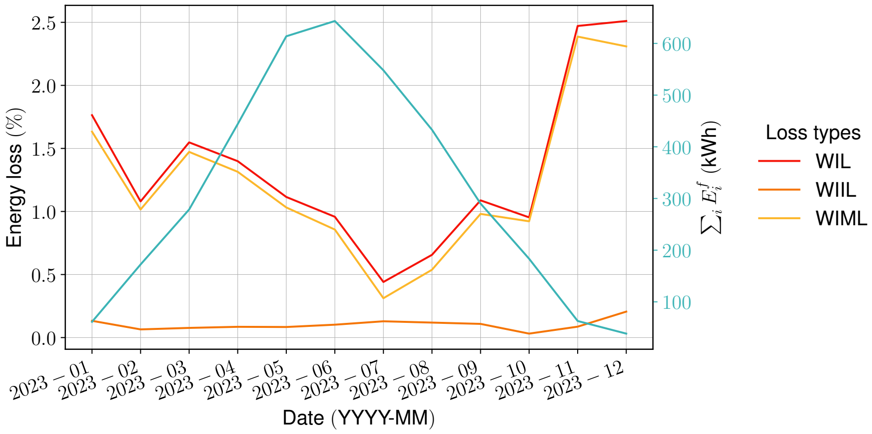

(c) Wave-induced losses at the HAV location, 2023.

Figure 3.23: WIL, WIIL, and WIML for 2023 at the BAR (3.13a), RIS (3.13b), and HAV (3.13c) locations. The cyan line corresponds to the right vertical axis and shows the sum of the energy produced by each individual module in the FPV system.

Chapter 4

Conclusions

I developed a pipeline to estimate the wave-induced losses of FPV at locations requiring high spatial resolution. To model the sea-states at the chosen locations, the pipeline uses uses the third generation SWAN wave model. SWAN uses input wind and bathymetry data as well as wave spectra data at the boundaries. From the output sea-states, 3DFloat simulates the FPV module movements based on the WFM assumptions that the float strictly follows the sea surface. The power production of the FPV system is calculated based on the module orientation at every 10 s time step, from which the resulting wave induced losses are found.

The simulated module movements with 3DFloat with the WFM assumptions show differences in the movement range compared to site measurements. The site measurements contained calm sea-states with $H_s < 0.12$ m, which limited the validation of the simulated movements. The site measurements showed restricted movement in the roll which currently cannot be replicated by 3DFloat with the WFM assumptions. Out of 10 sampled sea-states, the largest difference in the standard deviations, between the site measurements and the simulated module movements, was 1.323° in the roll. The site measurements showed no apparent restrictions in the pitch rotations where the largest difference in the standard deviations was 0.358°. In the case of $H_s = 0.09$ m and $T_p = 2$ s, the simulated movements by 3DFloat showed a wider movement range than the module movements measured at the site.

A sea-state variable sensitivity scan was performed, which enabled a reduction in required simulation time with 3DFloat by up to 81.5%. The peak enhancement factor was found to have the least impact of the WIL. The wave directional spread was found to change the WIL by up to 2% for short-crested wave surfaces, where Sprd $< 45°$. The largest impact on the WIL was found for combinations of increasing H_s and decreasing T_p: steeper waves. The impact of the incoming wave direction on the WIL has a 180-degree rotational symmetry and varies as a function of the sun's azimuth. The resolution of the sea-state variables output from the SWAN model was reduced before simulating the sea surface with 3DFloat.

The WIL is found to decrease with calmer sea states. Of the BAR, RIS, and HAV locations, the yearly WIL for a 10-module FPV system with no initial tilt is smallest at the BAR location, which experienced an overall calmer sea surface, with WIL = 0.837%. The RIS location, an area where skerries dampen the waves coming from the open sea, showed WIL = 0.945%. While the HAV location, which is directly exposed to the Skagerrak strait, showed a significantly larger WIL at 1.429%. These results are an overestimation given the larger range of movement of the simulated module movements by 3DFloat.

The definitions of the WIML and WIIL are intuitive and reasonable based on the results found in this thesis. The electrical mismatch losses are significantly larger than the optical losses, by an order of magnitude. For an FPV system placed with no initial tilt at the BAR, RIS, and HAV locations, the WIIL is negligible, while the WIML is significant and determines the WIL. For an FPV system placed with a 15° initial tilt at the BAR, RIS, and HAV locations, the WIIL remains small in comparison to the WIML, albeit larger. The WIIL increases when placing the FPV system with a favourable initial tilt due to the wave-induced movements moving the modules away from a favourable orientation. The WIML decreases when placing the FPV system with a favourable initial tilt, yet remains determined by the combination of irradiance and sea-state conditions.

4.1 Propositions for future work

The WFM assumptions allow for a simple methodology to extract FPV module movements. However, for a complete FPV system simulation, it would be beneficial to upgrade the 3DFloat simulation tool to include structural interactions between the floats and mooring lines. Including the impact of mooring lines would capture the details and interdependencies between the float movements and thus on the resulting WIL.

The pipeline created in this work facilitates the generation of FPV system energy generation data at specific sites with local sea-state and irradiance conditions. Performing energy yield modelling at multiple geographically different locations can create varied data which can be used to perform regression tasks Performing multivariate regression, for instance with ElasticNet or XGBoost, could potentially reduce the computation time required for an estimate of the WIL at specific locations.

This work has not considered the energy loss from inverters. With constantly varying module orientations, the inverters may increase the wave-induced losses with wave-induced inverter losses. The optimal operating voltage of an FPV array varies due to the constant motion of the array modules. Therefore, more energy may be lost to wave-induced motions depending on the update frequency of the operating voltage by the inverter.

Finally, the pipeline can be expanded to include thermal effects in the modelled FPV systems. With the `pvmismatch` package, one can update the operating temperature of the cells or modules in an array. Expanding the pipeline would allow for a more complete assessment of FPV energy yield.

Bibliography

[1] A. Alcañiz et al. ‘Offshore floating PV–DC and AC yield analysis considering wave effects’. In: *Energy Conversion and Management* 300 (Jan. 2024), p. 117897. ISSN: 01968904. DOI: 10.1016/j.enconman.2023.117897. URL: https://linkinghub.elsevier.com/retrieve/pii/S0196890423012438 (visited on 26/06/2024).

[2] J.-V. Björkqvist et al. ‘WAM, SWAN and WAVEWATCH III in the Finnish archipelago – the effect of spectral performance on bulk wave parameters’. In: *Journal of Operational Oceanography* 13.1 (Jan. 2020), pp. 55–70. ISSN: 1755-876X. DOI: 10.1080/1755876X.2019.1633236. URL: https://doi.org/10.1080/1755876X.2019.1633236 (visited on 28/04/2025).

[3] N Booij, Leo Holthuijsen and R Ris. ‘THE "SWAN" WAVE MODEL FOR SHALLOW WATER’. In: *Coastal Engineering* 1 (Jan. 1996).

[4] Judith Bosboom and Marcel J F Stive. ‘Coastal Dynamics’. en. In: ().

[5] Katherine Calvin et al. *IPCC, 2023: Climate Change 2023: Synthesis Report. Contribution of Working Groups I, II and III to the Sixth Assessment Report of the Intergovernmental Panel on Climate Change [Core Writing Team, H. Lee and J. Romero (eds.)]. IPCC, Geneva, Switzerland.* en. Tech. rep. Edition: First. Intergovernmental Panel on Climate Change (IPCC), July 2023. DOI: 10.59327/IPCC/AR6-9789291691647. URL: https://www.ipcc.ch/report/ar6/syr/ (visited on 23/04/2025).

[6] *Center for Satellite Applications and Research - NOAA / NESDIS / STAR.* en-US. URL: https://www.star.nesdis.noaa.gov/star/index.php (visited on 15/03/2025).

[7] Kuixiao Chen et al. ‘Wave Induced Losses Simulation of Floating Solar Photovoltaic Systems at Open Waters’. en. In: OnePetro, June 2023. URL: https://dx.doi.org/ (visited on 16/05/2025).

[8] *Consequences of climate change - European Commission.* en. URL: https://climate.ec.europa.eu/climate-change/consequences-climate-change_en (visited on 29/04/2025).

[9] *CryoSat-2 operations.* en. URL: https://www.esa.int/Enabling_Support/Operations/CryoSat-2_operations (visited on 15/03/2025).

[10] Erdem Cuce et al. ‘Floating PVs in Terms of Power Generation, Environmental Aspects, Market Potential, and Challenges’. en. In: *Sustainability* 14.5 (Jan. 2022). Number: 5 Publisher: Multidisciplinary Digital Publishing Institute, p. 2626. ISSN: 2071-1050. DOI: 10.3390/su14052626. URL: https://www.mdpi.com/2071-1050/14/5/2626 (visited on 24/04/2025).

[11] Maarten Dörenkämper. ‘INFLUENCE OF WAVE INDUCED MOVEMENTS ON THE PERFORMANCE OF FLOATING PV SYSTEMS’. en. In: ().

[12] Maarten Dörenkämper et al. 'The cooling effect of floating PV in two different climate zones: A comparison of field test data from the Netherlands and Singapore'. In: *Solar Energy* 214 (Jan. 2021), pp. 239–247. ISSN: 0038-092X. DOI: 10.1016/j.solener.2020.11.029. URL: https://www.sciencedirect.com/science/article/pii/S0038092X20311853 (visited on 24/04/2025).

[13] *Drifting buoys - DBCP*. en-GB. https://www.oceanobservers.org/Learn-about-observing-the-ocean/Drifting-buoys-DBCP. Accessed: 2025-02-17. URL: https://www.oceanobservers.org/Learn-about-observing-the-ocean/Drifting-buoys-DBCP (visited on 17/02/2025).

[14] *Electricity – Renewables 2023 – Analysis*. en-GB. Jan. 2024. URL: https://www.iea.org/reports/renewables-2023/electricity (visited on 29/04/2025).

[15] *Envisat - Earth Online*. en. URL: https://earth.esa.int/eogateway/missions/envisat (visited on 15/03/2025).

[16] *ERS-1 (European Remote-Sensing Satellite-1) - eoPortal*. en. URL: https://www.eoportal.org/satellite-missions/ers-1#eop-quick-facts-section (visited on 15/03/2025).

[17] *ERS-2*. en. URL: https://www.esa.int/Enabling_Support/Operations/ERS-2 (visited on 15/03/2025).

[18] Lewis W. Farrar et al. 'Floating solar PV to reduce water evaporation in water stressed regions and powering water pumping: Case study Jordan'. In: *Energy Conversion and Management* 260 (May 2022), p. 115598. ISSN: 0196-8904. DOI: 10.1016/j.enconman.2022.115598. URL: https://www.sciencedirect.com/science/article/pii/S0196890422003946 (visited on 24/04/2025).

[19] S. Zahra Golroodbari and Wilfried Van Sark. 'Simulation of performance differences between offshore and land-based photovoltaic systems'. en. In: *Progress in Photovoltaics: Research and Applications* 28.9 (Sept. 2020), pp. 873–886. ISSN: 1062-7995, 1099-159X. DOI: 10.1002/pip.3276. URL: https://onlinelibrary.wiley.com/doi/10.1002/pip.3276 (visited on 27/02/2025).

[20] GEBCO Bathymetric Compilation Group 2024. *GEBCO_2024 Grid*. English. Archive Location: World Publisher: NERC EDS British Oceanographic Data Centre NOC. July 2024. DOI: 10.5285/1c44ce99-0a0d-5f4f-e063-7086abc0ea0f. URL: https://www.bodc.ac.uk/data/published_data_library/catalogue/10.5285/1c44ce99-0a0d-5f4f-e063-7086abc0ea0f (visited on 24/03/2025).

[21] Hilde Haakenstad et al. 'NORA3: A Nonhydrostatic High-Resolution Hindcast of the North Sea, the Norwegian Sea, and the Barents Sea'. en. In: *Journal of Applied Meteorology and Climatology* 60.10 (Oct. 2021), pp. 1443–1464. ISSN: 1558-8424, 1558-8432. DOI: 10.1175/JAMC-D-21-0029.1. URL: https://journals.ametsoc.org/view/journals/apme/60/10/JAMC-D-21-0029.1.xml (visited on 31/01/2025).

[22] John E. Hay. 'Calculating solar radiation for inclined surfaces: Practical approaches'. In: *Renewable Energy*. Solar radiation, environment and climate change 3.4 (June 1993), pp. 373–380. ISSN: 0960-1481. DOI: 10.1016/0960-1481(93)90104-O. URL: https://www.sciencedirect.com/science/article/pii/096014819390104O (visited on 07/04/2025).

[23] Hans Hersbach et al. 'The ERA5 global reanalysis'. en. In: *Quarterly Journal of the Royal Meteorological Society* 146.730 (2020). _eprint: https://onlinelibrary.wiley.com/doi/pdf/10.1002/qj.3803, pp. 1999–2049. ISSN: 1477-870X. DOI: 10.1002/qj.3803. URL: https://onlinelibrary.wiley.com/doi/abs/10.1002/qj.3803 (visited on 14/01/2025).

[24] Jiamin Huang et al. 'Arid AREAS Water-Piled Photovoltaic Prevents Evaporation Effects Research'. en. In: *Water* 15.21 (Jan. 2023). Number: 21 Publisher: Multidisciplinary Digital Publishing Institute, p. 3716. ISSN: 2073-4441. DOI: 10.3390/w15213716. URL: https://www.mdpi.com/2073-4441/15/21/3716 (visited on 24/04/2025).

[25] IRENA. *Renewable Power Generation Costs in 2023*. Abu Dhabi, 2024.

[26] *Jason 2*. en-US. URL: https://www.jpl.nasa.gov/missions/jason-2/ (visited on 15/03/2025).

[27] Kartverket. *Terrain models of the seabed 50m grid*. https://geonorge.no:/geonetworktest/srv/api/records/67a3a191-49cc-45bc-baf0-eaaf7c513549. Accessed: 2025-01-31. URL: https://geonorge.no:/geonetworktest/srv/api/records/67a3a191-49cc-45bc-baf0-eaaf7c513549 (visited on 31/01/2025).

[28] G. J. Komen et al. *Dynamics and Modelling of Ocean Waves*. Cambridge: Cambridge University Press, 1994. ISBN: 978-0-521-57781-6. DOI: 10.1017/CBO9780511628955. URL: https://www.cambridge.org/core/books/dynamics-and-modelling-of-ocean-waves/767155B50D6E29B0F62729F29C2DE124 (visited on 27/01/2025).

[29] Dag Lindholm et al. 'Heat loss coefficients computed for floating PV modules'. en. In: *Progress in Photovoltaics: Research and Applications* 29.12 (2021). _eprint: https://onlinelibrary.wiley.com/doi/pdf/10.1002/pip.3451, pp. 1262–1273. ISSN: 1099-159X. DOI: 10.1002/pip.3451. URL: https://onlinelibrary.wiley.com/doi/abs/10.1002/pip.3451 (visited on 24/04/2025).

[30] Gaëtan Masson et al. 'Snapshot 2025'. en-US. In: (Apr. 2025). URL: https://iea-pvps.org/snapshot-reports/snapshot-2025/ (visited on 20/05/2025).

[31] *Moored buoys - DBCP*. en-GB. https://www.oceanobservers.org/Learn-about-observing-the-ocean/Moored-buoys-DBCP. Accessed: 2025-02-17. URL: https://www.oceanobservers.org/Learn-about-observing-the-ocean/Moored-buoys-DBCP (visited on 17/02/2025).

[32] United Nations. *What Is Climate Change?* en. Publisher: United Nations. URL: https://www.un.org/en/climatechange/what-is-climate-change (visited on 29/04/2025).

[33] J. N. Newman. *Marine Hydrodynamics*. en. The MIT Press, Aug. 1977. ISBN: 978-0-262-28061-7. DOI: 10.7551/mitpress/4443.001.0001. URL: https://direct.mit.edu/books/book/2693/Marine-Hydrodynamics (visited on 20/05/2025).

[34] Tor Anders Nygaard et al. 'Development, Verification and Validation of 3DFloat; Aero-servo-hydro-elastic Computations of Offshore Structures'. en. In: *Energy Procedia* 94 (Sept. 2016), pp. 425–433. ISSN: 18766102. DOI: 10.1016/j.egypro.2016.09.210. URL: https://linkinghub.elsevier.com/retrieve/pii/S1876610216308797 (visited on 03/02/2025).

[35] Vilde Stueland Nysted et al. ‘Modelling wave-induced losses for floating photovoltaics: Impact of design parameters and environmental conditions’. In: *Solar Energy* 293 (June 2025), p. 113439. ISSN: 0038-092X. DOI: 10.1016/j.solener.2025.113439. URL: https://www.sciencedirect.com/science/article/pii/S0038092X25002026 (visited on 16/05/2025).

[36] Richard Perez et al. ‘Modeling daylight availability and irradiance components from direct and global irradiance’. In: *Solar Energy* 44.5 (1990), pp. 271–289. ISSN: 0038-092X. DOI: https://doi.org/10.1016/0038-092X(90)90055-H. URL: https://www.sciencedirect.com/science/article/pii/0038092X9090055H.

[37] Jean-François Piollé, Guillaume Dodet and Yves Quilfen. *ESA Sea State Climate Change Initiative (Sea_State_cci) : Global remote sensing merged multi-mission monthly gridded significant wave height from altimetry, L4 product, version 3*. en. 2022. DOI: 10.5285/9C350D4FF7EE438F9F1FC7252CBB2282. URL: https://catalogue.ceda.ac.uk/uuid/9c350d4ff7ee438f9f1fc7252cbb2282 (visited on 19/02/2025).

[38] Zhipeng Qu et al. ‘Fast radiative transfer parameterisation for assessing the surface solar irradiance: The Heliosat-4 method’. en. In: *Meteorologische Zeitschrift* 26.1 (Feb. 2017), pp. 33–57. ISSN: 0941-2948. DOI: 10.1127/metz/2016/0781. URL: http://www.schweizerbart.de/papers/metz/detail/26/87036/Fast_radiative_transfer_parameterisation_for_asses?af=crossref (visited on 04/02/2025).

[39] D. T. Reindl, W. A. Beckman and J. A. Duffie. ‘Evaluation of hourly tilted surface radiation models’. In: *Solar Energy* 45.1 (1990), pp. 9–17. ISSN: 0038-092X. DOI: https://doi.org/10.1016/0038-092X(90)90061-G. URL: https://www.sciencedirect.com/science/article/pii/0038092X9090061G.

[40] *SARAL / AltiKa | CNES*. en. URL: https://cnes.fr/en/projects/saral (visited on 15/03/2025).

[41] M. Schroedter-Homscheidt et al. ‘Surface solar irradiation retrieval from MSG/SEVIRI based on APOLLO Next Generation and HELIOSAT-4 methods’. en. In: *Meteorologische Zeitschrift* 31.6 (Dec. 2022), pp. 455–476. ISSN: 0941-2948. DOI: 10.1127/metz/2022/1132. URL: http://www.schweizerbart.de/papers/metz/detail/31/101866/Surface_solar_irradiation_retrieval_from_MSG_SEVIR?af=crossref (visited on 04/02/2025).

[42] Josefine Selj, Stefan Wieland and Ioannis Tsanakas. ‘Floating Photovoltaic Power Plants: A Review of Energy Yield, Reliability, and Maintenance’. en-US. In: (Apr. 2025). URL: https://iea-pvps.org/key-topics/t13-floating-pv-plants-review-2025/ (visited on 02/05/2025).

[43] *Summary | Jason-1*. en. URL: https://sealevel.jpl.nasa.gov/missions/jason-1/summary (visited on 15/03/2025).

[44] Hendrik Tolman et al. *User manual and system documentation of WAVEWATCH III (R) version 6.07*. Mar. 2019.

[45] *TOPEX-POSEIDON | PO.DAAC / JPL / NASA*. en. Mar. 2020. URL: https://podaac.jpl.nasa.gov/TOPEX-POSEIDON (visited on 15/03/2025).

[46] Gerald B. Whitham. *Linear and nonlinear waves*. en. Nachdr. Pure and applied mathematics. New York: Wiley, 1976. ISBN: 978-0-471-94090-6.

[47] Jürgen Willebrand. ‘Energy transport in a nonlinear and inhomogeneous random gravity wave field’. en. In: *Journal of Fluid Mechanics* 70.1 (July 1975), pp. 113–126. ISSN: 1469-7645, 0022-1120. DOI: 10.1017/S0022112075001929. URL: https://www.cambridge.org/core/journals/journal-of-fluid-mechanics/article/energy-transport-in-a-nonlinear-and-inhomogeneous-random-gravity-wave-field/D206750AAFC1458B0DF1494F848AB693 (visited on 24/01/2025).

[48] Hye-Jin Woo and Kyung-Ae Park. ‘Long-term trend of satellite-observed significant wave height and impact on ecosystem in the East/Japan Sea’. In: *Deep Sea Research Part II: Topical Studies in Oceanography*. Current Status of the East/Japan Sea Ecosystem in a changing world 143 (Sept. 2017), pp. 1–14. ISSN: 0967-0645. DOI: 10.1016/j.dsr2.2016.09.003. URL: https://www.sciencedirect.com/science/article/pii/S0967064516302818 (visited on 14/01/2025).

[49] *World’s first offshore solar farm*. en-US. URL: https://oceansofenergy.blue/a-worlds-first-offshore-floating-solar-farm-installed-at-the-dutch-north-sea/ (visited on 29/04/2025).

Appendix A

Code

A.1 Dnora example

We note that this code example is performed wth `dnora v2`. The version is found on the branch ‘v2’ on the github repository of the `dnora` package (https://github.com/MET-OM/dnora).

```python
# ==============================
# IMPORT dnora
# ==============================
import dnora as dn
# ==============================
# DEFINE GRID OBJECT
# ==============================
# Set grid definitions
area = dn.grid.GEBCO(lon=(9.1, 9.4), lat=(58.6, 58.9), name='ExampleName')
area.import_topo()
# area.set_spacing()
area.mesh_grid()
area.set_boundary_points(dn.grid.mask.Edges())
area.set_output_points(dn.grid.mask.LonLat(lon=[9.28], lat=[58.725]))
# ==============================
# DEFINE MODEL OBJECT (mdl.)
# ==============================
model = dn.modelrun.ModelRun(area, start_time='2023-05-31T00:00',end_time='2023-05-31T03:00')
# ==============================
# IMPORT BOUNDARIES AND FORCING
# ==============================
# Boundary Spectra
model.import_spectra(dn.read.spectra.ec.ERA5(), dn.pick.NearestGridPoint())
# Wind Forcing
model.import_wind(dn.read.wind.ec.ERA5())
# ==============================
# EXPORT BOUNDARIES AND FORCING
# ==============================
exporter = dn.export.SWAN(model)
exporter.export_grid()
exporter.export_wind()
exporter.export_spectra()
# ==============================
# EXPORT NML files
# ==============================
```

```python
exe = dn.executer.SWAN(model)
exe.write_input_file()
exe.run_model(model_folder='PATH/TO/SWANFOLDER')
# ============================
#EOF
```

A.2 Acquire NORA3 subset wind data

```python
import netCDF4 as nc
import numpy as np
import subprocess

def get_indices_from_lat_lon(url, lat_range, lon_range):
    with nc.Dataset(url) as ds:
        # Lat and lon from the full dataset
        lats = ds.variables['latitude'][:, :]
        lons = ds.variables['longitude'][:, :]

        # Create a mask for the desired latitude and longitude range
        lat_mask = (lats >= lat_range[0]) & (lats <= lat_range[1])
        lon_mask = (lons >= lon_range[0]) & (lons <= lon_range[1])
        combined_mask = lat_mask & lon_mask

        # find the x and y dimension limits to download the correct area
        indices = np.where(combined_mask)
        x_min, x_max = np.min(indices[1]), np.max(indices[1])
        y_min, y_max = np.min(indices[0]), np.max(indices[0])

        return (x_min, x_max), (y_min, y_max)


def download_nc_subset(x_range, y_range, year_month, destination):
    """
    Download a subset of NORA3 wind data using ncks from a MET's THREDDS server.

    Parameters:
    - x_range: tuple of (x_min, x_max) specifying the range for the x dimension.
    - y_range: tuple of (y_min, y_max) specifying the range for the y dimension.
    - year_month: string in the format "%Y%m" representing the year and month for the filename.
    """
    input_url = f"https://thredds.met.no/thredds/dodsC/nora3_subset_atmos/atm_hourly/arome3km_1hr_{year_month}.nc"
    output_filename = f"{destination}/arome3km_1hr_{year_month}.nc"

    # command to fetch the data
    # -v are variables and -d are dimensions
    # we can not download by variable as that would download the entire file, we must limit to the corresponding x and y coordinates
    command = [
        'ncks',
        '-v', 'longitude,latitude,wind_speed,wind_direction',
        '-d', f'x,{x_range[0]},{x_range[1]}',
        '-d', f'y,{y_range[0]},{y_range[1]}',
        input_url,
        '-o', output_filename
```

```python
    ]

    print('Running command:', ' '.join(command))
    try:
        # Run the command
        result = subprocess.run(command, check=True, capture_output=True, text=True)
        print(result.stdout)
    except subprocess.CalledProcessError as e:
        print("An error occurred while running ncks:")
        print(e.stderr)


# latitude and longitude range of interest
lat_range = (50.0, 60.0)
lon_range = (5.0, 15.0)

for year_month in ['202301', '202302', '202303', '202304', '202305', '202306',
                   '202307', '202308', '202309', '202310', '202311', '202312']:

    # URL of the OPeNDAP file
    url = f"https://thredds.met.no/thredds/dodsC/nora3_subset_atmos/atm_hourly/arome3km_1hr_{year_month}.nc"

    # Get the x and y indices from the specified latitude and longitude range
    x_range, y_range = get_indices_from_lat_lon(url, lat_range, lon_range)

    print(f"x_range: {x_range}, y_range: {y_range}")

    destination = '/Users/nilsenriccanuttaugbol/NORA3/atm_hourly/'

    # Download the subset using the obtained x and y indices
    download_nc_subset(x_range, y_range, year_month, destination)

    with nc.Dataset(f'/Users/nilsenriccanuttaugbol/NORA3/atm_hourly/arome3km_1hr_{year_month}.nc') as ds:
        # Extract latitude and longitude variables
        lats = ds.variables['latitude'][:]
        lons = ds.variables['longitude'][:]

        print(np.max(lats), np.min(lats), np.max(lons), np.min(lons))
```

Appendix B

Energy yield

B.1 February at BAR, RIS, and HAV

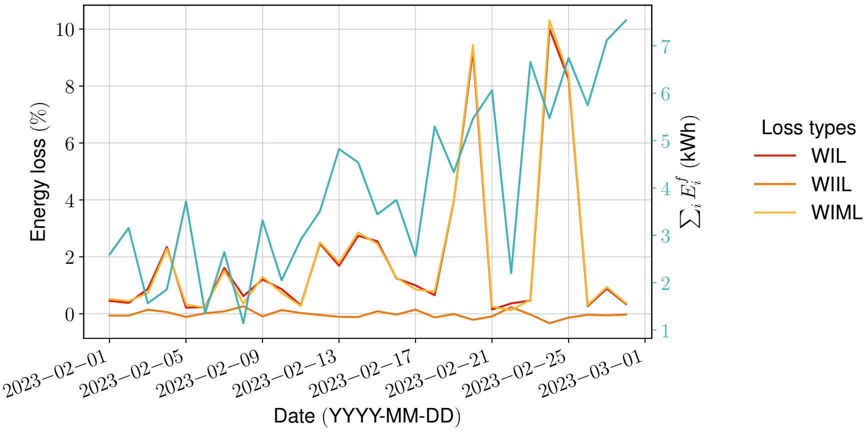

(a) Energy generation and wave-induced losses at the BAR location, February 2023.

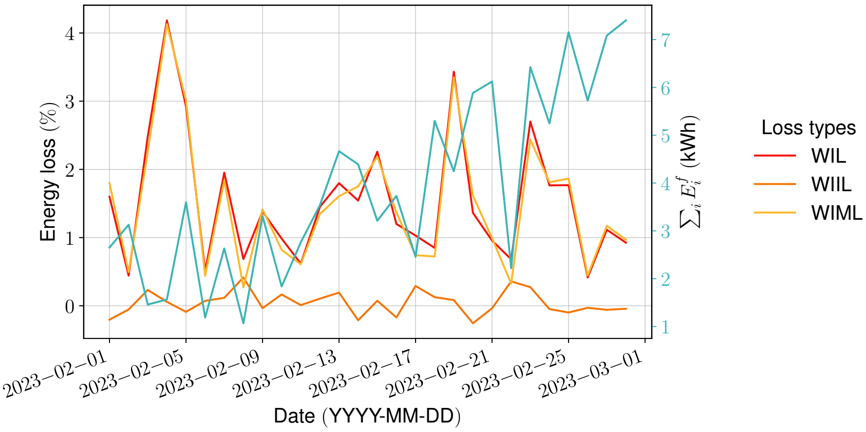

(b) Energy generation and wave-induced losses at the RIS location, February 2023.

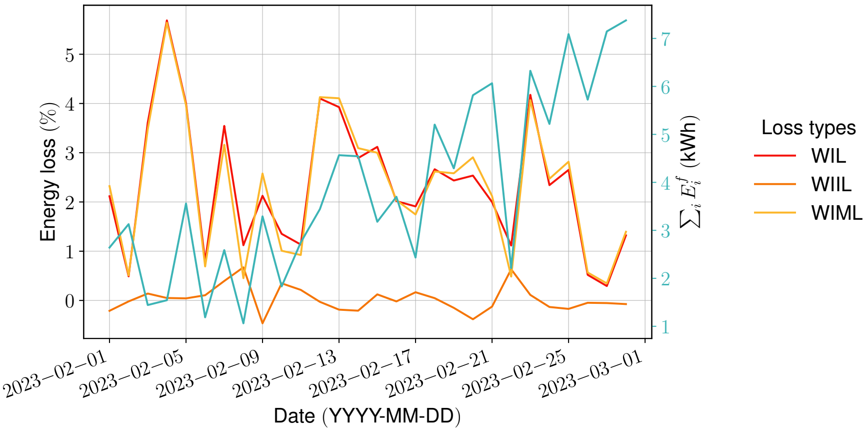

(c) Energy generation and wave-induced losses at the HAV location, February 2023.

Figure B.1: WIL, WIIL, and WIML for February 2023 at the BAR (B.1a), RIS (B.1b), and HAV (B.1c) locations. The cyan line corresponds to the right vertical axis and shows the sum of the energy produced by each individual module in the FPV system.

B.2 October 4^{th}

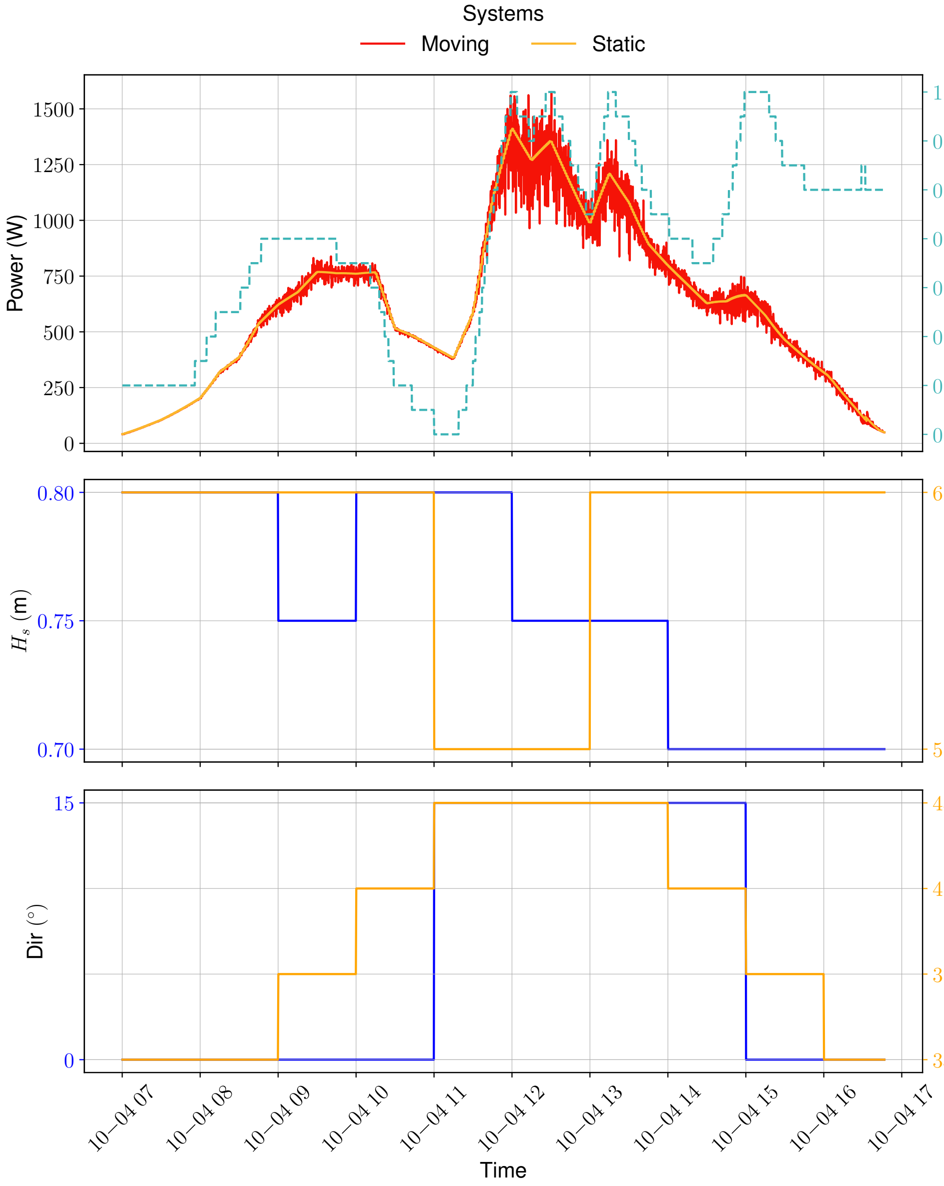

Figure B.2: Power generation of the moving and static systems at the HAV location for October 4^{th} 2023 along with the variations in sea-state variables. In the uppermost panel, the stippled cyan line represents the clearsky index, a measure of how sunny it is compared to the clearsky conditions. In the lower two panels, the blue lines correspond to the respective left vertical axis while the orange line corresponds to the respective right vertical axis.

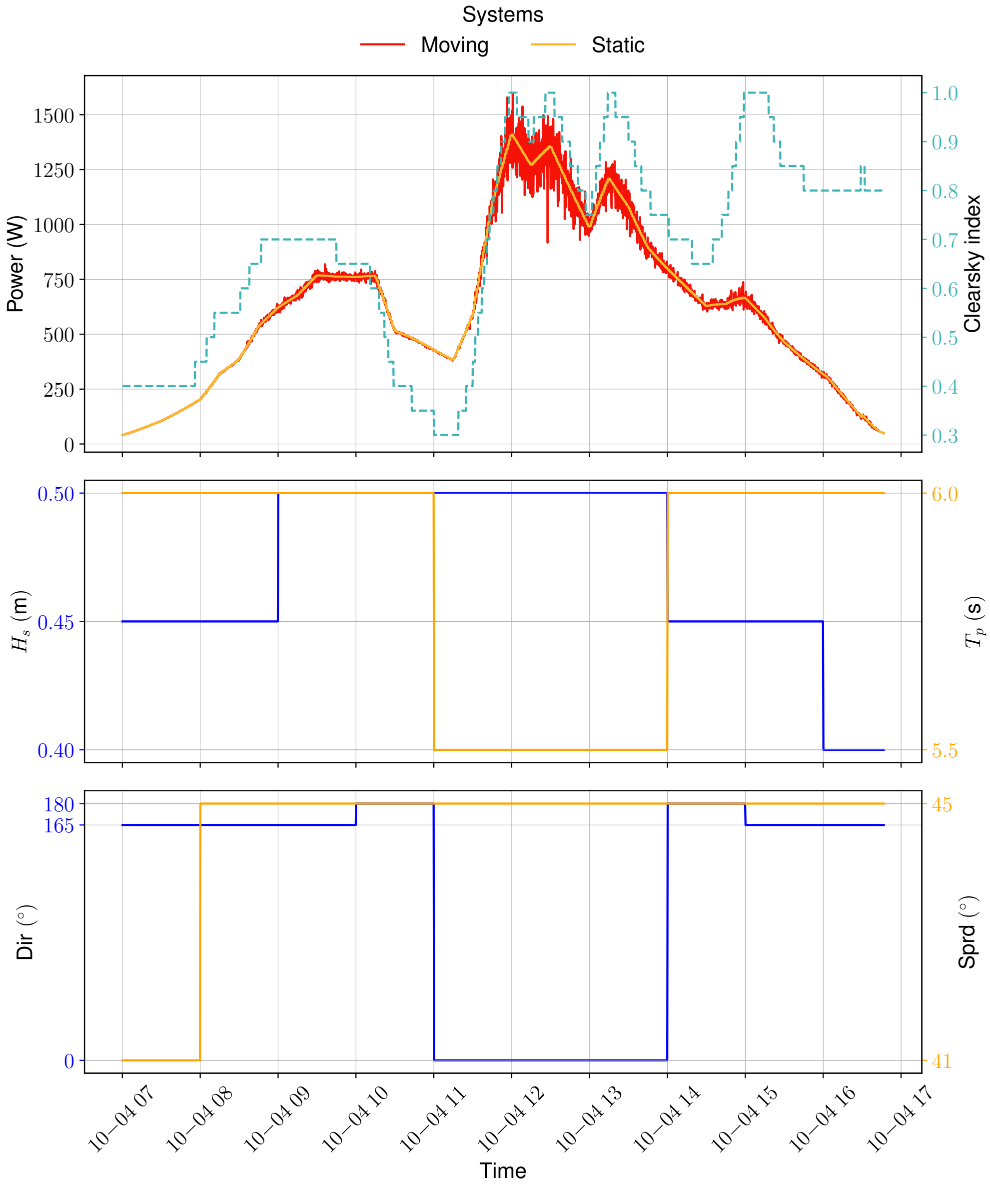

Figure B.3: Power generation of the moving and static systems at the RIS location for October 4th 2023 along with the variations in sea-state variables. In the uppermost panel, the stippled cyan line represents the clearsky index, a measure of how sunny it is compared to the clearsky conditions. In the lower two panels, the blue lines correspond to the respective left vertical axis while the orange line corresponds to the respective right vertical axis.

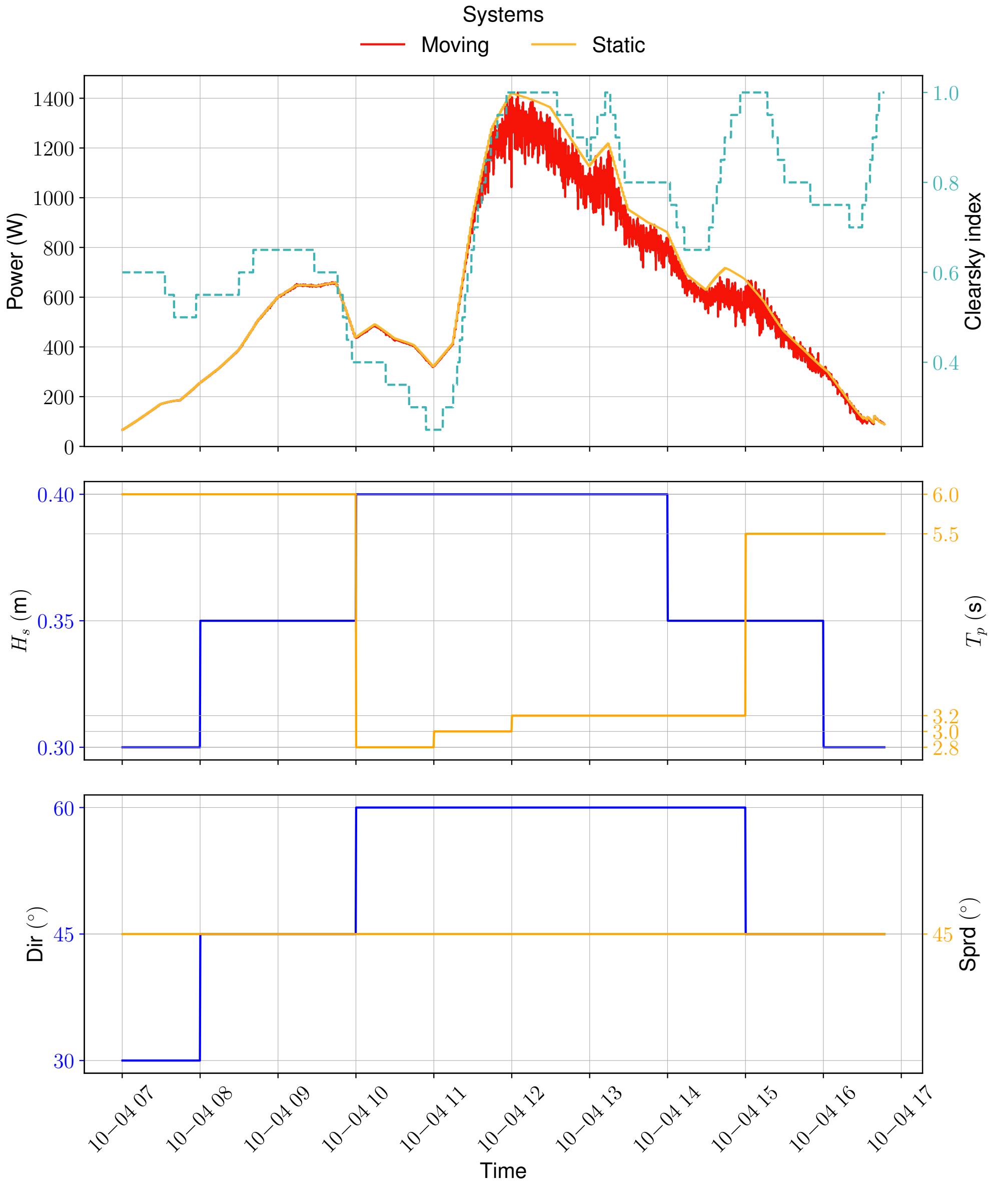

Figure B.4: Power generation of the moving and static systems at the BAR location for October 4th 2023 along with the variations in sea-state variables. In the uppermost panel, the stippled cyan line represents the clearsky index, a measure of how sunny it is compared to the clearsky conditions. In the lower two panels, the blue lines correspond to the respective left vertical axis while the orange line corresponds to the respective right vertical axis.